










Cite this: *J. Anal. At. Spectrom.*, 2026, **41**, 16

Received 10th November 2025

DOI: 10.1039/d5ja90058a

rsc.li/jaas

Atomic spectrometry update: review of advances in environmental analysis

Warren R. L. Cairns, ^{a*} Emma C. Braysher, ^b Owen T. Butler, ^c
Olga Cavoura, ^d Christine M. Davidson, ^e Jose Luis Todoli Torro ^f
and Marcus von der Au ^g

- | | |
|--|---|
| <ol style="list-style-type: none"> 1. Introduction 2. Air analysis <ol style="list-style-type: none"> 2.1. Review papers 2.2. Sampling techniques 2.3. Calibrants, reference materials and standardisation 2.4. Sample preparation 2.5. Instrumental analysis <ol style="list-style-type: none"> 2.5.1. Atomic absorption, emission and fluorescence spectrometries 2.5.2. Mass spectrometry <ol style="list-style-type: none"> 2.5.2.1. Inductively coupled plasma mass spectrometry 2.5.2.2. Mass spectrometry techniques other than inductively coupled plasma mass spectrometry 2.5.3. X-ray spectrometry 2.5.4. Carbonaceous particle measurements 3. Water analysis <ol style="list-style-type: none"> 3.1. Reviews 3.2. Reference materials 3.3. Sample preconcentration and matrix removal 3.4. Speciation 3.5. Nano- and micromaterials 3.6. Instrumental analysis <ol style="list-style-type: none"> 3.6.1. Atomic absorption spectrometry and atomic emission spectrometry 3.6.2. Vapour generation 3.6.3. Inductively coupled plasma mass spectrometry 3.6.4. X-ray fluorescence spectrometry 3.6.5. Laser-induced breakdown-spectroscopy 4. Analysis of soils, plants and related materials <ol style="list-style-type: none"> 4.1. Review papers 4.2. Reference materials 4.3. Sample preparation | <ol style="list-style-type: none"> 4.3.1. Sample dissolution and extraction 4.3.2. Analyte separation and preconcentration 4.4. Instrumental analysis <ol style="list-style-type: none"> 4.4.1. Atomic absorption spectrometry 4.4.2. Atomic fluorescence spectrometry 4.4.3. Inductively coupled plasma mass spectrometry 4.4.4. Laser-induced breakdown spectroscopy 4.4.5. X-ray fluorescence spectrometry 5. Analysis of geological materials <ol style="list-style-type: none"> 5.1. Review papers 5.2. Reference materials and data quality 5.3. Sample preparation, dissolution and chemical separation 5.4. Instrumental analysis <ol style="list-style-type: none"> 5.4.1. Laser-induced breakdown spectroscopy 5.4.2. Dating techniques 5.4.3. Inductively coupled plasma mass spectrometry 5.4.4. Secondary ion mass spectrometry 5.4.5. X-ray fluorescence spectrometry and related techniques 5.4.6. Other techniques 5.5. Software and databases 6. Glossary of abbreviations |
|--|---|

Highlights in the field of air analysis included: development of laboratory-based particle emission simulators to emulate real-world processes such as tyre-wear abrasion; ongoing performance verification of Hg calibrators; progress in laser and spark emission spectroscopic techniques for *in situ* aerosol measurements, advances in data processing software tools in supporting sp-ICP-

^aCNR-ISP and Università Ca' Foscari, Via Torino 155, 30123 Venezia, Italy. E-mail: warrenraymondlee.cairns@cnr.it

^bNational Physical Laboratory, Hampton Road, Teddington, Middlesex, TW11 0LW, UK

^cHealth and Safety Executive, Harpur Hill, Buxton, SK17 9JN, UK

^dSchool of Public Health, University of West Attica, Leof Alexandras 196, 115 21 Athens, Greece

^eDepartment of Pure and Applied Chemistry, University of Strathclyde, 295 Cathedral Street, Glasgow, G1 1XL, UK

^fDepartment of Analytical Chemistry, Nutrition and Food Sciences University of Alicante, 03690 San Vicente del Raspeig, Alicante, Spain

^gFederal Institute for Materials Research and Testing, Richard-Willstätter-Straße 11, 12489 Berlin, Germany



MS measurements, feasibility of using aerosol mass spectrometers for measuring nanoplastics in air, and a comprehensive review of brown carbon aerosols, its sources, optical properties and measurement approaches used. While recent developments in water analysis include significant progress in sp-ICP-MS, including the introduction of new measurement protocols, determination of isotope ratios, and new reference materials. The number of studies employing LIBS for assessing metal burdens in water has also grown notably, particularly with respect to innovations in sample preparation. Advances were further reported in the development of portable analytical devices and systems for continuous environmental water monitoring. In addition, several comprehensive reviews were published, providing guidance for researchers on establishing robust measurement workflows, including split-stream and sp-ICP-MS methodologies. In the analysis of plants and soils, there has been increased interest in deep eutectic solvents as milder and greener alternatives to traditional extractants. Microwave plasma torch mass spectrometry methods have been developed that allowed concurrent measurement of trace elements and organic pollutants in liquid samples. Promising steps have also been taken towards application of techniques for direct analysis of solids. Advances in LIBS have largely focussed on data processing and modelling whilst in XRF, the influence of soil matrix composition on measurement accuracy was highlighted. Quantitative geochemical analysis faces continuous challenges, making the development of new RMs a persistent priority, especially for localized microanalysis. Application of LIBS is gaining increasing interest because of its portability and the use of machine learning tools to improve the quality of the obtained data. Interest is also increasing in the analysis of extraterrestrial samples. Novel ICP-MS instrumentation has offered highly precise isotopic analysis and spectral interference removal. Other important techniques in this review period have been nanoSIMS, NAA, and MS variants because they may provide new and enhanced chemical information. The fusion of data and the significantly increasing application of AI for rapid mineral identification and data integration marks a key trend that is expected to grow exponentially.

1. Introduction

This is the 41st annual review of the application of atomic spectrometry to the chemical analysis of environmental samples. This update refers to papers published approximately between July 2024 and June 2025 and continues the series of Atomic Spectrometry Updates (ASUs) in Environmental Analysis¹ that should be read in conjunction with other related ASUs in the series, namely: clinical and biological materials, foods and beverages;² advances in atomic spectrometry and related techniques;³ elemental speciation;⁴ X-ray spectrometry;⁵ and metals, chemicals and functional materials.⁶ This review is not intended to be a comprehensive overview but selective with the aim of providing a critical insight into developments in instrumentation, methodologies and data handling that

represent significant advances in the use of atomic spectrometry in the environmental sciences.

All the ASU reviews adhere to a number of conventions. An italicised word or phrase close to the beginning of each paragraph highlights the subject area of that individual paragraph. A list of abbreviations used in this review appears at the end. It is a convention of ASUs that information given in the paper being reported on is presented in the past tense whereas the views of the ASU reviewers are presented in the present tense.

2. Air analysis

2.1. Review papers

Following a review⁷ (74 references) of sampling and analytical methods for the determination of *microplastics* in urban ambient air, it was concluded that techniques such as μ -Raman and Py-GC used in combination were required to establish dose-response relationships for health exposure studies. In a complementary review⁸ (145 references), challenges in sampling, pretreatment and analytical steps were articulated and future requirements, such as method standardisation and QA/QC requirements, discussed.

Progress in determining the composition and morphology of atmospheric particulates was the focus of three reviews. In the first review⁹ (115 references), the principles, advantages and limitations of analytical techniques for determining the physiochemical properties of ultrafine particles of <100 nm were summarised. Such techniques were broadly grouped into the following categories: electron and X-ray microscopy, optical spectroscopy and microscopy, electrical mobility and mass spectrometry. In the second review¹⁰ (302 references), while it was noted that the development of analysis methodologies has helped shape our understanding of new particle formation from gaseous precursor species, further improvements were outlined. These included the development of cheaper, more robust and easier to use particle sizing instrumentation, better measurement methods to detect and quantify low concentrations of precursor vapours and improved analytical tools for determining the composition of the resultant particles formed in the 2–20 nm size range. The reviewers concluded that there is a need for better measurement harmonisation and suggested that standard operation procedures be published and common calibration and intercomparison practices be adopted. In the third paper, various instrumental approaches for determining the RCS content in APM, spanning IR and XRD techniques that are currently used to emerging QCL-IR and Raman-based techniques, were reviewed¹¹ (160 references).

2.2. Sampling techniques

Replicating real-world particle emission processes *via* use of laboratory-based simulators as a precursor to better understanding their environmental and health impacts is an expanding but nevertheless challenging endeavour. One current interest is the need to better understand the impact of particle emissions from tyre wear. Development¹² of a novel tyre wear



Table 1 Developments in air sampling instrumentation

| Analyte | Sample matrix | Study rationale | Findings | References |
|---------------------|---------------|--|---|------------|
| APM | Air | Development of an new automated air sampler device for collection of samples at high time resolution | Compact and transportable STRAS (size and time resolved aerosol sampler) sampler for the collection of $PM_{1.0}$, $PM_{2.5}$ or PM_1 for subsequent analysis by PIXE. Ability to sequentially collect up to 168 hourly samples (1 week). Use of commercially available size-selective sampler inlets possible because system operates at a nominal flow rate of 16.7 L min^{-1} | 253 |
| APM | Air | Performance evaluation of respirable parallel particle impactor (PPI) samplers | PPI samplers challenged with polydisperse NaCl particles and select sizes of PSL particles with MMAD of $1\text{--}25 \text{ }\mu\text{m}$ in laboratory chamber studies. D_{50} values of $\sim 4 \text{ }\mu\text{m}$ determined for the single-use 2, 4 and 8 L min^{-1} flow rate PPI variants. D_{50} values of $4.07 \text{ }\mu\text{m}$ determined for the reusable 2 L min^{-1} model but a value of $4.27 \text{ }\mu\text{m}$ noted for the 4 and 8 L min^{-1} reusable variants | 254 |
| APM/asbestos fibres | Air | Development of a new portable water-based condensation aerosol concentrator | A turbulent-mixing condensation aerosol concentrator (TCAC) to efficiently collect aerosol/fibre samples by impaction onto a collection substrate as a small dried spot suitable for analysis. Demonstrated that for asbestos fibre counting applications using PCM, the TCAC could significantly reduce sample collection time (hence counting uncertainty) compared with conventional sampling onto 25-mm diameter filter collection by 2 and 3 orders of magnitude. Potential for device to be incorporated into small, handheld, portable instrument for the collection and subsequent analysis of $\text{nm }\mu\text{m}^{-1}$ -sized particles using laser spectroscopic methods, such as Raman, reflectance, absorption, fluorescence, or emission spectroscopy | 255 |
| CH_4 | Air | Development of an improved portable air sampler for radiocarbon measurements | Improved sampler over earlier iteration developed allowing effective ^{14}C measurements (MU of 0.9% for a $60 \text{ }\mu\text{g C}$ sample) to be performed following collection of a 60 L air sample. Potential for direct coupling to AMS so avoiding use of an off-line collection trap | 256 |
| PM_1 | Air | Development of improved PM_1 size-selective sampler inlets | PM_1 inlets based on the non-bouncing impactor (NBI) technique were developed that employed vacuum oil-wetted glass fibre filter (GFF) substrates, to minimise particle bounce, incorporating a daily vacuum oil injection facility. Operated at a nominal flow rate of 16.7 L min^{-1} . Modified from the existing $PM_{2.5}$ M-WINS inlet design with a cut-size (D_{50}) of $0.99 \pm 0.02 \text{ }\mu\text{m}$ determined. Can be retrofitted onto existing air sampling platforms | 257 |
| PM_1 | Air | Development of a combined inertial and pleated filter assembly for size-selective aerosol sampling | A filter-based $PM_{1.0}$ sampling system, referred to as the inertial filter/pleated filter sampler (I/P sampler), developed to separate particles $>1.0 \text{ }\mu\text{m}$ from those of $<1.0 \text{ }\mu\text{m}$ but collect both size fractions. In field trials, good correlations were achieved between this I/P sampler and conventional $PM_{1.0}$ air sampling devices (namely a cyclone sampler, a cascade impactor, a beta attenuation monitor and an EPA-approved federal reference method sampler) with r ranging from 0.90 to 1.07 (in summer time trials) and between 1.10 to 1.37 (in winter time trials) | 258 |
| $PM_{1/2.5}$ | Air | Development of 3D printed micro-cyclonic samplers for low cost aerosol sampling applications | One-piece low-cost 3D-printed micro-cyclones ($PM_{2.5}$ and PM_1) fabricated for potential use in a range of aerosol applications. The collection efficiencies and 50% cutoff diameters (d_{50}) of multiple cyclones evaluated with both monodisperse and polydisperse challenge aerosols which ranged between 0.1 to $3 \text{ }\mu\text{m}$ in size. Altering the sampler inlet orientation relative to the micro-cyclone centreline (orthogonal, 50% offset, and fully offset) resulted in sharper cut-points being achieved | 259 |



Table 1 (Contd.)

| Analyte | Sample matrix | Study rationale | Findings | References |
|---------|---------------|--|---|------------|
| UFP | Air | Performance of four impactor devices for collecting UFP evaluated, namely an ELPI, a MOUDI, a PENS and an ultraMOUDI | Impactors designed to collect UFP evaluated in both laboratory and field trials with respect to parameters such as cutoff diameters, particle bounce, pressure drop and steepness of cutoff curve. All four designs were capable of separating and collecting UFP with a cutoff diameter of ~ 100 nm but each offers unique advantages and limitations so it was essential to match an impactor to a specific application taking into consideration factors such as chemical composition, particle morphology and physical interaction of particles with selected impactor | 260 |
| Water | Fog/cloud | Development and evaluation of a new water collector for the analysis of cloud composition | New easy to clean sampler developed that can be used off-grid on battery power with a droplet D_{50} of $12\ \mu\text{m}$ estimated <i>via</i> CFD. In 21 cloud collection trials, a water collection rate of $100 \pm 53\ \text{mL h}^{-1}$ determined with an estimated collection efficiency of $70 \pm 11\%$ | 261 |

abrasion simulator, consisting of a rotating drum that ensured tyres under test remained in contact with challenge asphalt or concrete surfaces at realistic loads and speeds, enabled particles to be generated that were very similar in shape to those generated on real-world roads. It was subsequently determined that abrasion rate over concrete was *ca.* 3-fold higher than that over asphalt surfaces. In a similar experimental setup elsewhere, additional refinements were added¹³ namely: an enclosed experimental rig to improve thermal stability and minimise background fluctuations in particle numbers, use of a catalytic stripper to ensure that only those non-volatile particle emissions were measured, and addition of sand particles to the testing protocol to mimic other particles typically present on roads. To simulate¹⁴ a dusty indoor air environment, a vortex generator to resuspend collected house dusts and a cyclone to then collect a requisite PM_{10} size fraction on PTFE filters for subsequent analysis. This simulation was undertaken because indoor air sampling to collect sufficient sample mass for chemical testing remains logistically challenging but is less so for settled dusts.

Applications and developments in air sampling instrumentation are summarised in Table 1.

2.3. Calibrants, reference materials and standardisation

In a comprehensive *review paper*¹⁵ (282 references), published measurement standards that underpin the metrology of particle mass, number concentration and size determinations were summarised. Whilst such knowledge may be familiar to many metrologists and regulators, a key aim was dissemination aimed at research students and air monitoring practitioners wishing to improve the quality of their measurements. Future monitoring needs were summarised including a requirement to perform better measurements of nm-sized particles at high airborne concentrations, and μm -sized bioaerosols at low concentrations. There was a recommendation that both

operating and associated quality assurance procedures should be tabulated from the outset either when new instrumentation is developed or when new air monitoring networks are implemented. In another comprehensive review paper¹⁶ (109 references), the status of nanoscale RMs used in supporting measurements of engineered nanomaterials was summarised by tabulation of certification and ILC exercises undertaken to characterise materials developed to date. A useful synopsis of the underpinning standardisation activities and regulatory requirements was also presented. To conclude, future RM needs were summarised including, for example, the need for poly-disperse nanomaterials that are more representative of real-world matrices.

Calibration of Hg analysers remains topical. The saturated mass concentration of Hg in air above a liquid pool can be calculated using the Dumarey equation and is used for calibrating gas analysers, but recent studies have questioned its accuracy. In a new study,¹⁷ the concentrations of Hg^0 gas standards, generated either by cold vapour reduction of defined volumes and concentrations of NIST SRM 3133 (mercury standard solution) or prepared from a saturated headspace, were compared and differences of $<4\%$ noted. As the MUs overlapped, the researchers concluded that such small discrepancies were attributable to random measurement effects and not to any systematic bias. They also concluded that there was a need to correct Hg^0 concentration values arising from air expansion effects during sample injection of aliquots of this head-space gas as calibrants. Page *et al.* described¹⁸ for the first time a methodology based on the use of on-line ID-ICP-MS for the direct quantification of gas standards generated from Hg calibrator units. This was achieved by: mixing the outputs from these calibrators with a vapour derived from the reduction of a ^{199}Hg -enriched liquid standard, measuring the $^{202}\text{Hg}/^{199}\text{Hg}$ ratio of this blended gas and calculating the resultant calibrator output using a single ID equation adapted for gas mixtures. The efficiency of the ^{199}Hg vapour generation step was



Table 2 Air-related RM developments

| Analyte | Sample matrix | Study rationale | Findings | References |
|---------|------------------------------|---|--|------------|
| Pu/U | MP RM | Development of a combined Pu/U RM for nuclear safeguarding measurement applications | New spherical particles 1 μm in size with desired elemental and isotopic distributions synthesised and electrostatically deposited upon silicon planchets | 262 |
| Hg | Pine needles | Development of two new RM for biomonitoring of atmospheric Hg concentration | NIES RM 1001 (pine needle 1) and RM 1002 (pine needle 2) with Hg values of 5.4 ± 0.4 and $22 \pm 2 \text{ ng g}^{-1}$ ($k = 2$) determined using TD-AAS. Indicative isotopic Hg values (<i>via</i> MC-ICP-MS) and selected elemental values (<i>via</i> ICP-AES/MS) also provided | 263 |
| Ni/Mo/W | Isotopic taggants | Synthesis and characterisation of isotopically barcoded taggants for intentional nuclear forensics applications | Synthesis of taggant species of Ni, Mo and W undertaken <i>via</i> a double-spike mechanism, whereby two highly enriched isotopes of interest per elemental taggant were mixed to form an enriched "double-spike" that was subsequently isotopically diluted with bulk material having a natural isotopic composition. $^{60}\text{Ni}/^{58}\text{Ni}$, $^{100}\text{Mo}/^{98}\text{Mo}$, $^{186}\text{W}/^{183}\text{W}$ measurements undertaken <i>via</i> MC-ICP-MS at two independent laboratories | 264 |
| Various | Atmospheric fallout material | Further characterisation of a RM prepared by the National Meteorological Institute of Japan | The ^{237}Np activity concentration, $^{237}\text{Np}/^{239}\text{Pu}$ atom ratio, and $^{237}\text{Np}/^{241}\text{Am}$ activity ratio in a reference fallout material determined following separation and purification using AEC, use of ^{242}Pu as an ID tracer in subsequent assays using SF-ICP-MS | 265 |

predetermined *via* a procedure that used a ^{197}Hg radiotracer. Significant uncertainties remain in the sampling and analysis of trace GOM species in ambient air, so a review¹⁹ (47 references) of current calibration approaches and future measurement requirements is timely.

Developments in RM applicable to air measurements are summarised in Table 2.

2.4. Sample preparation

Understanding the *solubility of metal-containing APM*, key parameter in aerosol toxicity studies, is nuanced by viewing from the bulk or single particle perspective. A timely and all-encompassing review²⁰ (211 references) summarised current knowledge, described interactions between physical and chemical factors that can influence solubility, and critiqued both available on- and off-line analytical tools. Future recommendations included a need to develop new supporting measurement techniques. In two independent studies,^{21,22} the impact of different sample preparation procedures and various reagents, used to extract APM from filter samples for toxicological testing, was assessed. It was concluded that the composition of a prepared sample could indeed be different from that of the collected sample, thus placing doubt on the accuracy of subsequent testing. Standardisation of sample preparation procedures was therefore advocated to ensure comparability in future toxicological studies.

Air-related sample preparation applications are summarised in Table 3.

2.5. Instrumental analysis

2.5.1. Atomic absorption, emission and fluorescence spectrometries.

The development of a prototype *spark emission spectrometer*, the so-called TARTA (Toxic-metal Aerosol Real time Analyser) that was reviewed in an earlier ASU,²³ has now progressed²⁴ to testing in the field. This portable instrument with the ability to perform *in situ* trace metals measurements in $\text{PM}_{2.5}$ at high temporal resolution was deployed at three locations (urban roadside, urban background and rural) and tested against a co-located XRF-based analyser (Xact 625i®). A number of $\text{PM}_{2.5}$ filter samples were also collected in parallel for additional comparative testing using a laboratory-based XRF spectrometer. The average TARTA to laboratory measured ratio was 1.01 (Cu), 0.93 (Fe), 1.04 (Mg) and 1.07 (Zn) but ranged between 9 and 22 for Cr. A need here for future calibration refinements was noted. Side-by-side comparative testing against the Xact instrument was limited to only Cu, Fe and Zn because airborne concentrations of other metals were below the Xact LOD because the air sampling interval was only one hour. While it was acknowledged that r^2 values of 0.29 (Cu), 0.09 (Fe) and 0.61 (Zn) were poor, the researchers pointed out the challenges in conducting comparative instrumental side-by-side testing in the field, which included the microspatial heterogeneity of airsheds, differences in particle sampling efficiencies and variations in instrumental calibration approaches. Further instrumental refinements were described, but this system already offers a tantalising new potential for the *in situ* measurement of metals in a variety of air environments.



Table 3 Selected air-related sample preparation applications

| Analyte | Sample matrix | Study rationale | Findings | References |
|-------------------|-------------------------|---|--|------------|
| NPs | Air filter samples | Development of a standardised MAE procedure for extraction of non-labile metallic NPs prior to sp-ICP-MS analysis | Quantitative extraction of unaltered NPs <i>e.g.</i> Au/Pt NPs achieved in 6 min using a 0.1 M NaOH extractant | 266 |
| NPs | Urban dust | Methodology developed for the separation of metallic NPs from bulk dust samples and their preparation for subsequent biotoxicity testing | Isolation of NPs from dust matrix achieved using coiled tube FFF. Albumin then used as a stabilising agent, a 5 min UV treatment to sterilise samples (because extracted NP samples contained microorganisms) and a ultrafiltration step to preconcentrate samples | 267 |
| REEs | APM/cigar smoke samples | Synthesis of magnetic functional sorbents for SPE of REEs from digested samples prior to ICP-MS analysis | Sorbent demonstrated a high affinity for REEs (EF of up to 300) with good reusability (up to 45 times) and enabled MDL of 0.001–0.2 ng L ⁻¹ to be achieved | 268 |
| PM _{2.5} | Filter samples | Development of an UAE procedure for extraction of metals from PM _{2.5} samples, collected on beta attenuation filter spots, prior to ICP-MS analysis | Use of a HNO ₃ extractant enabled metals of regulatory interest such as As, Cd, Co, Cr, Cu, Ni, Pb, Sb, and V to be determined at MDL of 0.001 µg m ⁻³ (24 m ³ air volume sample). However, endogenous concentrations of elements, such as Ba, Fe and Zn present in the glass fibre filter media, compromised some measurements | 269 |

In a review²⁵ (121 references) of progress in the use of LIBS for measurements of atmospheric species, selected applications were presented as exemplars. One example was the emerging use of LAMIS for isotopic analysis exploiting both atomic and molecular spectral emission data. A second example was the analysis of indoor air pollutants when algorithms and tools such as BP-ANN, PCA and SVM were leveraged to decipher emission signals arising from complex aerosol mixes. A third example was use of LIBS in wider industrial settings, such as monitoring workers' exposure to welding fume or measuring emissions from biomass combustion, where on-line rapid measurements were advantageous for process diagnostic purposes. Future directions noted included use of ultrafast LIBS to enhance laser ablation efficiency and stability; use of LIBS-LIF to enhance measurements of organic species, and use of machine learning tools for improved data interrogation.

Air-related atomic spectrometric applications and developments are summarised in Table 4.

2.5.2. Mass spectrometry

2.5.2.1. Inductively coupled plasma mass spectrometry. In a review of developments and applications of sp-ICP-MS, for the elemental, isotopic and sizing analysis of individual NPs covering use of quadrupole, magnetic sector and TOF systems, the emergence of AI tools for interrogating large datasets was one important topic highlighted²⁶ (160 references). Similarly, progress in sp-ICP-MS studies over the past ten years was detailed²⁷ (106 references) and a projected look over the next ten years presented when it was envisaged that new single particle studies will improve our understanding of environmental processes in arenas such as biogeochemical cycling and climate change.

Handling and interrogating large datasets remains challenging, so a review of the advances here in single cell/particle-ICP-(TOF)-MS studies²⁸ (45 references) is welcomed. A new iteration of SPCal, an open-source Python-based programme initially developed to handle QMS datasets, has now been released²⁹ for sp-TOF-ICP-MS users. New tools were incorporated to facilitate the handling and manipulation of larger data at processing rates >1 and 2 gigabit min together with implementation of enhanced data analytical tools and improved statistical functionalities. Deciphering complex and overlapping particle signal events in sp-ICP-MS studies can be difficult, thus making particle-type classification studies challenging. To assist here, a multi-stage SSML model was developed³⁰ which used as a training sample, a suspension that consisted of natural biotite, ilmenite and rutile NPs alongside a man-made TiO₂ NPs (E171 grade) material. Improved classifications were thus obtained with false positive classification rates of <2% for the natural species and <5% for the anthropogenic material. It was suggested that use of this SSML model approach could be extrapolated to other particle classification studies.

Effective *sample preparation* is key to good analysis. In developing³¹ a sp-ICP-MS method for the determination of airborne metallic NPs in indoor air, use of MCE filter media for sampling was advantageous, because the particles were fully dissolved in 0.1 M NaOH by MAE. This enabled various test NPs to be quantitatively recovered from spiked test samples irrespective of composition or size. In subsequent experiments using Pt NPs, a LOD_{size} of 15 nm and a LOD_{concentration} of 120 particles L⁻¹ were established, values deemed suitable for future indoor air quality measurements. Following preliminary UAE experiments that involved leaching aliquots of ERM-CZ120



Table 4 Selected air-related atomic spectrometric applications and developments

| Analyte | Sample matrix | Study rationale | Findings | References |
|--|------------------------------|---|--|------------|
| Al, Ca, Fe, Si, Ti | Coal dust | Development of an on-line SES-based analyser for the determination of metals in coal dusts (anthracite, bituminous coals and lignite) | LOD of $<4 \text{ mg m}^{-3}$ for a sampling time of 10 min. Use of PCA possible to categorise coal samples | 270 |
| Al, Ba, Ca, Cu, K, Mg, Na | APM | Use of a commercially available PILS in conjunction with a micro discharge OES (μDOES) analyser for near real-time determination of water-soluble metals in sampled μm -sized particles | LODs of 0.01 (Al), 0.02 (Ba), 0.01 (Ca), 0.01 (Cu), 0.01 (K), 0.05 (Mg) and 0.001 (Na) $\mu\text{g m}^{-3}$ with long-term repeatability of $<5\%$ achieved. Suggested that the compact design with advantage of ease of operation and maintenance was suitable for <i>in situ</i> measurements in the field | 271 |
| Ba, Pb, Sb | GSR | Development of a protocol for the identification of GSR that used LIBS in conjunction with use of PCA and a probabilistic SVM algorithm for dimensionality reduction | Potential alternative to the more commonly used SEM-EDS method developed. Demonstrated that 100% accurate classifications were possible even in simulated samples contaminated with those elements characteristic of GSR | 272 |
| Cr ₂ O ₃ , CuO mixed with SiO ₂ , Ni ₂ O ₃ , ZrO ₂ | Simulated workplace aerosols | Development of a real-time analyser that integrated Raman and SES to characterise both the elemental and molecular composition of airborne particles present in workplace air | Nozzle impactor-based sampler developed to collect and preconcentrate aerosol samples for analysis. Instrumental LODs were 80 (Cu), 14 (Cr), 6 (Ni) 14 (Si) and 65 (Zr) $\mu\text{g m}^{-3}$ for a nominal 20 L air sample collected at 2 L min ⁻¹ for 10 min | 273 |
| Cu, Pb | Simulated aerosols | Development of a LIBS analyser for <i>in situ</i> analysis of gas-phase aerosols contaminated with metals | System consisted of a 1065 nm Nd:YAG laser, a Czerny–Turner spectrometer and a CCD camera. Simulated Cu and Pb aerosols over the range 0.26–1.29 ppmv and 0.40–1.19 ppmv generated from nebulising liquids standards that were subsequently desolvated. The instrumental LODs were 2 and 5 ppbv with LOQs of 5 and 28 ppbv | 274 |
| Hg | Flue gas | Development of an APGD-AES spectrometer, incorporating a gold amalgam system for analyte enrichment for the ultrasensitive determination of Hg | Measurements at 253.6 nm performed. The method LOD was 0.1 $\mu\text{g m}^{-3}$ for a nominal 10 L gas sample. Relative deviations from reference measurements undertaken using a Hg combustion AAS analyser were $<3\%$ | 275 |
| Hg | Air | AFS analysers require the use of inert carrier gases such as Ar or He but ongoing replenishment of bottled gas supplies was logistically challenging for analysers deployed in remoted monitoring locations so development of an analyser with reduced gas consumption undertaken | New prototype AFS analyser developed which incorporated a recirculating carrier gas system with an embedded Hg scrubber so facilitating reuse. Gas consumption was only 1 L per week, up to 99% decrease in gas consumption compared with that of existing analysers | 276 |
| K, Na, Mg | Simulant aerosols | Development of a field deployable LIBS instrument for the analysis and classification of aerosol particles at the single particle level | A size amplification aerosol charging device employed for efficient particle focusing using a linear electrodynamic quadrupole. Absolute instrumental LODs achieved on stimulants were 70 (K), 40 (Na) and 2 (Mg) ng. In testing of an outdoor aerosol sample with particles in the size range of 1–3 μm , an analysis speed of <i>ca.</i> 20 particles per min. and size LODs of 0.3–0.8 μm were achieved | 277 |



Table 4 (Contd.)

| Analyte | Sample matrix | Study rationale | Findings | References |
|----------------|---|---|--|------------|
| O ₂ | Ice core bubbles | Development of a new instrument, based on the optical-feedback cavity-enhanced absorption spectroscopy (OF-CEAS) technique for the simultaneous and continuous measurement of O ₂ concentration and $\delta^{18}\text{O}(\text{O}_2)$ in trapped gas bubbles at high-temporal-resolution to better understand past climatic conditions | The minimum Allan deviation occurred between a 10 and 20 min window, which corresponded to the optimal achievable integration time and analytical precision, —0.002% for the O ₂ concentration and 0.06‰ for $\delta^{18}\text{O}(\text{O}_2)$ —before onset of instrumental drift started to degrade measurements. Results on test gas samples were in good agreement with those obtained using dual-inlet IRMS. Measurements of $\delta^{17}\text{O}(\text{O}_2)$ values were possible but achievable precisions as yet not comparable to those obtained using IRMS | 278 |
| Rh, Pd, Pt | Spend automotive catalyst and e-waste materials | Development of a method for the determination of PGE using HR-CS-FAAS following MAE at 240 °C using aqua regia | LODs of 0.6, 0.5 and 0.4, mg kg ^{−1} achieved for Pd, Pt and Rh, respectively with a precision <7%. Results for Pd, Pt and Rh in ERM EB504 (PGE in used automobile catalyst) respectively and Pd in BAM CRM-M505a (electronic scrap) were within certified ranges | 279 |

(PM₁₀-like fine dust) in different extractants,³² 10 mM Na₄P₂O₇ solution was deemed optimal. In subsequent sp-ICP-MS analysis of extracts from PM₁₀ air filter samples collected in the vicinity of a historical mining area, it was determined that 0.3–1.7% of total Pb and 0.6–3.8% of total Zn were NPs.

Use of a novel on-line *gaseous sample introduction* system enabled metal(loid) impurities, be they gaseous or nanoparticulate, in semiconductor grade gases to be determined³³ by ICP-MS. The gas exchange device (GED) incorporated a membrane for the effective substitution of the test gas matrix with argon thus enabling the plasma to be sustained. Achievable elemental LOD were typically 5 to 50-fold lower than those obtainable using a conventional gas-into-liquid impinger sampler with ICP-MS analysis back in the laboratory. A similar GED-ICP-MS system was deployed³⁴ in the on-line determination of trace metals in PM_{1.0} where the average concentrations of metals (Ba, Cd, Co, Cr, Cu, Mn, Mo, Ni, Pb and V) were <10 ng m^{−3}. The high temporal resolution of this methodology effectively captured diurnal variations and episodic pollution events, which was not possible with traditional time-averaged filter-based methods that involved laboratory analysis. Preliminary results were reported³⁵ in a novel study suggesting that ICP-MS/MS could be used to identify organic-based volatiles. Initially, test VOCs such as benzene and toluene were introduced directly into the CRC resulting in molecular interactions induced by collision with Ar⁺ ions derived from the plasma. From examination of resultant mass spectra the reaction products observed, arising from a soft ionisation process, included molecular ions (M⁺), protonated ions ((M + H)⁺) and deprotonated ions ((M−H)⁺). A follow-up investigation of volatile dimethyl diselenide (Se₂(CH₃)₂), revealed products such as Se⁺, Se₂⁺, [SeCH₃]⁺, [Se₂CH₃]⁺, [Se₂(CH₃)₂]⁺ and SeH⁺ indicating that other processes occurred besides soft ionisation.

Other ICP-MS applications and developments for air-related measurements are summarised in Table 5.

2.5.2.2. Mass spectrometry techniques other than inductively coupled plasma mass spectrometry. Progress over the past ten years in the application of *GD-TOF-MS* for analysing solid and gaseous samples was discussed³⁶ (60 references), including measurement of inorganic compounds and VOCs in ambient air and exhaled breath. It was noted that the advent of higher resolution systems with $m/\Delta m$ of 6000 now facilitated improved elemental and molecular determinations.

The *aerosol chemical speciation monitor (ACSM)*, available either as a quadrupole or a TOF mass spectrometer, is widely used for real-time *in situ* measurements of APM, but since both possess only unit mass resolving power, ions with similar m/z , such as OH⁺ ν NH₃⁺, which are of interest to aerosol scientists, cannot be resolved. This limitation was now addressed³⁷ by the development of an improved instrument with a $m/\Delta m$ of 2000 resulting in a LOD improvement from 0.200 to 0.008 $\mu\text{g m}^{-3}$ in measuring NH₃ concentrations. Another accrued benefit was the improved mass spectral separation at m/z 30 of the CH₂O⁺ and NO⁺ species thereby facilitating an improved interrogation of particulate nitrate species derived from either inorganic or organic precursors. There is a growing concern about the potential health impact of airborne nanoplastics, so their potential measurement by on-line aerosol MS is welcomed. In a proof of concept study³⁸ that involved measuring nano-sized PET particles, it was observed that resultant mass spectra were consistent with those obtained using Py-GC-MS, a technique currently used in an off-line mode for measuring airborne nanoplastics collected on filters. This suggested that similar thermal decomposition processes and ion fragmentation mechanisms were in play. Measurements undertaken of characteristic fragmentation ions at m/z 149 and 166 enabled LODs



Table 5 Selected air-related ICP-MS developments and applications

| Analyte | Sample matrix | Sample preparation/ introduction | Technique | Rationale and findings | References |
|----------------|--|--|---------------|---|------------|
| Ag | NP test standards | Miniaturized ultrasonic nebulization | sp-ICP-MS | Development of a miniaturized ultrasonic nebulization system that achieved ~80% transport efficiency thereby enabling AgNPs of 60 nm and 100 nm to be accurately sized | 67 |
| Au | Spiked polymer thin film | LA | sp-ICP-MS | Liquid-spiked polymer thin films standards produced that enabled defined number of particles to be introduced into the plasma by selecting a particular laser ablation spot size. Accurate sizing of both single- and multi-element NPs within $\leq 2.5\%$ of the certified diameter value achieved. A LOD_{mass} for gold NP of 3×10^{-7} ng achieved, which equated to a LOD_{size} of 15.5 nm, comparable to that obtained with the more conventional liquid-suspension sample introduction approach | 280 |
| Au, Fe | NP standards | Direct particle introduction and suspension nebulisation | sp-ICP-MS | Direct surface sampling probe system developed with an extraction efficiency of 4–10% comparable to the transport efficiency (1–10%) obtained with conventional liquid-suspension sp-ICP-MS introduction. NPs and MPs ranging from 30 nm and 1 μ m accurately sized | 281 |
| Ce, Eu, Lu | Lanthanide doped test microparticles | Suspension nebulisation | sp-ICP-TOF-MS | Performance (accuracy, impact of collision gas in CCT mode, precision, signal intensity) of two commercial instruments (icpTOF 2R® and CyTOF Helios®) for the determination of $^{153}Eu/^{151}Eu$, $^{142}Ce/^{140}Ce$, and $^{176}Lu/^{175}Lu$ in lanthanide-doped MPs assessed as a prelude to future fingerprint studies for identifying sources and fate of MPs released into the environment | 61 |
| CeO | 1 μ m-sized CeO test microparticles | Suspension nebulisation | sp-MC-ICP-MS | Demonstrated that by using fast integration times, as low as 50 ms, it was possible to undertake isotope ratio measurements in microparticles that were of sufficient precision and accuracy for potential future environmental and nuclear forensic applications | 63 |
| Cr, Fe | NPs emitted from additive manufacturing 3D printing process involving use of impregnated ABS and PA filament polymers. (acrylonitrile butadiene styrene and polylactic acid) | Sonication from filters/ suspension nebulisation | sp-ICP-TOF-MS | Sampling chamber and filtration system designed to collect emitted particles from printing process. Metals such as Al, Cr, Fe, Ti, and Zr measured in emitted particles demonstrating that metal-containing aerosols were released during 3D printing | 282 |
| Cu, Fe, Ti, Zn | NPs deposited from vehicular emissions | Filtration of motorway liquid runoff and rainfall samples/ suspension nebulisation | sp-ICP-MS | Determined that average particle per L of runoff water in descending order was Ti (4.8×10^8) > Fe (1.7×10^8) > Zn (9.0×10^7) > Cu (7.8×10^7) from a heavily trafficked urban motorway ~1 00 000 vehicular movements per d. Except for Fe, runoff samples exhibited higher concentrations of Cu, Ti and Zn NPs compared with the rainfall samples collected nearby as comparators | 283 |
| Fe, Pt, Si | Iron nanotubes and platinum nanorods | Sonication/suspension nebulisation | sp-ICP-MS | Application demonstrated that it was possible to obtain accurate mass and dimensional estimations that aligned with results obtain from more conventional SEM and HR-TEM analysis | 284 |



Table 5 (Contd.)

| Analyte | Sample matrix | Sample preparation/ introduction | Technique | Rationale and findings | References |
|------------|--|---|----------------|---|------------|
| Fe, Ti, Zn | Road-dust NPs | Air dried, filtered and suspension nebulisation | sp-ICP-MS | The number concentration ranges determined, per mg of road dust, were Fe (3.8×10^6 – 8.4×10^8), Ti (2.3×10^6 – 1.4×10^8) and Zn (6.0×10^5 – 2.3×10^8). Higher number concentrations found in summer than in winter. Hotspots of Fe-containing NPs were more concentrated in industrial and traffic areas, Zn-containing NPs were mainly distributed in the central urban areas, while Ti-containing NPs were abundant in areas that received high rainfall | 285 |
| Pb | PM ₁₀ | MAD of air filter samples | ICP-MS-MS | Development of a high throughput ICP-MS/MS measurement protocol enabled Pb isotope ratio values in PM ₁₀ to be determined in the first UK nationwide survey. Values for $^{207}\text{Pb}/^{206}\text{Pb}$ ranged from 0.864 to 0.910 (average RSE of 0.68%) while $^{208}\text{Pb}/^{206}\text{Pb}$ values ranged from 2.08 to 2.187 (average RSE of 0.84%). The calibration method developed used NIST SRM 981 (common Pb isotopic standard) and was sufficiently precise to distinguish variations in isotope ratios between sampling locations and types of samples | 286 |
| Ru | Ru-containing test particles collected on aerosol deposition samplers | Particles subsampled from deposition sampler collection plates onto GSR tabs prior to LA raster analysis | LA- ICP-TOF-MS | Automated, high-throughput analysis of particles presented on GSR tabs undertaken. Confirmatory analysis undertaken using SEM-APA on same tab samples demonstrated that LA-ICP-TOF-MS approach was 100% successful in detecting sampled particles | 287 |

of 0.4 and 0.1 $\mu\text{g m}^{-3}$ to be achieved. The expansion of air monitoring research networks in different global locations has resulted in the deployment of an increased number of ACSMs, so a better understanding of instrument-to-instrument variability was critical if regional data sets were to be compared. In one recent intercomparison, the comparative testing of six Q-ACSM instruments was undertaken³⁹ both in laboratory and field settings. In the former exercise, instruments were challenged with inorganic NH_4NO_3 and NH_4SO_4 particles and various organic species such as levoglucosan, which is used as an atmospheric chemical tracer for biomass burning. In the latter field exercise, variabilities in measured atmospheric concentrations of species such as Cl^- , NH_4^+ and SO_4^{2-} were assessed. Findings from this exercise provided valuable insights into the respective calibration and operational procedures used and enabled new relative ionisation efficiency data to be tabulated.

2.5.3. X-ray spectrometry. By employing Rietveld refinement within a XRD procedure, quantification⁴⁰ of heavily-laden RCS air filter samples was improved because processing overlapping reflections present in complex mineralogical samples was possible. A performance evaluation of the Horiba PX-375®

continuous XRF particulate monitor for the online determination of elements present in PM₁₀ was reported.⁴¹ Following instrumental calibration with filters available from the University of California at Davies, it was demonstrated that a LOD (3 s) of $<3 \text{ ng m}^{-3}$ was achievable for key elements such as Cu, Ni, Pb and Zn in APM following sampling at hourly intervals and resulted in a MU ($k = 2$) of between 5 and 25% for those determinants present in air $>20 \text{ ng m}^{-3}$.

2.5.4. Carbonaceous particle measurements. Photometers such as the widely used aethalometer provide continuous measurements of *black carbon* in air. Following a review⁴² (89 references) of published monitoring studies, mass absorption cross-section values of 10.1 ± 3.7 and $3.4 \pm 5.7 \text{ m}^2 \text{ g}^{-1}$ for urban and rural airsheds were tabulated that can be used to calculate an equivalent black carbon mass concentration (eBC). Carbonaceous APM can also be determined using an alternative elemental carbon (EC) measurand and here average eBC:EC mass ratios of 0.81 and 1.17 for freshly emitted and aged carbonaceous particles were also tabulated.

Brown carbon is that fraction of organic aerosols that can adsorb light in the short-visible and UV spectral ranges. One key emission source can be wildfires which now occur at an



increased frequency due to climate change. The publication of an extensive review paper⁴³ (124 references) is therefore timely wherein emission sources, optical properties and measurement approaches were discussed. A key future requirement noted was the need to identify suitable chromophores that can be used as specific markers of brown carbon aerosols prior to the development of develop standardised optically-based measurement methods.

Elemental carbon (EC) is determined *via* combustion analysis of APM collected on air filter samples using thermal optical analysers (TOA) working to operationally-defined protocols. Subtle alterations in protocols employed in laboratories can result in variations in reported EC values and here use of ILCs were valuable in gaining a better insight into such differences. In one reported single study,⁴⁴ an expanded ($k = 2$) MU of 17% was calculated for determinations of EC collected on filters from the exhaust of a helicopter engine by five participating laboratories operating identical analysers and protocols. Here test samples were prepared by passing emissions initially through a catalytic stripper to remove volatiles and collecting a PM₁ fraction on filters for comparative testing. It was noted that while this MU value was largely dominated by the between-laboratory variance which likely represents the optimal achievable method performance because identical instruments working to the same protocol were used. In a second study⁴⁵ that involved laboratories participating in an ongoing PT programme for the analysis of diesel fume collected on filter samples, a median between laboratory reproducibility of 23% and 19% was calculated for those cohorts that operated the widely-used EN 16909 and NIOSH 5040 protocols, respectively. Furthermore, the correlation coefficient between EC_{NIOSH 5040} data and EC_{EN16909} data was 0.86, which agreed well with those of previously published relationships.

3. Water analysis

3.1. Reviews

Seawater remains one of the most challenging matrices in water research, since in most cases analyte preconcentration and matrix separation are necessary. Thus, to enable routine seawater analysis, sample preparation and the commercial availability of suitable resins is crucial. Haryanto *et al.*⁴⁶ presented a comprehensive overview (178 references) of current strategies for the preparation of seawater and pore water samples, with a particular focus on commercially available resins for REE and trace metal preconcentration. The extent to which researchers had used different types of resins, calibration strategies and manifold setups (both pressurized and non-pressurized) was illustrated graphically as pie charts, and a list of analyses conducted over the past 20 years was compiled.

The *environmental burden of nano- and microplastics* has become a growing concern in recent years, leading to a significant increase in research interest and scientific publications in this field. Three comprehensive reviews provided an oversight of current developments. Fernandes *et al.*⁴⁷ (154 references) focused on the characterization of microplastic in aquatic environments. Moteallemini *et al.*⁴⁸ (233 references) concentrated

on analytical methods and removal strategies for microplastic in water systems. Vasudeva *et al.*⁴⁹ (265 references) explored spectroscopic techniques and offered insights into metal adsorption on nano-/microplastics. Each review highlights a distinct aspect of microplastic research, underscoring the multifaceted nature of this environmental issue, the complexities involved in detecting such analytes, and the analytical challenges.

Environmental contaminants are becoming increasingly diverse, requiring analytical techniques to evolve accordingly. One promising approach to extract more comprehensive information from a single sample is the use of *multimodal chemical speciation* techniques. Kato *et al.*⁵⁰ (104 references) published a detailed tutorial review, serving as an introductory guide to this emerging field, that focused on the simultaneous application of high-resolution molecular and atomic MS for both target and non-target analytes. The review outlined the principles, strengths, and limitations of various MS techniques and discussed strategies for optimizing split-stream detection setups following chromatographic separation. The potential of this approach was illustrated through a case study involving turtle liver, and the authors also presented advanced data evaluation strategies to support broader adoption in environmental, biological, and pharmaceutical research.

3.2. Reference materials

Certified reference materials are fundamental for quality assurance, but the availability of such materials particularly for matrices containing organometallic compounds remains limited. To address this gap, Lu and co-workers from the National Institute of Metrology in China⁵¹ developed two aqueous CRMs containing different levels of trimethyllead: GBW(E)080971 ($92.73 \pm 3.15 \mu\text{g g}^{-1}$) and GBW(E)080972 ($0.740 \pm 0.030 \mu\text{g g}^{-1}$), that were traceable to GBW 08619 (standard solution of Pb), ensuring unbroken traceability to SI units.

Reference materials are essential to support analysts in regulatory contexts by providing a basis for reliable and comparable data. This need is particularly evident with the increasing demand to quantify *nanomaterials in the aquatic environment* based on particle number, which calls for the development of number-based standards. Addressing this gap LGCQC5050, a number-based RM consisting of 30 nm colloidal gold NPs suspended in deionized water specifically designed for use in sp-ICP-MS, was developed.⁵² In addition to characterizing the material using the dynamic mass flow method with sp-ICP-MS, the authors shared their experiences with the production, storage, and transportation of nano RMs, providing guidance for future developments in compliance with ISO 17034.

3.3. Sample preconcentration and matrix removal

The most significant advances in *analyte preconcentration* for water analysis are summarised in Table 6 (solid-phase extraction) and Table 7 (liquid-phase extraction).





Table 6 Preconcentration methods using solid phase extraction for the analysis of water

| Analytes | Matrix | Technique | Substrate | Coating or modifier | LOD in $\mu\text{g L}^{-1}$ (unless stated otherwise) | Method validation | References |
|--|--|-----------|--|--|--|---|------------|
| Ag^{I} , Pd^{II} | Tap, river, waste, sea and mining water, soil | FAAS | $\text{SiO}_2/\text{MMWCNT}$ | 8-HQ-HCHO-TU polymer | 0.2 (Ag), 0.5 (Pd) | 206 BG 326 (ore polymetallic gold Zidarovo-PMZrZ) | 288 |
| As^{III} | Tap, river, waste and well water | ICP-AES | Glycidyl methacrylate modified magnetic NPs | Cystamine dihydrochloride | 0.050 | GBW08666 (arsenious acid solution), GBW08667 (arsenic acid solution) | 289 |
| As^{III} , As^{V} , DMA, MMA | Tap, bottled and geothermal water, urine | LC-ICP-MS | agarose fibers | FeNP | 0.10 (As^{III}), 0.25 (As^{V}), 0.01 (DMA), 0.37 (MMA) | NIST SRM 2669 (arsenic species in frozen human urine), NIST SRM 1643a (trace elements in natural water) | 290 |
| As^{V} | Fortified water | EDXRF | Amino functionalized Zr-based metal organic framework (UiO-66-NH2) on carbon cloth | — | 0.790 | Spike recovery (water) | 291 |
| Au^{III} , Pd^{II} | Tap, river and sea water | FAAS | Silica gel | <i>N</i> -((6-(2-thienyl)pyridin-2-yl) methyl)propan-1-amine | 0.038 (Au), (1.04) Pd | Spike recovery (water) | 292 |
| Bi | Tap and spring water | FAAS | $\text{Ni}(\text{OH})_2$ nanoflowers | — | 2.8 | NIST SRM 1643f (trace elements in fresh water) | 293 |
| Cd^{II} | Tap, mineral, river, sea water and vegetables | FAAS | Benzophenone | — | 0.4 | NIST SRM 1643d (trace elements in water) | 294 |
| Cd^{II} | Tap, farming, water, food samples | FAAS | Magnetic Cu_2O nanocubes | — | 0.12 | IRMM CRM BCR 505 (estuarine water (trace elements)), NIST SRM; 1577b (bovine liver) | 295 |
| Cd^{II} | Tap and waste water, tobacco, food samples | FAAS | MWCNT@ TiSiO_4 | — | 0.053 | NACIS CRM NCS ZC 73033 (scallion), NIST 1570a (spinach leaves), IRMM CRM BCR-505 (estuarine water (trace elements)) | 296 |
| Cd^{II} , Co^{II} , Ni^{II} , Pb^{II} , Zn^{II} | Tap and bottled water, milk, juice | FAAS | Silica gel | (<i>E</i>)- <i>N</i> '((2-butyl-4-chloro-1 <i>H</i> - imidazole-5-yl)methylene) isonicotinohydrazide | 1.48 (Co), 2.97 (Cd), 3.17 (Ni), 1.62 (Pb), 1.55 (Zn) | Spike recovery (water) | 297 |
| Cd^{II} , Pb^{II} | Sea, bottled, tap and mineral water | FAAS | ZnO NPs | Fe_3O_4 | 7.86 (Cd), 2.36 (Pb) | Spike recovery (water) | 298 |
| Cd, Co, Cu, Ni, Pb | Water, Chinese herbal medicine | ICP-MS | Thione and amine groups-rich magnetic COF | — | 0.00026 (Cu), 0.00016 (Cd), 0.00025 (Pb), 0.00008 (Co), 0.00017 (Ni) | Spike recovery (water) | 299 |
| Cd, Cu, Ni, Pb, Zn | River, tap and high salt matrix simulated water | SCGD-AES | DIAION™ CR20 | — | 0.6 (Cd), 0.6 (Cu), 2 (Ni), 6 (Pb); 2 (Zn) | GBW08608 (metal elements (Cd, Cr, Cu, Ni, Pb and Zn) in water) | 300 |



Table 6 (Contd.)

| Analytes | Matrix | Technique | Substrate | Coating or modifier | LOD in $\mu\text{g L}^{-1}$ (unless stated otherwise) | Method validation | References |
|---|---|------------|--------------------------------------|--------------------------------------|---|--|------------|
| Co, Cu, Ni, Pb | Dam, river and lake water, industrial effluent | FAAS | Fe_3O_4 NPs | Carboxymethyl- β -cyclodextrin | 0.14 (Co), 0.55 (Cu), 0.5 (Ni), 1.38 (Pb) | ECCC CRM TMDA 64.3 (a trace metal fortified sample, lake water) | 301 |
| Cr^{III} | Tap, mineral and waste water | FAAS | Acid activated perlite | <i>Pichia kudriavzevii</i> (JD2) | 4.8 | RM SPS-WW1 (waste water) | 302 |
| Cr^{VI} | Tap and deionized water | ICP-AES | Polyurethane foam | Sol-gel-functionalized | Not calculated | Spike recovery (water) | 303 |
| Cu^{II} | Waste and tap water, tea | FAAS | MnSb_2O_6 NPs | Fe_3O_4 | 2.1 | Spike recovery (water) | 304 |
| Cu^{II} | River, tap and waste water, food samples | FAAS | MnO_2 nanowires | — | 2.9 | IRMM CRM BCR-505 (estuarine water (trace elements)), NIST SRM 1573a (tomato leaf) | 305 |
| Pb^{II} | Tap and river water, food samples | GFAAS | Cu^{II} -nanocluster | Folic acid-capped | 0.014 | Spike recovery (water), NIST SRM 1515 (apple leaves) | 306 |
| Pb^{II} | River water, food samples | GFAAS | TU@MOF-199 | — | 0.0005 | Spike recovery (water) | 307 |
| Se^{IV} | Tap, river, mineral, spring and waste water | UPLC-DAD | MIL-125-NH ₂ MOF | — | 0.013 | Spike recovery (water) | 308 |
| Tl^{I} | Tap, spring, river and sea water | EDXRF | Sepolite nanomaterial | Prussian blue | 0.057 | Spike recovery (water) | 309 |
| U | Ground, river, tap and lake water | ICP-MS | C18-Disc | 1-(2-Thiazolylazo)-2-naphthol | 1.5 | ECCC CRM TMDA-52.4 (a trace metal fortified sample, lake water) | 310 |
| Volatile metal organics (As, Hg, I, Sn, Sb) | Waste water | TD-MIP-AES | Stableflex 85 μm | — | 0.016 (Bu_3SnCl), 0.025 (SbH_3), 0.0067 (MeHgCl), 0.0052 (Hg_0) | IRMM CRM ERM-CA 011a (hard drinking water), IRMM CRM ERM CC580 (estuarine sediment) | 311 |
| Zn | Environmental water, food samples | ICP-AES | NiO nanoflower | — | 0.77 | NIST SRM 1573a (tomato leaves), spike recovery (environmental water, waste water) | 312 |
| Zn | Tap water | EDXRF | Fe_3O_4 NP | 1-(2-Pyridylazo)-2-naphthol | 450 | Spike recovery (water) | 313 |



Table 7 Preconcentration methods using liquid phase extraction for the analysis of water

| Analytes | Matrix | Technique | Method | Reagents | LOD in $\mu\text{g L}^{-1}$ (unless stated otherwise) | Method validation | References |
|-------------------------------------|---|--------------------------------|--------|--|---|---|------------|
| Al (bioavailable) | River and lake water | ETAAS | VALLME | Salicylaldehyde 4-picolinhydrazone and sodium dodecyl sulfate | 0.015 | Spike recovery | 314 |
| Au | Water, sediment, acid and ornaments | FAAS | DLLME | Bis (salicylaldehyde)ethylenediimine, NaNO_3 , CHCl_3 , and ACN | 1 | Spike recovery | 315 |
| Cd ^{II} | Tap, bottled, pond and waste water | FAAS | LLME | <i>Tetra-n</i> -butylammonium bromide and decanoic acid | 0.7 | SPS RM WW2 (waste water level 2) | 105 |
| Cd ^{II} , Ni ^{II} | Waste and mineral water, food samples | FAAS | DLLME | DES-based ferrofluid | 15 | Spike recovery | 316 |
| Co | River water | ETAAS | DLLME | 2-(5-Bromo-2-pyridylazo)-5-dimethylaminobenzen-amine, 1-hexyl-3-methylimidazolium hexafluorophosphate, and ACN | 0.026 | Spike recovery | 317 |
| Cu | Tap water, tea | FAAS | LPME | Diphenylcarbazide in EtOH and 1,2-dichloroethane | 1.6 | Spike recovery | 318 |
| Hg ^{II} | Tap water | Fluorescence Spectrophotometer | VALLE | Chloroform, 2,2'-bipyridyl and Rose Bengal | 6.06×10^{-9} M | Spike recovery | 319 |
| Pb | Drinking water | ETAAS | SFODME | 1-Hexyl-3-methylimidazolium hexafluorophosphate and 1-dodecanol | 0.075 | NRCC CRM AQUA-1 (drinking water certified reference material for trace metals and other constituents) | 320 |
| Th ^{IV} | Sea, ground, lake and river water | TXRF | CPE | Bis(phosphoramidate) and sodium dodecyl sulfate | 0.1 | Spike recovery | 321 |
| Tl | Mineral and river water | FAAS | LPME | Ammonium pyrrolidine dithiocarbamate and diisobutyl ketone | 2.1 | NIST SRM 1643e (trace elements in water) and SRM 2704 (buffalo river sediment) | 322 |
| Zr ^{IV} | Tap, ground and waste water, rock samples | ICP-AES | CPE | CTAB, Eriochrome cyanine R and Triton X-114 | 0.5 | Spike recovery | 323 |

3.4. Speciation

Ion chromatography coupled with an elemental detector is a powerful technique for the sensitive species-specific determination of cations and anions in water samples. In this context⁵³ an IC was coupled with ICP-AES to determine oxyhalide bromine and various chlorine species in artificial water samples. Using an optimized method, the target analytes were successfully separated and detected within 24 min. Notably, Br^- and ClO_3^- could not be resolved by IC with conductivity detection but differentiation was possible using an elemental detector, allowing the quantification of all target analytes. The method was validated using spiked water samples, achieving recoveries between 95% and 105%. The LODs were $32 \mu\text{g L}^{-1}$ for Br^- , $60 \mu\text{g L}^{-1}$ for BrO_3^- , $34 \mu\text{g L}^{-1}$ for Cl^- , $91 \mu\text{g L}^{-1}$ for ClO_2^- , and $150 \mu\text{g L}^{-1}$ for ClO_3^- . Further optimization would be required to lower the LODs to meet regulatory drinking water limits. Anions such as iodine and bromine play a crucial role in polar atmospheric chemistry. Their accurate determination is essential, although challenging due to their typically low concentrations. To meet these challenging analytical requirements, Frassati *et al.*⁵⁴ coupled an IC system with ICP-MS. This setup achieved exceptional LODs of 0.4 pg g^{-1} for I^- , 0.8 pg g^{-1} for IO_3^- , 4 pg g^{-1} for Br^- , and 1 pg g^{-1} for BrO_3^- , which the authors claimed to be 30 times lower than previously reported. The separation was completed in 1500 s and successfully applied to various snow samples. An IC-ICP-MS method was developed⁵⁵ for the speciation of polyphosphonates and their transformation products in surface waters. For method optimisation, nine analytes were separated in approximately 200 s with species-specific LODs of $0.06 \mu\text{g L}^{-1}$ (2-aminoethylphosphonate), $0.6 \mu\text{g L}^{-1}$ (aminomethylphosphonic), $0.12 \mu\text{g L}^{-1}$ (glyphosate), $0.13 \mu\text{g L}^{-1}$ (phosphate), $0.14 \mu\text{g L}^{-1}$ (iminodi(methylene phosphonate)), $0.14 \mu\text{g L}^{-1}$ (phosphonoacetic acid), $0.41 \mu\text{g L}^{-1}$ (aminotris(methylene phosphonate)), $0.49 \mu\text{g L}^{-1}$ (diethylenetriaminepenta(methylenephosphonate)) and $0.73 \mu\text{g L}^{-1}$ (ethylenediaminetetra(methylene phosphonate)). Further in the study a simulated sample was produced by oxidising diethylenetriamine penta(methylenephosphonate) with MnO_2 for 28 h and then analysed using the optimised method. Besides the original species, eleven transformation products were separated, of which only two were positively identified. This highlights both the analytical power of the method and the need for further research in this area.

The *speciation of trace elements by HPLC-ICP-MS* remains an important topic. Antimony is released into the environment through various natural and anthropogenic activities. Due to its four different oxidation states, each with distinct behaviours and toxicities, speciation plays a key role in understanding its environmental pathways and assessing its toxicity. Chen and co-workers⁵⁶ developed a HPLC-HG-MC-ICP-MS method that enabled the identification of Sb species and determination of their isotopic compositions, significantly enhancing the amount of information that could be extracted from a single sample. The precision of the method was improved by using the linear regression slope method and In as external standard correction, reaching a precision $<0.05\%$ (2 s). The method was

validated against synthetic solutions and CRMs NIST SRM 3102a (antimony standard solution), IGGE GSD-11 (stream sediment) and GSD-12 (stream sediment) as well as applied to different types of environmental water. Tellurium is another element that occurs naturally at low concentrations but due to anthropogenic activities, its presence in the environment is increasing. Given that toxicity is dependent on its oxidation state, speciation of Te has become increasingly important. In this context, an HPLC-ICP-MS method using a reversed-phase C18 column was developed⁵⁷ for the determination of Te^{IV} and Te^{VI} . The optimized method achieved LODs of 1.4 ng g^{-1} for Te^{IV} and 0.5 ng g^{-1} for Te^{VI} . Calibration was performed using NMJJ CRM 3630-a (Te standard solution Te(1000)) as the source of Te^{IV} , while an in-house standard was used for Te^{VI} . The method was then applied to river water and various seawater samples. One of the most widely investigated species systems in the aquatic environment is the $\text{Cr}^{\text{III}}/\text{Cr}^{\text{VI}}$ system, but many approaches are not thoroughly validated. Pechancová *et al.*⁵⁸ employed a bottom-up approach to evaluate MU in characterizing and validating their IEC-ICP-MS method for Cr speciation in natural waters. The optimized, rapid method enabled separation within 1.5 min and achieved LODs of $0.98 \mu\text{g L}^{-1}$ for Cr^{III} and $0.1 \mu\text{g L}^{-1}$ for Cr^{VI} . Comprehensive method validation was performed, including assessments of Cr species interconversion, quantification of uncertainty components, and verification of the developed MU model. Additionally, the method was validated for LOD, LOQ, trueness, repeatability, intermediate precision, selectivity, and carryover for both Cr^{III} and Cr^{VI} using isotopically enriched CRMs. This results in a fully characterized and robust analytical method, an increasingly rare achievement in the current scientific literature.

3.5. Nano- and micromaterials

Polymers play a crucial role in our daily lives, but one of their downsides is that their debris contaminates aquatic environments. A major concern in this context is the *presence of micro- and nanoplastic particles*. While sp-ICP-MS is a widely used technique for the detection of carbon-based microparticles, its lower and upper particle size limitations remain significant drawbacks. Sandro *et al.*⁵⁹ successfully overcame the upper size limitation of sp-ICP-TOF-MS for various types of plastics (PS, PMMA, PVC), extending the detectable range up to $20 \mu\text{m}$. This advancement was made possible by utilizing a gravity-fed down-pointing ICP source. In the case of $4 \mu\text{m}$ PVC particles, the authors were able not only to quantify particle size but also to identify the polymer type by detecting the concurrent Cl and C signal. Laser ablation ICP-MS for the analysis of plastic particles is also gaining attention but as with sp-ICP-MS, the availability of suitable RMs is limited. This challenge was addressed by developing⁶⁰ a RM consisting of a thin PS film (thickness: 150 nm) deposited on a silicon wafer using spin-coating. Certified particle standards (PS, PMMA, PVC) in the size range of $2\text{--}5 \mu\text{m}$ were then accurately characterized, achieving a size accuracy of $\leq 6.3\%$. Sample preparation on a silicon wafer, with solvent evaporation at 80°C , also facilitated the size detection of microplastic particles in aquatic samples.



In recent years, a relatively new approach has gained increasing attention: the determination of *isotopic ratios within micro- and nanoparticles*, which could help trace the source of the particles in aquatic bodies and determine whether they are of anthropogenic or natural origin. In this regard, three different isotopic systems ($^{153}\text{Eu}/^{151}\text{Eu}$, $^{142}\text{Ce}/^{140}\text{Ce}$, and $^{176}\text{Lu}/^{175}\text{Lu}$) were investigated⁶¹ in commonly used, commercially available PS calibration beads for CyTOF, using two different ICP-TOF-MS systems (CyTOF Helios and icpTOF 2R). This study found that the measured results closely matched the theoretical values, with the icpTOF 2R delivering slightly better performance. However, as the RSD for the icpTOF 2R measurements ranged from 6% to 19% for the investigated systems, and no correction of instrumental isotopic fractionation was applied, the results indicate that further research is necessary if precise isotopic ratios in the ‰ range or better are required. Manard *et al.*⁶² conducted a comparative study using both MC-ICP-MS and ICP-TOF-MS for the isotopic analysis of NdVO₄ NPs (*ca.* 100 nm diameter). For the investigated isotopic systems, $^{142}\text{Nd}/^{144}\text{Nd}$, $^{143}\text{Nd}/^{144}\text{Nd}$, $^{145}\text{Nd}/^{144}\text{Nd}$, $^{146}\text{Nd}/^{144}\text{Nd}$, and $^{148}\text{Nd}/^{144}\text{Nd}$, they reported relative differences ranging from −20% to 0.7% for the sp-ICP-TOF-MS system, and from −2.4% to 3.9% for sp-MC-ICP-MS, relative to bulk MC-ICP-MS measurements after digestion of the NPs. In both approaches, the RSDs of the isotopic ratios were within the higher percentage range (3–26% for the sp-ICP-TOF-MS approach and 6–23% for the sp-MC-ICP-MS approach). A further study investigated⁶³ $^{142}\text{Ce}/^{140}\text{Ce}$ isotopes in CeO₂ NPs using sp-MC-ICP-MS, aiming to optimize the procedure for improved precision and accuracy. The FC integration time (ranging from 50 to 500 ms) and various ratio calculation methods were evaluated. The optimized method led to a reduction in percent relative differences and RSDs, although the values remained within the low percent range. The results demonstrate the potential of sp-MC-ICP-MS for isotopic analysis at the single-particle level, but also indicate that, for isotopic systems showing variability in the low δ -range, further improvements are necessary to achieve the precision and accuracy required.

With the ever-growing field of detection of nano- and microparticles in the aquatic environment, the range of *sample introduction systems used, and calibration strategies followed* has significantly expanded. To provide the scientific community

with an overview of the possibilities and limitations of various calibration approaches for sizing micro- and nanoparticles, Bazo *et al.*⁶⁴ evaluated different intensity-based and time-based methodologies for sp-ICP-MS using AuNPs (20–70 nm) and SiO₂NPs (100–1000 nm). The authors concluded that the highest accuracy was achieved with transport efficiency (TE) independent, intensity-based methods. A further study evaluated⁶⁵ the TE dependency on the particle size using SiO₂ particles ranging from 500 to 5000 nm and Au particles ranging from 60 to 1500 nm. A dramatic decrease in TE was reported once particle sizes exceeded approximately 700 to 800 nm highlighting the importance of determining TE using particles similar in size to the samples. A systematic study on various low-consumption sample introduction systems for their suitability and performance in sp-ICP-MS was conducted by Priede *et al.*⁶⁶ In this study, various combinations of spray chambers (three different types) and nebulizers (four different types) were investigated. The results showed that the desired TE of 100% was not achieved with any nebulizer/spray chamber combination. The study reinforced that careful selection of particle standards is essential. Besides the commercially available nebulizer/spray chamber combinations the development⁶⁷ of a novel miniaturized ultrasonic nebulization introduction system was reported. This system enables the determination of low particle concentrations, such as those found in surface waters, due to its high TE of approximately 80% when 60 nm and 100 nm Au NPs were used to evaluate its performance.

3.6. Instrumental analysis

3.6.1. Atomic absorption spectrometry and atomic emission spectrometry. Li *et al.*⁶⁸ developed a novel *portable device* that combined an absorption and emission spectrometer which consisted of a single syringe for sample introduction, a tungsten coil as the atomizer, an exchangeable HCL for AAS, and two CCDs as detectors. For validation, different water CRMs were used, and no significant differences were observed with the certified values (*t*-test, *p* < 0.05). Elements such as Cr, Cu, In, and V were determined by AAS whilst Ba, Cr, Cu, Fe, Mg, Mn, Ni and V were detected by AES. The newly developed instrument was successfully applied to the analysis of various water samples, including tap, surface, river, and formation water. Similarly, a portable AES-based device for the quantification of

Table 8 Photochemical vapour generation methods for the analysis of water

| Analytes | Matrix | Technique | Reagents | LOD in $\mu\text{g L}^{-1}$ (unless stated otherwise) | Method validation | References |
|-----------|------------------------|---------------------|--|--|---|------------|
| Hg | River, tap, well water | $\mu\text{APD-AES}$ | Formic acid (8% (m/m)) | 0.33 | Spike recovery | 324 |
| Rh | Lake and river water | ICP-MS | 10 M formic acid, 10 mg L^{-1} Cu, 5 mg L^{-1} Co, and 50 mM NaNO ₃ | 13 pg L^{-1} | NRCC CRM AQUA-1 (drinking water) and SLRS-6 (river water) | 325 |
| Br, Cl, I | Various | ICP-MS | Acetic acid (1% (v/v), 20 mg L^{-1} Cu | 0.0063 (Br), 4.2 (Cl), 0.0019 (I) | NIST SRM 1515 (apple leaves), NIST SRM 1549 (whole milk powder), NIST SRM 1632c (trace elements in coal (bituminous)), NRCC CRM DORM-5 (fish protein) | 123 |



Hg employed VG⁶⁹ coupled with a piezoelectric transformer-driven microplasma as the excitation source. This configuration resulted in a compact, lightweight, and robust instrument with low power consumption, allowing field operation that mitigates the risk of instability of Hg in solution when transporting samples back to the laboratory. The system demonstrated a linear range of 0.01–1 mg L⁻¹ and LOD of 2.8 µg L⁻¹. Validation was carried out using spiked spring and river water samples and digests of the CRMs NRCC DOLT-5 (dogfish liver) and the NIMC GBW07405 (soil).

The *determination of TOC* is a key parameter in assessing water quality but most methods are laboratory based. To address this limitation, Liu *et al.*⁷⁰ developed a microchip-based AES method in which the C signal from a liquid electrode discharge microplasma was measured. The method achieved a LOD of 0.15 mg L⁻¹ and an RSD of 4%. Each measurement required only 43 µL of sample and was completed within one minute. Recoveries of spikes ranged from 97% to 102%. The optimized method was successfully applied to determine TOC in both river and seawater samples.

3.6.2. Vapour generation. The most significant advances in *photochemical vapour generation* for water analysis are summarised in Table 8.

3.6.3. Inductively coupled plasma mass spectrometry. The *use of automated on-line matrix separation and analyte pre-concentration* coupled to ICP-MS reduces interferences and improves limits of quantification. This is especially important for highly saline matrices such as seawater where historically such steps were carried offline. To refine the process and improve direct coupling with ICP-MS, Kuo and Su⁷¹ utilized 3D printing that extended into four-dimensional printing where the 4th dimension was the use of smart materials that respond to external stimuli and can change their structure over time. Their design featured two H⁺-responsive, flow-actuated needle valves with the SPE material in between, removing the need for preprogramming timing control. By simply switching from an alkaline sample flow to an acidic eluent Cd, Co, Cu, Mn, Ni, Pb, and Zn were determined in <10 min per sample. Relative errors of ≤2%, MDLs from 0.5 ng L⁻¹ to 5.9 ng L⁻¹ and extraction efficiencies between 98.1% and 99.0% were achieved. For validation, the CRMs NRCC CASS-4 (nearshore seawater), NRCC SLRS-5 (river water), NIST SRM 1643f (trace elements in water), and the RM SeronormTM L-2 (trace elements in urine) were used. Tong *et al.*⁷² used the commercially available automated system ELSPE-2 Precon with a PS-DVB resin to determine REE concentrations in seawater samples. This system, which operates using a multi-valve and multi-syringe-based setup, allowed the analysis of up to 14 samples h⁻¹ consuming <1 mL per sample with a matrix removal efficiency between 99.3% and 100%. For validation, the seawater CRMs NRCC CASS-6 (nearshore seawater), NRCC NASS-7 (seawater) and NMIJ 7204-A (trace elements in seawater (elevated level)) were analysed.

Continuous monitoring of river water can uncover dynamic processes and enable rapid responses to changes in water quality. To achieve this, researchers from the Federal Institute for Hydrology in Koblenz⁷³ have developed a method that facilitates the collection of time-resolved data with an hourly

resolution, integrated into a continuous 24/7 monitoring workflow. They engineered a custom self-cleaning fraction collector rack compatible with a commercially available system, incorporating an automatic dilution and acidification unit following a cross-flow filtration stage. This setup enables the direct sampling and analysis of water from the Rhine River that flows next to the laboratory in Koblenz. The method was optimized for the monitoring of 56 elements. To ensure data quality, CRMs were analysed at defined intervals. Validation of the method was carried out using RMs such as Spectrapure Standards SPS-SW1 and SPS-SW2 (elements in surface waters), as well as ECCC CRMs NWTM-15.3 (water trace elements), NWTM-26.5 (trace elements in water), and NWTMDA-51.5 (fortified lake water). Additional off-line comparative measurements also confirmed the method's accuracy.

New applications and reaction gases for ICP-MS/MS continue to emerge since its introduction in the early 2010s, reflecting the ongoing evolution of this technique. This is particularly beneficial for aquatic samples, where analyte concentrations are often low and measurements suffer from interferences. A cell gas tested for its suitability in ICP-MS/MS was benzene in helium.⁷⁴ This proof-of-concept study demonstrated that benzene is a promising reaction gas for certain elements, such as S and Se, where it significantly enhances the performance by reducing the impact of spectral overlaps of the ICP-MS/MS system. Building on previous work reported in last year's update,⁷⁵ researchers from the Pacific Northwest National Laboratory^{76,77} investigated the suitability of NO as a cell gas for various elements. During these studies, they examined the impact of impurities in the NO gas and found that using purified NO led to an increased sensitivity. Additionally, the use of purified gas facilitated the use of higher flow rates, which further improved interference removal. These findings emphasized the critical importance of using high-purity gases in the reaction cell of an ICP-MS/MS instrument to minimise unwanted side reactions. In some cases, even gases rated as high-purity (*e.g.* 5N grade) may require further purification, as trace contaminants, such as water, can adversely affect analytical performance.

Another field that benefits from progress in ICP-MS/MS is *the determination of isotopic ratios*. While MC-ICP-MS is the gold standard for isotopic ratio measurements, MS/MS systems are being explored to make isotopic analysis more accessible. Schlieder *et al.*⁷⁸ optimised an ICP-MS/MS method using O₂ for the determination of the chlorine isotopic ratio. The method was validated using the NIST SRM 975a (isotopic standard for chlorine) in ultrapure water reaching an accuracy of 0.1%, a precision of 1% and a LOD of 3.4 ng g⁻¹.

Isotope ratio determinations in seawater are one of the most challenging applications. Li *et al.*⁷⁹ employed UNDBD VG for sample introduction with MC-ICP-MS to determine the ¹⁴³Nd/¹⁴⁴Nd isotopic ratio. They corrected for the mass-dependent fractionation by applying the exponential law using the ¹⁴⁶Nd/¹⁴⁴Nd ratio. With the optimized method, the ¹⁴³Nd/¹⁴⁴Nd isotopic ratio was determined at Nd concentrations as low as 0.5 µg L⁻¹ using only 600 µL of sample, and thus the method requires only an enrichment factor of approx. 1000,



given that typical Nd concentrations in seawater range from 0.38 to 2.55 ng L⁻¹. To validate the method, two NIMC CRMs GSB 04-3258-2015 and GBW04440 (Nd isotopic standard solutions), were analysed. Application to real seawater samples further demonstrated the suitability of this approach for trace-level isotopic analysis in complex marine matrices.

3.6.4. X-ray fluorescence spectrometry. With a salinity of around 35 g L⁻¹, seawater is one of the most challenging matrices in water analysis, and the determination of trace elements requires robust and selective methods. Wiggershaus *et al.*⁸⁰ developed a TXRF method for the direct determination of Co, Cr, Cu, Fe, Mn, Ni, and Zn in artificial seawater. By drying the sample on a glass carrier (10 µL, 2 min drying time on a hot plate) they removed the need for laborious sample pretreatment, and with a 500 s measurement time they could determine concentrations ranging from 0.1 to 1 mg L⁻¹. With the optimised method, an RSD below 1% was achieved for repeated measurements on the same glass carrier.

3.6.5. Laser-induced breakdown-spectroscopy. Although LIBS is a well-established technique for rapid and reliable elemental analysis of solid samples, when applied to aqueous samples, *conversion to a solid form* is often crucial. A simplified and efficient surface-enhanced LIBS approach was described⁸¹ to improve detection of Cr, Cu, and Pb in aqueous solutions. To boost sensitivity, the researchers polished the aluminum substrate (with 2000-mesh sandpaper). This combined the natural surface-enhancing properties of aluminium and significantly reduced the coffee-ring effect during drying. As a result, the method achieved low LODs of 1.02 ng mL⁻¹ for Cr, 1.23 ng mL⁻¹ for Cu, and 3.26 ng mL⁻¹ for Pb. In an alternative approach,⁸² nanoporous borosilicate glass with an average pore size of 4 nm and a porosity of 30% enabled homogeneous sample distribution after rapid drying of only 2–3 µL of sample. The LODs for Ag, Ba, Cu, and Sr were *ca.* 2 µg L⁻¹ with RSDs of ≤7%, and a dynamic range of *ca.* three orders of magnitude. For the sensitive detection of P in water, Zhang *et al.*⁸³ dried and preconcentrated samples onto a graphite substrate, achieved LODs of 0.009 mg L⁻¹ and 0.23 mg L⁻¹ when measured at the P 213.6 nm and 214.9 nm atomic emission lines. The optimized LIBS approach achieved a relative error of ≤12%, comparable to that of ammonium molybdate spectrophotometry in real-world water samples.

While the approaches above required ablating samples from a solid substrate, Chen *et al.*⁸⁴ developed a LIBS method for the *direct determination of metals in water* using a fs laser to significantly reduce the splashing and plasma quenching effects associated with ns lasers. The optimised method resulted in LODs in the ng L⁻¹ range for Cr, Cu and Pb with RSDs <4% and *r*² values >0.99, for calibrations ranging from 10–400 µg L⁻¹, indicating potential for real-time monitoring of metal contamination in water. To avoid splashing effects in ns-LIBS, Xiong *et al.*⁸⁵ generated a high-temperature plasma at a needle tip where the nebulised sample solution was effectively atomised, achieving LODs of 43 mg L⁻¹ for Cu, 58 mg L⁻¹ for Cr, and 51 mg L⁻¹ for Mn. The authors emphasized that this system can be readily integrated into online monitoring setups for real-time measurements in the field.

4. Analysis of soils, plants and related materials

4.1. Review papers

Numerous reviews featured *the determination of particular elements or radionuclides*. Tanaka *et al.*⁸⁶ (43 references) provided an overview of approaches for As speciation analysis, a topic also covered by Chung⁸⁷ (84 references). The measurement of Pu in environmental and biological samples was discussed by Sharma *et al.*⁸⁸ (168 references) and by Wang *et al.*⁸⁹ (123 references), both of whom included atomic spectrometry alongside radiometric techniques. Chaudhry *et al.*⁹⁰ (98 references) focussed on methods for the determination of Li; Mogashane *et al.*⁹¹ (207 references) on P; and Yu *et al.*⁹² (83 references) on U. Sample pretreatment, purification and measurement of ¹²⁹I and ¹³¹I was discussed by Ren *et al.*⁹³ (153 references).

A useful tutorial review⁹⁴ (107 references) on *methods for the assessment of PTE contamination in soils* first covered sample preparation and extraction methods and then gave an overview of a variety of atomic spectrometry techniques (AFS, ETAAS, ICP-AES, ICP-MS, and use of a direct mercury analyser). Common risk assessment indices, such as the PLI and PERI, were also described.

The impact of metallic NPs in plants is a topic of increasing concern. Developments in the characterisation and determination of such particles over the past 20 years by techniques including AFM, CE-ICP-MS, FFF-ICP-MS, HPLC-ICP-MS, LA-ICP-MS, sp-ICP-MS, TEM/SEM, XANES and µXRFS were reviewed⁹⁵ (125 references) and progress in the understanding of NP uptake, accumulation and toxicity summarised. The authors emphasised the need for better integration of quantitative and qualitative analysis with computer modelling and theoretical frameworks to improve knowledge of NP-plant interactions.

4.2. Reference materials

The development of *NIST SRMs for dietary supplement ingredients* – many of which are of plant origin *e.g.* ginger, kelp – over the past 20 years was reviewed⁹⁶ (142 references). It was noted that relatively few botanical dietary supplement ingredient RMs/SRMs possessed assigned values for trace elements, in particular the toxic elements As, Cd, Hg and Pb, meaning laboratories typically use other less closely matrix-matched botanical SRMs for QC purposes such as 1515 (apple leaves) or 1575 (pine needles). The authors recommend additional trace element profiling in existing botanical dietary supplement RMs/SRMs, highlighting the useful work of Sam *et al.* who had recently published⁹⁷ As, Cd, Hg and Pb concentrations in 34 such materials.

New stable isotope ratio values were reported⁹⁸ for δ^{142/140}Ce in 22 Chinese RM's, nine of which were soils. Samples were digested in acid, purified using a single column separation, and analysed by MC-ICP-MS using SSB and Sm addition, where the ¹⁴⁹Sm/¹⁴⁷Sm ratio was used to correct the measured δ^{142/140}Ce values. A novel three-step sequential chromatographic separation⁹⁹ enabled multi-elemental isotopic analyses by MC-ICP-MS to be carried out on 57 RMs that included soils, sediments and



plants. Values for $\delta^{60}\text{Ni}$ in 44 materials, for $\delta^{65}\text{Cu}$ in 24 materials and for $\delta^{66}\text{Zn}$ in 17 materials were reported for the first time.

4.3. Sample preparation

4.3.1. Sample dissolution and extraction. *Reviews on preparation methods* included that of Ferreira *et al.*⁹⁴ (107 references), which covered procedures for the determination of As, Cd, Pb, Hg, and Sb in soil. The broad review discussed sampling and storage, advantages and drawbacks of heating and drying methods, and acid mixtures for MAE. Quantification techniques including AAS, AFS, ETAAS, ICP-AES and ICP-MS were also covered. Potential health risks associated with the increasing use of nuclear energy was the driver for the reviews of Ren *et al.*⁹³ (153 references), which focused on methods for the determination of ^{129}I and ^{131}I , and Sharma *et al.*⁸⁸ (168 references), which reviewed methods for Pu speciation. Traditional acid and alkaline digestion, pyrolytic procedures, solvent extraction and ion exchange purification methods were covered by both reviews, while Sharma *et al.* also considered flow injection and sequential injection methods and challenges in isotopic fingerprinting. Both sets of authors concluded that improvements were needed in the sensitivity and accuracy of existing methods. Lack of accuracy was also highlighted in the review by Chung⁸⁷ (84 references) on speciation of As in foodstuffs including plants and grains. Interconversions between MMA and DMA and their thiolated counterparts in sulfur-containing matrices were commonly observed in extractions performed with dilute HNO_3 , resulting in over or under estimation of the species. Enzymic extractions were more favourable for species preservation. Addressing knowledge gaps in metabolite interconversions and the need for RMs certified for thiolated species were emphasized.

Contributions to *extraction methods for soils and plants* primarily considered the efficiency and optimisation of existing methods. Gürbüz¹⁰⁰ studied the efficiency of the Mehlich-3 reagent, ammonium bicarbonate-DTPA, the modified Morgan reagent, acid ammonium acetate-EDTA, and water, for the determination of phytoavailable B, Ca, Cu, Fe, K, Mg, Mn, P, S and Zn in 130 neutral and alkaline soils, benchmarked against more widely-applied extractants such as ammonium acetate and DTPA. Correlations between concentrations were ranked by means of TOPSIS (technique for order of preference by similarity to ideal solution). This multi-criteria decision-making technique identified ammonium bicarbonate-DTPA as the most effective extractant. Lopez *et al.*¹⁰¹ optimised acid volume, temperature and extraction time using a Box Behnken experimental design for the MAE of Ca, Fe, K, Mg and Na in mushrooms prior to quantification by FAAS (Mg, Fe) and ICP-AES (Ca, K, Na). Optimised conditions for a 0.5 g sample were addition of 1 mL H_2O_2 + 5 mL HNO_3 , and extraction at 198 °C for 10 min. Relative measurement errors ranged from -4.5% (Na) to +7.3% (Mg) in RM INCT-TL-1 (tea leaves), precision was <10%, and LODs ranged from 0.005 mg L⁻¹ (K) to 0.079 mg L⁻¹ (Ca).

An *UAE for multielement determination in lignocellulose* was proposed¹⁰² as an alternative to the standard EN ISO 16967 MAD method which uses harsh conditions and reagents to digest this

notoriously resistant matrix. Optimal conditions were an ultrasound frequency of 45 kHz, acoustic amplitude 70%, a temperature of 50 °C, extraction time 30 min, and 20 mL of 1 M H_2SO_4 . No significant differences were observed between concentrations of Ca, K, Mg, Mn, Na, P, Sr, Zn determined in sugarcane bagasse, and eucalyptus and pine wood residue biomass under these milder extraction conditions compared to the standard method (Student's *t*-test, 95% CI). However, extractions of Al, Ba, and Fe were poor.

Deep eutectic solvents continue to be explored as milder and greener alternatives to traditional reagents Zhang *et al.*¹⁰³ prepared four DESs based on guanidine hydrochloride, fructose, glycerol, citric acid, proline and choline chloride, and used them for the MAE extraction of Se from rice for determination by ICP-MS. Component ratios were optimised based on density and viscosity measurements. Concentrations of Se extracted by two of the DESs – one composed of 34% guanidine hydrochloride, 21% fructose, 45% water, and the other composed of 30% choline chloride, 25% citric acid, 45% water – were significantly higher than MAD with HNO_3 and H_2O_2 . However, the number of samples tested was not specified and the DES extraction time was relatively long at 45 min. Ferreira *et al.*¹⁰⁴ reported that the extraction efficiencies of DESs were dependent not only on DES composition, but also on the preparation method. Three DESs were each prepared by two different methods: stirring without heating, and rotary evaporation under reduced pressure. The preparation method was found to affect both the viscosity and the melting point of the solvents. When used for MAE, the extraction efficiency for As, Cd and Pb in plant material was also influenced by the preparation method, indicating a need for further studies on the influence of component interactions.

4.3.2. Analyte separation and preconcentration. In *methods for LLME*, rapid extraction and concentration of Cd in acidic plant digests was achieved¹⁰⁵ using a hydrophobic DES without chelating or dispersing agents. The DES, based on *tetra-n*-butylammonium bromide and decanoic acid, was easily prepared by simple magnetic stirring of the components at 50 °C for approx. 10 min, and was superior to an alternative DES based on thymol- and menthol-acid combinations. Under optimized conditions (1 g sample, 1000 μL DES, 2 min vortex, 5 min centrifuge at 4000 rpm) an LOD of 0.7 $\mu\text{g L}^{-1}$ was achieved by FAAS. Spike recoveries (0.2 mg L⁻¹ standard solution) ranged from 95 to 98%, and relative measurement errors for RM NCS DC 78302 (Tibet Soil) were between -6.2 and -1.7% (Student's *t*-test, 95% CI, *n* = 3).

In *methods for solid-phase extraction*, Vaezi and Dalali¹⁰⁶ proposed a vortex-assisted extraction using a zeolite imidazole framework adsorbent for the preconcentration of Cd and Co in soil and vegetables, prior to determination with FAAS. However, the analytes were adsorbed (and eluted) separately and, while interferences for a range of other ions were assessed, potential inference of Cd and Co on each other was not considered.

Chen *et al.*¹⁰⁷ proposed a *five-step sequential extraction and procedure for the determination of content and isotopic composition* of B in soil. Readily soluble B was extracted following Sun *et al.*;¹⁰⁸ carbonate-bound B was extracted with 1 M HAc-NaAc (8 mL), 4 h shaking, 30 min centrifugation; organically-bound B





Table 9 Preconcentration methods involving solid-phase (micro)extraction used in the analysis of soils, plants and related materials

| Analyte(s) | Matrix | Technique and extraction mode | Reagent(s) | Findings | LOD ($\mu\text{g L}^{-1}$) | Validation | References |
|----------------|---|-------------------------------------|---|---|---|--|------------|
| Cd | Plants (spinach, tea), water | FAAS temperature induced DSPE | Dithizone chelating agent (1×10^{-4} M), benzoic acid sorbent, ethanol eluent | Digestion 2 g sample, $\text{HNO}_3 + \text{H}_2\text{O}_2$ (2 + 1). Extraction 40 mg sorbent, 50 °C, pH 6. Elution 1 mL | 0.3 | SRM NIST 1643d (trace elements in water), spike recovery (10 and 20 $\mu\text{g L}^{-1}$) | 326 |
| Cd | Plants (leek, lettuce), water | FAAS ion pair solvent assisted DSPE | KI for CdI_4^{2-} anion formation, alkyl dimethyl benzyl ammonium chloride (ADBAC) ion pairing surfactant cation, benzophenone sorbent in ethanol dispersion solvent, ethanol eluent | Digestion 2 g sample, $\text{HNO}_3 + \text{H}_2\text{O}_2$ (2 + 1). Extraction 0.5 mL, 10% (w/v) KI, 0.6 mL ADBAC (1 M) for ion pair formation, 2% (w/v) benzophenone. Elution 1 mL | 0.4 | Spike recovery (10, 20 and 50 $\mu\text{g L}^{-1}$ for water; 0.5 and 1 $\mu\text{g g}^{-1}$ for leek and lettuce; SRM NIST 1643d (trace elements in water) | 294 |
| Co, Cu, Ni, Pb | Plants (cucumber, mint, tobacco leaves), water (dam, effluent, industrial, river) | FAAS VA magnetic SPE | Fe_3O_4 @-carboxymethyl- β -cyclodextrin adsorbent, 2 M HNO_3 eluent | Digestion 0.7 g sample, 10 mL HNO_3 , 95 °C (hotplate). Extraction 20 mg sorbent, pH 7, vortex 3 min. Elution 1 mL. Sorbent recycling up to 13 times | 0.14 (Co), 0.55 (Cu), 0.5 (Ni), 1.38 (Pb) | Spike recovery (0.7, 0.8 and 1 mg L^{-1}); CRM ECCO TMDA 64.3 (supplemented water), CRM INCT-OBT-5 (ornamental basma tobacco leaves) | 301 |
| Hg, Ni, Zn | Beverages, foods (beans, rice, nuts), fruits (banana, orange, strawberry), vegetables (onion, spinach), water | ICP-AES magnetic SPE | <i>Agaricus augustus</i> biosorbent loaded on γ - Fe_2O_3 MNP, 1 M HCl eluent | Digestion 1 g sample, 5 mL $\text{HNO}_3 + \text{HCl}$ (1 + 1) heated (hotplate) till dry, followed by 6 mL $\text{HNO}_3 + \text{HCl} + \text{H}_2\text{O}_2$ (1 + 1 + 0.2) MAD. Extraction 75 mg biosorbent, pH 4. Elution 5 mL. Sorbent cycling up to 30 times | 0.02 (Hg), 0.01 (Ni), 0.02 (Zn) | Spike recovery (5 $\mu\text{g L}^{-1}$), SRM NIST 1643e (simulated fresh water), RM SCP science EU-L-2 (wastewater), RM NWRI EC NWTM-15 (spiked-fortified water), CRMs NACIS NCS ZC73350 (poplar leaves) and NCS ZC73014 (tea leaves) | 327 |
| Ni, Pb | Baby milk, chicken, onion, parsley, potato, rice, tea, tobacco, tomatoes | ICP-AES SPE | <i>Sparassis crispa</i> -loaded hollow mesoporous nano-silica sorbent, 1 M HCl eluent | Digestion $\text{HNO}_3 + \text{HCl} + \text{H}_2\text{O}_2$ (1 + 1 + 0.2) MAD. Extraction 100 mg biosorbent, pH 6. Elution 5 mL. Sorbent cycling up to 25 times | 0.019 (Ni), 0.033 (pb) | CRMs NACIS NCS ZC 73014 (tea leaves) and NCS DC 73350 (poplar leaves), RM NWRI EC NWTM-15 (fortified water) | 328 |

was extracted with 0.02 M CaCl_2 –0.01 M mannitol solution (25 mL), 4 h shaking, and 30 min centrifugation; adsorbed-bound B was extracted with 0.1 M NH_3OHCl –0.01 M HNO_3 (25 mL), 4 h shaking, and 30 min centrifugation. Each step was repeated six times. Residual B was extracted with 5 mL HNO_3 + 1 mL H_2O_2 + 1 mL HF, at 180 °C for 10 h. Extractants from each step were purified using boron-selective resins and isotopic composition was determined by MC-ICP-MS, expressed relative to that of NIST SRM 951 (H_3BO_3). Values of $\delta^{11}\text{B}$ ranged from -31.9 to 25.8‰ ; readily soluble B had the most positive $\delta^{11}\text{B}$ values ($+1.3$ to $+25.8\text{‰}$) but relatively low content while residual B had the lowest $\delta^{11}\text{B}$ values (-31.9 to -24.5‰) and the highest B content. Despite the long processing time, the extraction is of potential interest for studying B cycling and isotopic behaviour.

Organic forms of Hg are of particular concern due to their biomagnification potential. However EtHg is often overestimated following propylation of samples for Hg speciation analysis due to the formation of EtHg artifacts. Wu *et al.*¹⁰⁹ combined CuSO_4 – HNO_3 – CH_2Cl_2 , to remove Hg^{2+} from the derivatisation solution (thereby reducing artifact formation) with propylation to allow accurate quantification of EtHg . The approach offered recoveries of between 81 and 86%, with artifact levels $<\text{LOD}$ ($1.98 \times 10^{-4} \text{ ng g}^{-1}$), and gave comparable results to those of online SPE-HPLC-ICP-MS ($r^2 = 0.99$).

Other separation and preconcentration methods for the analysis of soils, plants or related materials, or those developed for other sample matrices that used soil or plant CRMs for validation, are summarised in Table 9.

4.4. Instrumental analysis

4.4.1. Atomic absorption spectrometry. Butcher¹¹⁰ (65 references) reviewed *recent developments in elemental analysis by ETAAS and ETMAS* including examples featuring plants and soil. Multi-element determination, analyte preconcentration, speciation analysis, and solid/slurry sampling were amongst the areas highlighted for further research.

Interest has continued in *the use of HR-CS-AAS for multielement analysis*. A HR-CS-ETAAS method was developed¹¹¹ and successfully applied for the determination of trace Pb in Antarctic grass, lichen and moss, simultaneously with the lithogenic elements Al and Fe, the concentrations of which are required to estimate environmental Pb enrichment. A matrix modifier ($1 \text{ g L}^{-1} \text{ Pb} + 0.6 \text{ g L}^{-1} \text{ Mg}(\text{NO}_3)_2$) and a compromise temperature programme ($T_{\text{pyrolysis}} 900 \text{ °C}$, $T_{\text{atomisation}} 2500 \text{ °C}$) avoided loss of the relatively volatile Pb whilst ensuring efficient atomisation of the more refractory Al. Combining spectral lines with different sensitivities and measuring at different points within each line extended the linear working range to four orders of magnitude for Al. Relative bias for analysis of four plant CRMs was in the range 8 to 12%, -4 to $+5\%$ and -5 to $+7\%$, for Al, Fe and Pb, respectively. Other authors coupled¹¹² CVG with HR-CS-QTAAS for the sequential determination of As, Bi, Hg and Sb, followed by Se and Te, in a variety of samples, including sediment and soil. It was necessary to measure the analytes in two groups because different pre-reduction conditions were required for each. Flushing the reaction cell (and

atomiser) with Ar (6 L min^{-1} for 20–30 s) before introducing NaBH_4 eliminated spectral interference from residual NO_x and O_2 .

Direct solid sampling avoids lengthy sample digestion procedures in atomic spectrometry. A method for mercury speciation analysis by thermal release ETAAS achieved¹¹³ baseline resolution of CH_3HgCl , HgCl_2 , HgS and HgSO_4 with a sample furnace heating rate of 15 °C min^{-1} and an argon gas flow rate of 0.2 L min^{-1} . Calibrants were prepared by diluting the Hg species mixture with aluminium oxide and the method was applied to samples from a mine tailings dump. Spike recoveries from the tailings samples were 98–104% for $\text{CH}_3\text{-HgCl}$, HgCl_2 and HgS , but only 88% for HgSO_4 . A Cd–Hg analyser incorporated¹¹⁴ a programmable ETV unit, a dual catalytic pyrolysis furnace (to remove interferences such as soil organic matter), a gold amalgamator (for trapping of Hg), and miniature AAS spectrometer detectors for each analyte (based on FAAS for Cd and CVAAS for Hg). Addition of a matrix modifier ($7 + 3 \text{ m/m NaCl} + \text{citric acid}$) improved sensitivity for Cd, allowing sub ng g^{-1} LODs to be achieved for both analytes. Results could be obtained for a 100 mg soil sample in as little as 3 min.

An alternative to analysing dry solid samples is to present them to the instrument in the form of a slurry. A *slurry sample introduction system for ETAAS* was described¹¹⁵ that incorporated closed, cooled vessels to prevent evaporation and contamination. Automated stirring stabilised suspensions without the need for addition of surfactant. Results for the determination of Cd in RM BAM-U110 (contaminated soil) suspended in water were stable over a 12 h run involving 184 measurements, with relative measurement errors of -8 to $+23\%$.

4.4.2. Atomic fluorescence spectrometry. An *electrolytic HG-AFS method for the determination of Se* used¹¹⁶ a nickel foam electrode to enhance the yield of H_2Se from Se^{IV} . Combination with an UAE and pre-reduction of the electrochemically inert Se^{VI} to Se^{IV} allowed speciation analysis of mushrooms to be carried out. The LOD was $0.13 \mu\text{g L}^{-1}$ with spike recoveries in the range 95–99% for Se^{IV} and 96–98% for Se^{VI} .

4.4.3. Inductively coupled plasma mass spectrometry. Several *sp-ICP-MS review articles* were published during the Update period. Nakazato and Hirata²⁶ (160 references) provided an accessible overview of the principles and capabilities of the technique, whilst Goodman *et al.*²⁷ (103 references) focussed more on its history and contribution to improved understanding of environmental processes. Both sets of authors highlighted the large volumes of data produced during analysis and the need to handle these appropriately. Fortunately, data treatment tools in *sp-ICP-MS* and single cell ICP-MS were the topic of another review¹¹⁷ (45 references) that covered advances in text-based and graphic user interfaces, as well as machine learning. Although mainly directed towards clinical analysis, a mini-review¹¹⁸ (113 references) of sample preparation methods for the measurement of NPs in biological fluids and tissues by *sp-ICP-MS* included some examples featuring the analyses of plants.

Other aspects of ICP-MS have been reviewed. Xu *et al.*¹¹⁹ (71 references) described advances in ICP-MS for detection of endogenous substances in single cells, including plant tissues



(in Chinese with an abstract in English). Laser ablation ICP-MS was amongst the techniques included in an overview (112 references) by Vats *et al.*¹²⁰ of MS approaches for elemental or molecular imaging of plants, microbes and food. Duan *et al.*¹²¹ provided a very comprehensive review (402 references) of stable Zn isotopes as tracers in environmental geochemistry, including information on sample processing and $\delta^{66}\text{Zn}$ measurement by MC-ICP-MS. Quantitative and isotopic determination of REEs and radionuclides by ICP-MS/MS was the topic of Zhu *et al.*¹²² (170 references) who covered articles published since the first commercial instrument was released in 2012. A key conclusion was that for measurement of actinides, it would be useful to extend the mass range of the second quadrupole to >300 AMU.

A PVG-ICP-MS method¹²³ for the simultaneous determination of Br, Cl and I used a novel spray chamber with internal UV light source for irradiation of sample aerosol and addition of 1% (v/v) acetic acid + 20 mg L⁻¹ Cu²⁺. Signal enhancements relative to conventional pneumatic nebulisation were 40-fold, 3-fold, and 30-fold, for Br, Cl and I, respectively, with corresponding LODs of 6.3 pg mL⁻¹, 4.2 ng mL⁻¹ and 1.9 pg mL⁻¹. Results for the analysis of NIST SRM 1515 (apple leaves) agreed with certified or information values (Student's *t*-test at 95% confidence).

Coupling LC with ICP-MS for speciation analysis continues to be of interest. Methods for the analysis of seaweed based on IC-ICP-MS were reported that could separate and quantify As species¹²⁴ (AB, DMA, As^{III}, MMA and As^V) and Pb species¹²⁵ (Pb²⁺, trimethyl lead and triethyl lead). A dual HPLC-ICP-MS/ESI-MS procedure¹²⁶ in which the column effluent was split and directed towards the elemental and molecular mass spectrometers in parallel was developed and applied to study As detoxification mechanisms in seedlings grown in As-spiked hydroponic media. Arseno-thiols and As^{III}-phytochelatins were detected in roots of plants exposed to As^{III} and As^V, and arsenolipids in roots exposed to As^V. A method for Se speciation in rice¹²⁷ took a similar approach to a procedure for soil analysis described in our previous Update: samples were extracted (in this case with Pronase E enzyme); extracts were filtered; then soluble Se species in the filtrate were separated and quantified by HPLC-ICP-MS, whilst Se NPs trapped on the membrane were quantified separately.

A comparison of different standards for the determination of lanthanides in tea by LA-ICP-MS recommended^{128–129} Au as IS over ¹³C, ¹⁰³Rh, ¹¹⁵In or ²⁰⁵Tl. External calibrants prepared by drying different concentrations of a lanthanide solution onto filter papers gave better precision than those prepared by spiking and pelleting powdered leaves or cellulose powder, and LODs were lower (20 ng g⁻¹ for Ce, 75 ng g⁻¹ for La and 14 ng g⁻¹ for Nd). Results obtained for the three analytes in mint tea were not significantly different from those obtained by digestion and conventional ICP-MS analysis according to a *t*-test at 95% confidence. The other lanthanides were <LOQs and not reported.

The ability of MC-ICP-MS to perform accurate *stable isotope ratio measurement* provides valuable insight into the biogeochemical cycling of trace elements. However, sample

pretreatment procedures must be carefully optimised to remove interferences, maximise analyte recovery, and avoid isotopic fractionation. Advances for Cd isotopic analysis included AEC procedures¹²⁹ applicable to plants, rocks, seawater and soil samples that gave $\delta^{114}\text{Cd}$ values in agreement with previously published literature values for a suite of CRMs, and a dry ashing method¹³⁰ for analysis of materials with high organic matter content (LOI > 90%). In the latter method, samples were wrapped in a quartz microfibre filter membrane – which was later removed by HF digestion – to avoid losses in the muffle furnace. Results were not significantly different from those obtained with high-pressure bomb digestion (*t*-test, *p* = 0.98) for a suite of eight CRMs, including BCR-482 (lichen) and GSB-16 (spirulina). For Sb, a HG-MC-ICP-MS procedure¹³¹ that involved SSB and Cd doping gave $\delta^{123}\text{Sb}$ value ranges for geological and environmental CRMs of low analyte content – including four soils and one plant – that overlapped (within uncertainty) previously published values.

New optimised ICP-MS/MS approaches included the use¹³² of CH₄ as reaction gas to successfully overcome the numerous mass spectral interferences associated with the determination of S in soil and plant digests. The analyte was measured as CH₂SH⁺ ion clusters in mass-shift mode at *m/z* 47 and 49. An investigation¹³³ of multi-element analysis of the *Brassica* tumorous stem mustard, recommended cool plasma conditions (rf power 600 W) and 1.5 mL min⁻¹ NH₃ reaction gas for interference reduction in the determination of Al, Co, Cr, Cu, Fe, Mn, Mo, Ni, Pb, Sr and V, but hot plasma conditions (rf power 1600 W) and 0.3 mL min⁻¹ O₂ + 7.0 mL min⁻¹ H₂ in the determination of As, Cd, Hg, Se and Zn. The LODs for all elements were below 1 ng g⁻¹ except for that of Se (4.8 ng g⁻¹). Studies featuring the determination of actinides in soil by ICP-MS/MS included a comparison⁷⁶ of commercial NO (99.5% purity) and specially purified NO (<100 ppt H₂O) reaction gases. The latter was shown to give a three-fold improvement in sensitivity for Np and Pu, and also meant that higher gas flow rates could be used to eliminate U interference. Other researchers studied¹³⁴ actinide reactivity with CO₂, O₂, and O₂/He reaction gases that led to development of a method suitable for measurement of ²⁴¹Am/²⁴¹Pu ratios in the presence of complex sample matrices. Both nuclides were determined in mass shift mode, with Am detected as ²⁴¹Am¹⁶O⁺ at *m/z* 257 and Pu as ²⁴¹Pu¹⁶O₂⁺ at *m/z* 273, to avoid the analytes interfering with one another.

An interesting application of sp-ICP-MS provided the first direct evidence of the existence of naturally occurring Cd-based NPs in paddy soil. The extraction procedure,¹³⁵ which was optimised by adding CdS-NPs to a Cd-free soil, involved shaking of 0.5 g samples with 20 mL of 20 mM tetrasodium pyrophosphate at 300 rpm for 3 h. This gave better recoveries (71%) than UAE. When applied to soil from six paddy fields in Guangdong, China, 17–50% of the Cd content was found to be in the form of NPs.

A study¹³⁶ on the translocation of Se in plants used isotopically labelled ⁸²Se NPs to avoid the polyatomic ion interferences suffered by the more abundant ⁷⁸Se and ⁸⁰Se. This improved the sp-ICP-MS S/N approximately 11-fold and decreased the size



LOD from 90 to 40 nm. Following foliar application to *Oryza sativa* (rice plants) ^{82}Se NPs were taken up, but largely remained in the leaves, with little translocation to other parts of the plant. Such information is important for the optimisation of biofortification programmes to address Se deficiency, which affects roughly 1 billion people worldwide.

Feldmann *et al.*¹³⁷ advocated the use of ICP-MS in non-target screening analysis of environmental samples. They emphasised the technique's potential contribution in three areas: the identification of chemicals of emerging concern; the quantification of compounds for which no reference standards exist; and the revealing of 'hidden' compounds *i.e.*, those that would not be detected if only targeted analysis was applied.

A novel nanolitre spray chamber was developed¹³⁸ for use with microwave plasma torch MS that allowed the concurrent measurement of Cr, Cu, Ni, Pb, Zn and three phthalate plasticisers (based on their predominant $[\text{M} + \text{H}]^+$ molecular ions) in soil. Limits of detection of 0.16 to 0.57 $\mu\text{g L}^{-1}$ for the PTE and 0.02 and 0.05 $\mu\text{g L}^{-1}$ for the phthalates were achieved at a samples flow rate of just 5 $\mu\text{L min}^{-1}$, with recoveries from a spiked soil digest of 91–106% and 89–97%, respectively. A group of researchers first investigated¹³⁹ the determination of Sb by HG-MPT-MS, demonstrating the possibility of accurate isotope ratio measurement through optimisation of capillary and tube lens voltages to remove interference from ^{123}Te . They then attempted¹⁴⁰ the more challenging direct determination of hydride-forming elements in solid samples by MPT-MS. Soil samples were ground, sieved and pressed into tablets for analysis, and calibration was achieved with respect to matrix-matched standards (clean soil spiked with the analytes of interest). The approach showed promise – As, Bi, Pb and Sb were all visible in the mass spectrum of soil CRM GBW07405 – but further work is needed to achieve accurate quantitative analysis.

4.4.4. Laser-induced breakdown spectroscopy. Several *LIBS review articles* were relevant to the analysis of soils and plants. Ferriera *et al.*¹⁴¹ (193 references) discussed calibration strategies – univariate calibration, a wide variety of multivariate approaches, and calibration-free LIBS – and data fusion *i.e.* the combination of LIBS with other analytical techniques such as Raman, IR or XRF spectroscopy. Looking to the future, they anticipated that advanced data science tools, such as machine learning and deep learning algorithms, will continue to grow in importance due to their ability to extract useful information from complex LIBS spectra. Yao *et al.*¹⁴² (121 references) also focussed on data fusion. Three areas were covered: LIBS combined with elemental analysis (LA-ICP-MS, XRF and LIF); LIBS combined with molecular spectroscopy (Raman and NIR) and LIBS combined with hyperspectral imaging. Rizwan *et al.*¹⁴³ (244 references) provided a comprehensive overview of the fundamental principles of double-pulse LIBS before discussing a wide variety of applications including environmental and soil analysis. Finally, a tutorial review by Zhao *et al.*¹⁴⁴ (153 references) described recent advances in LIBS imaging. The focus was mainly on fundamental principles and applications in medicine, minerals and materials analysis, but the potential

utility of the approach to investigate trace element transport and distribution in plants and seeds was noted.

Efforts have continued to *enhance signal intensity* and thereby improve LODs in the LIBS analysis of soil. To this end, two groups of researchers mixed conductive additives with their samples. One¹⁴⁵ compared KCl, KBr, graphite, TiO_2 NPs and ZnO NPs. They found the greatest enhancement for Cd was obtained with addition of 25% graphite, giving LODs of 1.5 and 3.6 mg kg^{-1} for two different soils. The other¹⁴⁶ studied NaCl and graphite. Best performance (LOD 26.1 mg kg^{-1}) for the determination of Pb was obtained with addition of a mixture containing 10% NaCl + 20% graphite. An alternative approach¹⁴⁷ involved the simultaneous application of a magnetic field (110 mT) and an electrical field (12 V) to the area occupied by the sample plasma. This combined approach increased spectral intensity for Al approximately two-fold, and for Fe approximately three-fold. Other workers proposed¹⁴⁸ (in Chinese with an abstract in English) an electrochemical LIBS method in which Hg was accumulated by electrodeposition on a gold electrode surface for interrogation with the laser.

A LIBS method¹⁴⁹ for determination of Cr, Cu and Pb in soil extracts used Au@SiO_2 NPs deposited on a specially designed laser-etched zinc substrate to improve LODs to 0.32, 0.28 and 0.36 mg kg^{-1} , respectively. This work highlights *a fundamental issue hampering the wider adoption of LIBS in soil laboratories*, which is a lack of connectivity and knowledge sharing between the scientists developing the spectroscopic methods and experienced soil analysts. For example, Guo *et al.*¹⁴⁹ noted that “remarkably” different results were obtained for Pb and Cu using different extractants. The fact that different extractants will remove different amounts of trace elements from the same sample has been known in the soil science community for the better part of a century. They also reported having “developed the solid-liquid-solid transformation (SLST) method”. However, what they actually did was a conventional UAE in DPTA – a procedure that is commonly-used in soil laboratories for assessment of phytoavailability – and then dried an aliquot of their extract on a hotplate.

Confocal controlled LIBS was applied¹⁵⁰ for the first time to determine Cd in soil. Real-time autofocusing at each data-acquisition point improved ablation consistency *i.e.* reduced variability in ablation crater depth and diameter, relative to conventional LIBS, thereby improving spectral stability. The LOD decreased from 80 to 49 mg kg^{-1} . However, this is still some way above that required for routine environmental monitoring.

Single-shot LIBS for *rapid nutrient monitoring in hydroponically grown plants* was proposed.¹⁵¹ Quantification was not attempted, but it was shown that the signal obtained for Ca in lettuce leaf increased with Ca concentration in nutrient medium. The study also confirmed the uptake of Ag NPs from hydroponic solution into plants. Although much more work needs to be done, the prospect of using real-time LIBS data to adjust hydroponic nutrient composition and thereby optimise crop growth is worthy of further exploration.



Many LIBS articles were concerned principally with *advances in data processing and modelling* rather than sample pretreatment or spectroscopy. Notable examples featuring soil were a machine learning approach based on the SHapley Additive exPlanations algorithm for the prediction of soil C;¹⁵² a transfer learning approach (named TransLIBS) for the determination of total N;¹⁵³ a PCA-generalised spectrum-extreme learning machine model for quantification of major elements (Al, Ca, Fe, Mg, Si and Ti);¹⁵⁴ and a black slit-supported stand-off LIBS method combined with machine learning for measurement of available soil nutrients (B, Ca, Cu, Fe, K, Mg, Mn, N, P, S, Zn).¹⁵⁵ For plants, a multi-chemometrics approach allowed the determination of N in coco-peat;¹⁵⁶ a XGBoost transfer learning model based on rice husks improved Cd detection in rice grains;¹⁵⁷ and a Wasserstein generative adversarial network revealed differences in the distribution of Ca, Fe, K, Mg, Mn and Na in leaves of rice plants under chromium stress, relative to those in unstressed plants.¹⁵⁸

An extension of the above is *proximal analysis* in which LIBS measurements, either alone or in combination with results obtained by other analytical techniques, are processed to classify or predict some property of a sample, rather than to obtain analyte concentrations. Interesting examples included a handheld LIBS method¹⁵⁹ for prediction of soil organic carbon content and soil texture (proportions of sand, silt and clay); the integration of LIBS with convoluted neural networks¹⁶⁰ to identify the origins of soybeans from different regions in China; and a classification system¹⁶¹ based on LIBS and machine learning that was able to distinguish different types of plant leaves.

4.4.5. X-ray fluorescence spectrometry. *Reviews of XRF* included that of Vanhoof *et al.*¹⁶² (91 references) that covered advances in 3D imaging particularly those achieved by XRF spectrometry CT and confocal XRF spectrometry. In-house 2D XRF spectrometry instrumentation was covered, as were advances in high resolution imaging with SR-XRF. Applications of SR with XRF and XAS or micronutrient mapping and speciation in plants and seeds were reviewed by Ashe *et al.*¹⁶³ (123 references), as was SR- μ -CT, as a tool for visualisation of the internal microstructures and 3D morphologies of seeds in fine detail.

A *novel monochromatic excitation EDXRF system* combined with fundamental parameters algorithmic analysis improved¹⁶⁴ the detection of As and Pb in grain. Optimisation of the doubly curved crystal structure and the geometry layout resulted in improved sensitivity compared to that of existing EDXRF methods. The LODs of 0.02 mg kg⁻¹ (As) and 0.03 mg kg⁻¹ (Pb) were sufficiently low to detect these PTE at concentrations below food safety limits.

The *influence of soil matrix variability on accuracy* was considered in several studies. Wang *et al.*¹⁶⁵ determined that linear relationships were particularly poor ($r^2 < 0.2$) between concentrations of As, Cd, Cr, Cu, Hg, Ni, Pb and Zn, in grey fluvo-aquic, fluvo-aquic, purple and rice soils determined by ICP-MS and the net area of XRF characteristic peaks. Pearson's correlation analysis indicated that the most significant

parameters influencing accuracy were Fe, Mn, Si and organic matter contents. To compensate for errors arising from organic matter content, a correction was proposed¹⁶⁶ using the Compton scattering peak as the internal standard. Application of the correction to As and Pb determinations in 33 soil samples, with organic matter content ranging from 0–49.5%, led to a reduction in relative measurement errors from 0.25–9.05% to 0.22–3.87% for As and 2.77–46.2% to 0.05–3.94% for Pb.

Studies on the performance of *portable instrumentation and software* included that of Purwadi *et al.*¹⁶⁷ They compared the concentrations of a range of elements in plants obtained using three portable XRF instruments, and three different quantification methods. Instrument performance varied depending on factors including anode and filter type, element of interest and instrument settings. Quantification based on manufacturer's algorithms were found to overestimate elemental concentrations and resulted in highest deviation from results obtained by ICP-AES, while empirical calibration based on XRF *vs.* ICP-AES regression had closest mean concentration agreement between the two techniques but occasionally produced negative results. Independent GeoPIXE software based on fundamental parameters gave the most accurate results, reducing errors by up to 95% compared to the manufacturer's algorithms. Such variation in performance reinforces the need for due diligence when using pXRF spectrometry.

5. Analysis of geological materials

5.1. Review papers

Sensing and analysis technologies for deployment in *lunar exploration* have been extensively reviewed¹⁶⁸ (209 references) in a wide ranging work covering chemical, isotopic, and structural analyses, radiation, temperature, and vacuum sensing. The importance of instrument miniaturisation and integration was emphasized for effective *in situ* exploration and analysis. Developments in miniaturised integrated instruments were discussed featuring a wide range of techniques including LIBS and MS.

A review with 212 references studied¹⁶⁹ analytical techniques for nanomaterial–mineral associations. Testing at the bulk, micro-, and nanoscale were discussed, alongside use of automated search software and preparation methods such as focused ion beam, ultramicrotomy, and ion milling. Studies that investigated the role of nanomaterials in soil organic matter stability and pollutant interactions were then considered.

5.2. Reference materials and data quality

Reference materials have played a pivotal role in the evolution of geochemical analysis, with their applications broadening well beyond traditional geological studies. A *bibliometric survey of geochemical RMs and CRMs*¹⁷⁰ (32 references) derived from over 14 000 documents revealed temporal and thematic trends, showing the evolution from ore geology and petrogenesis to broader applications supported by ISO standards and





Table 10 New geological reference materials for isotope measurements

| Analytes | Matrix | Technique | RM name | Comments | References |
|--|-----------------------|--------------|----------------------------|--|------------|
| Ag, As, Au, Bi, Cd, Co, Cu, In, Mo, Ni, Pb, Pd, Pt, Rh, Sb, Se, Sn, Te, Zn | Synthetic pyrrhotite | LA-ICP-MS | Po-800–9 | High purity pyrrhotite (Fe/S molar ratio 0.92), reacted at 800 °C for 4 days. Eighteen trace elements added at 100 mg kg ⁻¹ . Ground, pressed and annealed at 600, 800 and 1000 °C for 9 and 28 days; optimal homogeneity at 800 °C, 9 days (RSD < 5% at 80 µm spot). Embedded in epoxy and polished with diamond paste | 329 |
| Al, Ca, Cr, Co, Fe, Ga, Mg, Mn, Na, Ni, Sc, Si, Ti, V, Y, Zn | Orthopyroxene | LA-ICP-MS | BL-1 | Homogeneity (µm–mm scale) confirmed by WD-XRF, EPMA and LA-ICP-MS. Bulk analyses (WD-XRF, ICP-OES, solution-ICP-MS) agree with <i>in situ</i> microanalyses. Ca, Cr, Mn, Na, Ni, Ti, V > 100 mg kg ⁻¹ | 330 |
| ⁴⁰ Ar/ ³⁹ Ar dating | Muscovite | MS | ZMT04 | Laser step-heating and single-grain laser fusion prior to MS. Homogeneity at single-grain level. Minimum sample mass: 1 mg. K–Ar recommended age = 1804 ± 21 Ma (2 SD). ⁴⁰ Ar/ ³⁹ Ar age: 1772.2 ± 2.7 Ma (2 SD) | 331 |
| B isotopes | Ca-amphibole | LA-MC-ICP-MS | PRG, FIN | PRG: B 6.75 ± 1.10 µg g ⁻¹ ; $\delta^{11}\text{B} = -16.58 \pm 0.06\text{‰}$. FIN: B 3.27 ± 0.68 µg g ⁻¹ ; $\delta^{11}\text{B} = -5.90 \pm 0.09\text{‰}$. Good isotopic homogeneity. BHVO-2 G as bracketing standard; reproducibility: PRG ± 2.86‰ (2 SD, N = 87), FIN ± 3.96‰ (2 SD, N = 70) | 332 |
| B isotopes | Tourmaline | LA-MC-ICP-MS | TOUR1, TOUR4, TOUR5, TOUR6 | Recommended $\delta^{11}\text{B}$ (2 SE): TOUR1 –11.26 ± 0.06‰; TOUR4 –13.31 ± 0.07‰; TOUR5 –8.88 ± 0.05‰; TOUR6 –8.57 ± 0.04‰ | 333 |
| B, multielemental determination | Tourmaline megacrysts | LA-MC-ICP-MS | MD-B66, IM-B232, BR-DG68 | MD-B66: $\delta^{11}\text{B} = -7.74 \pm 0.25\text{‰}$ (2 SD, N = 251)—primary homogeneous RM. IM-B232, BR-DG68: secondary RMs. Solution MC-ICP-MS: MD-B66–7.71 ± 0.32‰ (N = 12); IM-B232–13.17 ± 0.62‰ (N = 8); BR-DG68–13.85 ± 0.32‰ (N = 12). BR-DG68 homogeneous in major (Al, B, Ca, Fe, Li, Mg, Mn, Na, Si, Ti) and trace elements (Be, K, Sc, V, Co, Zn, Ga, Sr, Sn, Pr, Nd, Sm, Eu, Pb) | 334 |
| B & Sr isotopes | Natural Tourmaline | LA-MC-ICP-MS | HGL-3 | From Huanggangliang-Hanzhuermiao Sn-polymetallic belt. Homogeneous in B and Sr at 33 µm and 90 µm. B 36 830–43 700 µg g ⁻¹ ; Sr 216–260 µg g ⁻¹ ; Rb/Sr < 0.0013. $\delta^{11}\text{B} = -12.83 \pm 0.38\text{‰}$ (2 SD, n = 485); ⁸⁷ Sr/ ⁸⁶ Sr = 0.70835 ± 0.00019 (2 SD, n = 515). LA-MC-ICP-MS precision: 0.42‰ (B), 0.00019 (Sr). Agrees with TIMS | 335 |
| C isotopes | Basaltic glasses | SIMS | ETNA24, ETNA32, ETNA36 | CO ₂ by SHM-IRMS: 2300 ± 69; 3360 ± 180; 2026 ± 34 µg g ⁻¹ . $\delta^{13}\text{C}$ (SHM-IRMS): –14.3 ± 0.7; –12.1 ± 0.2; –10.2 ± 0.7‰. H ₂ O (TCEA-IRMS): 2.86 ± 0.06%, 1.02 ± 0.06%, 2.30 ± 0.06%. δD (TCEA-IRMS): –135.7 ± 0.9; –103.9 ± 0.9; –101.6 ± 0.9‰ | 223 |
| C isotopes | Silicate glasses | SIMS | 31 RMs | Glass series (MORB, basaltic, NBO; andesite–basalt). Homogeneous $\delta^{13}\text{C}$. IMF reproducibility ± 1.0‰ for CO ₂ down to 1800 ± 200 ppm. Internal precision ± 1.1‰ (min. ± 0.3‰) at 10–20 µm. CO ₂ : 380–12 000 ppm. $\delta^{13}\text{C}$: –28.1 ± 0.2 to –1.1 ± 0.2‰ (± 1 SD). SIMS $\delta^{13}\text{C}$ (IMF-corrected) agrees with EA-IRMS | 336 |



Table 10 (Contd.)

| Analytes | Matrix | Technique | RM name | Comments | References |
|--|---------------------------|-------------------|---|---|------------|
| Cu, Fe & S isotopes | Chalcopyrite | LA-MC-ICP-MS | IGGCcp-1 | Homogeneity validated through EPMA. SN-MC-ICP-MS data: $\delta^{65}\text{Cu}$ 0.43 \pm 0.05‰ (2S, $N = 30$); $\delta^{56}\text{Fe}_{\text{IRMM-014}}$ and $\delta^{57}\text{Fe}_{\text{IRMM-014}}$: 0.24 \pm 0.04‰ (2S, $N = 18$) and -0.36 ± 0.09 ‰ (2S, $N = 18$), respectively $\delta^{34}\text{S}_{\text{VCDT}}$ (EA-IRMS): -0.28 ± 0.60 ‰ (2S, $N = 10$) | 337 |
| Fe isotopes | Hematite | LA-MC-ICP-MS | Sintered hematite | $\delta^{56}\text{Fe}_{\text{IRMM-014}}$ for the initial powder, sintered pellets, and unsintered pellets: 0.45 \pm 0.04‰ (2SD, $N = 20$), 0.44 \pm 0.04‰ (2SD, $N = 21$), and 0.45 \pm 0.02‰ (2SD, $n = 3$), respectively | 172 |
| Fe isotopes | Magnetite | fs-LA-MC-ICP-MS | HGS-9, FP-200, SX-72, CBL-500, SJS-20 | Isotopic homogeneity. $\delta^{56}\text{Fe}$ precision: ± 0.05 – 0.06 ‰ (2 SD, SN-MC-ICP-MS); ± 0.08 – 0.14 ‰ (2 SD, LA-MC-ICP-MS) | 338 |
| Fe oxidation state | Garnet | EPMA flank method | And1902, Grs1928, Mels01, Ald1906, Ald1915, Ald1917, Ald1905, Ald1907, Ald1925, Ald1926 | Ten natural RMs: three andradite-grossular, seven almandine-pyrope-grossular (Ald). Fe L_{α} /Fe L_{β} intensity ratio correlates with oxidation state. And1902 & Ald1906 suitable as primary flank standards. And-Grs: Fe ³⁺ /ΣFe = 0.89 \pm 0.03 to 1.00 \pm 0.03; Ald: 0.01 \pm 0.02 to 0.03 \pm 0.01. Agrees with Mössbauer. Uncertainty: ± 1 wt% (Fe ²⁺); ± 0.05 (Fe ³⁺ /ΣFe) | 339 |
| Fe & Mg isotopes | Olivine | LA-MC-ICP-MS | CUG-OL-Ar | Sintered olivine RM (solid-phase sintering + ultrafine powder). $\delta^{56}\text{Fe}_{\text{IRMM-014}} = 0.00 \pm 0.06$ ‰ (2 SD, $N = 350$); $\delta^{25}\text{Mg}_{\text{SC}} = 0.00 \pm 0.05$ ‰ (2 SD, $N = 350$). Excellent homogeneity and analytical performance. Long-term precision < 0.11 ‰ (Fe); < 0.08 ‰ (Mg) | 340 |
| Cl, CO ₂ , F, H ₂ O, S | Basaltic silicate glasses | SIMS | ND70 series | RMs range: H ₂ O 0–6% w/w; CO ₂ 0–1.6% w/w; S, Cl, F 0–1% w/w. Characterised via ERDA, NRA, EA, FTIR, SIMS, EPMA. Good inter-technique agreement except CO ₂ . SIMS reproducibility poor at high H ₂ O due to ¹² C ionisation effects | 178 |
| Hf isotopes | Cassiterite | LA-MC-ICP-MS | CST01, CST02, CST03 | Homogeneity at 30 μm . $^{176}\text{Hf}/^{177}\text{Hf}$: 0.282262 \pm 0.000022 (2 SD, $N = 200$); 0.282273 \pm 0.000031 (2 SD, $N = 348$); 0.282276 \pm 0.000049 (2 SD, $N = 517$) | 171 |
| Li isotopes | Lepidolite | LA-MC-ICP-MS | NWU-LPD | Recommended reference $\delta^7\text{Li}$ value: 8.70 \pm 0.28‰ (2SD, $N = 5$) | 341 |
| Lu-Hf dating | Garnet | LA-ICP-MS/MS | GWA-1, GWA-2 | GWA-1 (almandine-grossular), Lu $\approx 7.0 \mu\text{g g}^{-1}$; GWA-2 (almandine-spessartine), Lu $\approx 8.5 \mu\text{g g}^{-1}$ | 342 |
| O isotopes | Calcite | SIMS | WS-1 | Crystallisation ages: 1267.0 \pm 3.0 Ma with initial $^{176}\text{Hf}/^{177}\text{Hf}$; 0.281415 \pm 0.000012 (GWA-1), and 934.7 \pm 1.4 Ma with $^{176}\text{Hf}/^{177}\text{Hf}$: 0.281386 \pm 0.000013 (GWA-2) | 343 |
| O isotopes | Xenotime | SIMS | PX xenotime | SIMS spot-to-spot reproducibility < 0.21 ‰ (1 SD). $\delta^{18}\text{O}_{\text{VPDB}}$ (gas-source IRMS): -16.52 ± 0.13 ‰ (1 SD). Mean SIMS: -16.44 ± 0.25 ‰ (1 SD, $N = 225$). Useful for inorganic aragonites and low-Mg calcites; beware matrix effects in high-Mg organic skeletal calcites | 344 |
| O isotopes | Xenotime | SIMS | PX xenotime | From Zagi Mountain (Pakistan). Homogeneous by SIMS. $\delta^{18}\text{O}$ (LF-IRMS): 6.25 \pm 0.13‰ (2 SD, $N = 6$) | 344 |



Table 10 (Contd.)

| Analytes | Matrix | Technique | RM name | Comments | References |
|---|---------------------------------|------------------------------------|-------------------------|--|------------|
| O isotopes | Spodumene | SIMS | Tri-1, Kun-A-1, MG-1 | Bulk $\delta^{18}\text{O}_{\text{VSMOW}}$ by LF-IRMS: $11.29 \pm 0.04\text{‰}$; $9.12 \pm 0.10\text{‰}$; $15.13 \pm 0.08\text{‰}$ (2 SE). Homogeneous at nanogram scale by SIMS (2 SD $< 0.24\text{‰}$; $N > 20$). No crystal-orientation effects on SIMS mass bias | 345 |
| | Latosol | MC-ICP-MS | GSS-7 | Mean $\delta^{87}\text{Rb}_{\text{SRM984}}$: $-0.08 \pm 0.02\text{‰}$ (2 SD, $N = 9$). Accuracy tested by mixing with NIST SRM 984: $\delta^{87}\text{Rb}_{\text{SRM984}} = 0.02 \pm 0.02\text{‰}$ (2 SD, $N = 3$); similar composition mix: $0.03 \pm 0.02\text{‰}$ (2 SD, $N = 3$) | 346 |
| Rb isotopes | Pegmatite | ID-TIMS/MC-ICP-MS | OU-9 | Rb = $2494 \pm 22 \mu\text{g g}^{-1}$; Sr = $36.05 \pm 0.25 \mu\text{g g}^{-1}$. $^{87}\text{Rb}/^{86}\text{Sr} = 832.4 \pm 5.2$; $^{87}\text{Sr}/^{86}\text{Sr} = 32.60 \pm 0.19$. Not fully homogeneous in Rb and Sr mass fractions, but Rb–Sr systematics at 0.2 g scale agree with reference isochron. Isochron age ≈ 2650 Ma; initial $^{87}\text{Sr}/^{86}\text{Sr} \approx 1.2$ | 347 |
| Rb–Sr dating | Muscovite | LA-MC-ICP-MS/MS | ZMT04 | Rb–Sr isochron age: 1778.8 ± 4.9 Ma (2SD, $N = 180$), consistent with $^{40}\text{Ar}/^{39}\text{Ar}$ 1772.2 \pm 2.7 Ma (2SD). Inter-session RSD: 0.69% | 348 |
| ^{137}Ba , ^{140}Ce , ^{133}Cs , ^{163}Dy , ^{166}Er , ^{151}Eu , ^{157}Gd , $^{177,178}\text{Hf}$, ^{165}Ho , ^{139}La , ^{175}Lu , ^{93}Nb , ^{146}Nd , ^{141}Pr , ^{85}Rb , ^{149}Sm , ^{88}Sr , ^{181}Ta , ^{159}Tb , ^{232}Th , ^{169}Tm , ^{238}U , ^{89}Y , ^{172}Yb , $^{90,91}\text{Zr}$ | Black shales | ICP-HR-MS | SChS-1A SI-g-1A | Contents of 25 elements after fusion with lithium metaborate; mean error $< 5\%$ | 349 |
| | Barite | LA-ICP-MS | 1-YS, 294-YS | Natural pure barite. SEM: Main composition BaO, SO ₃ , SrO (minor Na ₂ O, Al ₂ O ₃). BSE: homogeneity in S, Ba, Sr. $\delta^{34}\text{S}$ reproducibility $< \pm 0.45\text{‰}$ (2SD, 1-YS); $< \pm 0.41\text{‰}$ (2SD, 294-YS). $\delta^{34}\text{S}$ recommended (four labs): 1 YS $13.37 \pm 0.42\text{‰}$; 294-YS $14.38 \pm 0.44\text{‰}$ (2 SD) | 350 |
| S isotopes | Barite | SIMS | NJU-Ba-1, NJU-Ba-2 | No internal zoning. $\delta^{34}\text{S}_{\text{V-CDT}}$ (GS-IRMS): $6.18 \pm 0.34\text{‰}$ (2SD, $N = 17$); $14.16 \pm 0.26\text{‰}$ (2 SD, $N = 9$). SIMS homogeneity inter-/intra-unit: variation 0.36‰ (2SD, $N = 328$); 0.45‰ (2SD, $N = 343$) | 351 |
| S isotopes | Pyrite | LA-MS-ICP-MS, LG-SIMS and NanoSIMS | M332, MK617 | S homogeneity confirmed <i>in situ</i> and matches IRMS. $\delta^{34}\text{S}$ (IRMS): $M332$ $24.96 \pm 0.22\text{‰}$ (2SD, $N = 10$); $MK617$ $-4.43 \pm 0.21\text{‰}$ (2SD, $N = 12$). $\delta^{33}\text{S}$ (SIMS): $MK617$ $12.89 \pm 0.60\text{‰}$ (2SD, $N = 104$); $M332$ $-2.23 \pm 0.35\text{‰}$ (2SD, $N = 120$) | 352 |
| S isotopes | Pyrite, gypsum and arsenopyrite | LA-MC-ICP-MS | NWU-Py, NWU-Gy, NWU-Apy | Ultra-fine powder hot-press sintering: high homogeneity. $\delta^{34}\text{S}$: NWU-Py $3.48 \pm 0.26\text{‰}$ (2SD, $N = 787$); NWU-Gy $18.19 \pm 0.32\text{‰}$ (2SD, $N = 290$); NWU-Apy $-0.19 \pm 0.32\text{‰}$ (2SD, $N = 383$). Agrees with IRMS | 173 |
| S isotopes | Sphalerite | LA-ICP-MS | Sph-LD | Mean $\delta^{34}\text{S}$: $+17.11 \pm 0.20\text{‰}$ (2SD, $N = 560$), comparable with IRMS ($+17.22 \pm 0.20\text{‰}$, 2SD, $N = 10$). Elemental homogeneity $< 10\%$ at 26–40 μm | 174 |
| Sr isotopes | Apatite | LA-MC-ICP-MS | SL-7, SM139-1 | EPMA/LA-ICP-MS: Cl $1.80\text{--}2.46 \text{ wt\%}$; Sr $> 3752 \mu\text{g g}^{-1}$; low Rb/Sr. $^{87}\text{Sr}/^{86}\text{Sr}$: 0.70521 ± 0.00016 (2SD, $N = 120$) and 0.70509 ± 0.00015 (2SD, $N = 126$). Agrees with solution TIMS/MC-ICP-MS | 353 |



Table 10 (Contd.)

| Analytes | Matrix | Technique | RM name | Comments | References |
|--|----------------------------|--------------------------|---|---|------------|
| Sr isotopes | Calcite | LA-MC-ICP-MS | HZZ-2, TARIM | Homogeneous natural calcite RMs (μ -XRF, EPMA, LA-ICP-MS). Rb/Sr $< 1 \times 10^{-5}$; Sr $\sim 1100 \mu\text{g g}^{-1}$ (HZZ-2), $\sim 620 \mu\text{g g}^{-1}$ (TARIM). TIMS $^{87}\text{Sr}/^{86}\text{Sr}$: 0.70941 ± 0.00001 (2SD, $N = 8$); 0.71042 ± 0.00001 (2SD, $N = 7$). Consistent with LA-MC-ICP-MS | 354 |
| U–Pb dating, Hf isotope measurement | Baddeleyite | LA-MC-ICP-MS | SK 10–3 | Transparent grains (150–300 μm , aspect ratio 2 : 1–3 : 1), inclusion-free, uniform U–Pb ages. LA-ICP-MS weighted mean $^{206}\text{Pb}/^{238}\text{U}$: 31.59 ± 0.11 Ma (MSWD = 0.7, $N = 197$). $^{176}\text{Hf}/^{177}\text{Hf}$: 0.282741 ± 59 (2SD, $N = 188$), ID-TIMS $^{206}\text{Pb}/^{238}\text{U}$: $31.592 \pm 0.020/0.022/0.040$ Ma (2SD, $N = 7$). MC-ICP-MS $^{176}\text{Hf}/^{177}\text{Hf}$: 0.282742 ± 8 (2SD) | 355 |
| U–Pb dating | Andradite-rich garnet | ID-TIMS, SIMS, LA-ICP-MS | MKWB, DGS, Stanley | Three natural andradite RMs: MKWB (secondary U–Pb & trace RM), DGS (very homogeneous U–Pb age), Stanley (secondary RM). Multi-lab and multi-technique homogeneity. ID-TIMS $^{206}\text{Pb}/^{238}\text{U}$: MKWB 264.9 ± 5.8 Ma (2SD, $N = 6$, MSWD = 3.4); DGS 139.42 ± 0.36 Ma (2SD, $N = 5$, MSWD = 1.9); Stanley 23.28 ± 0.38 Ma (2SD, $N = 3$, MSWD = 1.9) | 356 |
| U–Pb dating | Columbite-tantalite | LA-ICP-MS | OXF | U, Th, Pb concentrations: 428 ± 156 ppm; 6.3 ± 2.5 ppm; 20.0 ± 10.0 ppm (2SD). CA-ID-TIMS $^{206}\text{Pb}/^{238}\text{U}$: 262.85 ± 0.64 Ma (2SD, $N = 6$). LA-ICP-MS weighted mean (4 labs): 262.83 ± 0.29 Ma (2SD, $N = 358$) | 357 |
| U–Pb dating | Titanomagnetite | LA–SF–ICP-MS | HG79c | RM age: 259.2 ± 2.8 Ma, consistent with Concordia-intercept $^{206}\text{Pb}/^{238}\text{U}$ using cassiterite AY-4 as external standard. | 358 |
| U–Pb dating | Grossular-Andradite Garnet | LA-ICP-MS | And ₉₉ , And ₈₇ , And ₆₇ | Accurate also using zircon 91500 and garnet PL-57 calibration IC-TIMS single-crystal age precision $\sim 0.1\%$. RMs: And ₉₉ (Jumbo andradite) 110.34 ± 0.13 Ma ($N = 7$); And ₈₇ (Triptop andradite) 209.58 ± 0.28 Ma ($N = 6$). Primary RM And ₆₀ (Willshoro-Lewis) age 1024.7 ± 9.5 Ma (2 SD, $N = 6$) | 359 |
| U–Pb/Lu–Hf dating | Xenotime | LA-ICP-MS/MS | Xtm-NHBS | ID-TIMS $^{206}\text{Pb}/^{238}\text{U}$: 498.7 ± 0.4 Ma (2SD, $N = 5$). LA-Q/SF-ICP-MS spots: Lu–Hf weighted means: 502.1 ± 3.6 Ma (2SD, $N = 39$); 494.6 ± 3.8 Ma (2SD, $N = 40$) | 360 |
| U–Th–Pb, (U–Th)/He dating, Hf–O isotopes | Zircon | LA-ICP-ToF-MS | Zircon-S513 | U, Th, Pb, Hf: 924 ± 64.6 ; 89.6 ± 3.92 ; 119 ± 5.20 ; $8259 \pm 244 \mu\text{g g}^{-1}$ (2SD). ID-TIMS Th-corrected ratios: $^{206}\text{Pb}/^{238}\text{U}$ 0.090955 ± 0.000019 ; $^{207}\text{Pb}/^{235}\text{U}$ 0.73873 ± 0.00023 ; $^{207}\text{Pb}/^{206}\text{Pb}$ 0.058934 ± 0.000008 (2SD, $N = 8$). CA-ID-TIMS Th-corrected $^{206}\text{Pb}/^{238}\text{U}$ age: 561.18 ± 0.63 Ma ($N = 8$). LA-ICP-MS/SIMS $^{206}\text{Pb}/^{238}\text{U}$ ages: $560.8 \pm 5.8/10.2$ Ma (2SD, $N = 260$); $562.4 \pm 7.2/13.4$ Ma (2SD, $N = 198$). LA $^{208}\text{Pb}/^{232}\text{Th}$: $561.3 \pm 3.3/11.7$ Ma (2SD, $N = 86$). (U–Th)/He age: 420.3 ± 7.6 Ma (2SD, $N = 37$). $^{176}\text{Hf}/^{177}\text{Hf}$ MC-ICP-MS: 0.281606 ± 0.000010 (2SD, $N = 12$); LA: 0.281605 ± 0.000008 (2SD, $N = 310$). $\delta^{18}\text{O}$ (LF): $11.71 \pm 0.11\%$ (2SD, $N = 5$). Homogeneity: $\leq 8\%$ (1 σ) in major/minor elements, 0.12% (2SD) in U–Pb, 1.8% (2SD) in (U–Th)/He, 0.0036% (2SD) in Hf, 0.11% (2SD) in O | 361 |



Table 10 (Contd.)

| Analytes | Matrix | Technique | RM name | Comments | References |
|-------------------------------|----------|----------------|----------|---|------------|
| U–Th–Pb dating | Allanite | LA-ICP-MS | AMK, ASP | ²⁰⁶ Pb with respect to total ²⁰⁶ Pb content below 0.8 and 5.5%, AMK, U and Th concentrations: $140 \pm 41.9 \mu\text{g g}^{-1}$ (1SD) and $306 \pm 145 \mu\text{g g}^{-1}$ (1SD), respectively. ASP, U and Th concentrations: $261 \pm 143 \mu\text{g g}^{-1}$ (1SD) and $130 \pm 102 \mu\text{g g}^{-1}$ (1SD), respectively. Weighted mean ²⁰⁷ Pb/ ²⁰⁶ Pb age: $1533.6 \pm 1.9 \text{ Ma}$ (2SD, $N = 6$) for AMK and weighted mean ²⁰⁶ Pb/ ²³⁸ U age: $335.86 \pm 0.52 \text{ Ma}$ (2SD, $N = 8$) for ASP (ID-TIMS). AMK proposed as primary RM for LA-ICP-MS U–Th–Pb dating and ASP as secondary RM | 179 |
| U–Th–Pb dating, O–Nd isotopes | Monazite | LA-ICP-MS SIMS | M6 | ThO ₂ = $10.7 \pm 1.1\%$ (2SD); Th/U = 28.4 ± 3.3 (2SD). Age reproducible and homogeneous at $30 \mu\text{m}$ (LA-ICP-MS & SIMS), concordant with ID-TIMS. ID-TIMS ²⁰⁷ Pb/ ²³⁵ U $485.7 \pm 2.3 \text{ Ma}$ (2SD, $N = 7$). Sm–Nd (LA-MC-ICP-MS): ¹⁴³ Nd/ ¹⁴⁴ Nd = 0.511829 ± 0.000045 (2 SD); ¹⁴⁷ Sm/ ¹⁴⁴ Nd = 0.2302 ± 0.0139 (2SD). $\delta^{18}\text{O}$ (SIMS): $7.70 \pm 0.41\%$ (2SD) | 362 |

consolidated by the geoanalytical community. While RMs remain largely used in petrogenesis, CRMs are now more evenly distributed across earth, environmental, and chemical sciences. Current themes include high-resolution and microanalytical techniques, unconventional isotope systems, and the development of more realistic CRMs, with increasing attention to biogeochemical hazards, REEs, and radionuclides.

Recreating geological processes, but on a shorter time scale aided the development of new RMs. Three HfO₂-doped cassiterite RMs were prepared¹⁷¹ by *sintering* milled powders ($d_{50} = 6.3 \mu\text{m}$) under elevated temperature and pressure while maintaining the ¹⁷⁶Hf/¹⁷⁷Hf ratio in the dopant powder. A rapid method for hematite RM production for Fe isotope analysis *via* LA-MC-ICP-MS involved¹⁷² compaction of Fe₂O₃ NPs, previously blended with polyvinyl alcohol, followed by sintering at 1000 °C for 2 h to yield isotopically homogeneous pellets. This RM was stable, could be easily polished, and the procedure could be extended to the preparation of other RMs. Development of pyrite based RMs,¹⁷³ sphalerite RMs¹⁷⁴ and rutile RMs¹⁷⁵ also used a sintering process. Further information on these materials can be found in Table 10.

Production of new RMs with required elemental or isotopic compositions involved a *doping* process. Synthesizing B₄C with natural and enriched isotopic ratios *via* carbothermic reduction or direct reaction, followed by pelletizing, vacuum heating ($\sim 1800 \text{ }^{\circ}\text{C}$), and grinding provided RMs with ¹⁰B/¹¹B ratios between 0.247–2.03 for in-house measurements by particle induced γ -ray emission (PIGE).¹⁷⁶ Production of a columbite matrix standard for LA-ICP-MS applications¹⁷⁷ involving doping with a multielement standard solution, and extended milling (90% of particles $\leq 1.74 \mu\text{m}$), which enabled pressed pellet calibrants with smooth, glass-like surfaces to be produced. Preparation of RMs doped with volatile species (Cl, CO₂, F, H₂O, S) was however more challenging. Basaltic glass RMs were produced¹⁷⁸ by melting crushed material at 1350 °C, quenching, and re-melting to degas, followed by addition of volatile species by pressurised diffusion at 1–1.5 GPa and 1225–1325 °C for 2 h in a sealed system.

The lack of suitable RMs with low non-radiogenic Pb content has hindered U–Th–Pb dating in allanite. Two new matrix-matched allanite RMs with reduced common Pb, titled AMK and ASP, see Table 10, were proposed¹⁷⁹ as alternatives to the widely used Tara allanite standard, removing the need for common Pb correction, improving robustness and simplifying dating procedures.

The suitability of the widely used *NIST SRM 610 and 612* (trace elements in glass) for microanalysis by LA-ICP-MS was evaluated.¹⁸⁰ Calibration uncertainty was shown to be a major limitation for high-precision microscale measurements, demonstrating a need for new RMs with certified microscale homogeneity for their trace element content.

Interest in obtaining *novel elemental composition and isotopic data* for established geological reference materials (RMs) remains high. This updated information is crucial for validating current analytical methodologies and is reported in Tables 11 and 12 respectively.

Table 11 New data for existing geological reference materials

| Analytes | Matrix | Technique | Comments | References |
|-------------|---|--------------|---|------------|
| Ba isotopes | Sediments | MC-ICP-MS | Sediments NGRCC: GSD-1, GSD-2, GSD-3, GSD-6, GSD-7, GSD-7a, GSD-8, GSD-11 and GSD-14. $\delta^{138/134}\text{Ba}$: from $0.03 \pm 0.05\text{‰}$ to $-0.08 \pm 0.06\text{‰}$ (2SD, $n = 5$) | 363 |
| Cd isotopes | Chondrite | MC-ICP-MS | L3.2 ordinary chondrite GRO 95504. $\text{Cd} = 20.7 \pm 0.5 \text{ ng g}^{-1}$; $\delta^{114}\text{Cd} = 7.55 \pm 0.08\text{‰}$ | 129 |
| Ce isotopes | Igneous rocks, metamorphic rocks, sediments, soils | MC-ICP-MS | 33 USGS, GSJ, IGGE RMs. Precision $\pm 0.04\text{‰}$ (2SD). $\delta^{142/140}\text{Ce}$: igneous rocks (-0.036 to 0.062‰), soils (-0.015 to 0.029‰), sediments/nodules (-0.005 to 0.141‰) | 98 |
| Fe oxide | Igneous, sedimentary, metamorphic rocks | XRF | GeoPT samples (35). FeO from 0.07 to 11.88% | 364 |
| Ga isotopes | Granodiorite, gabbro, granite, clayey limestone, jasperoid, soil, shale, sediment | MC-ICP-MS | GSJ JG-1 (granodiorite): $\delta^{71}\text{Ga} = -1.36 \pm 0.06\text{‰}$ (2SD, $n = 6$); USGS JGb-2 (gabbro): $\delta^{71}\text{Ga} = -1.48 \pm 0.01\text{‰}$ (2SD, $n = 4$); IGGE GSR-1 (granite): $\delta^{71}\text{Ga} = -1.31 \pm 0.05\text{‰}$ (2SD, $n = 2$); IGGE GSR-6 (clayey limestone): $\delta^{71}\text{Ga} = -1.41 \pm 0.04\text{‰}$ (2SD, $n = 4$); USGS GXR-1 (jasperoid): $\delta^{71}\text{Ga} = -1.39 \pm 0.07\text{‰}$ (2SD, $n = 6$); USGS GSS-11 (soil): $\delta^{71}\text{Ga} = -1.32 \pm 0.04\text{‰}$ (2SD, $n = 2$); IGGE GSS-12 (soil): $\delta^{71}\text{Ga} = -1.40 \pm 0.04\text{‰}$ (2SD, $n = 4$); NIST 2711a (soil): $\delta^{71}\text{Ga} = -1.31 \pm 0.06\text{‰}$ (2SD, $n = 2$); USGS SGR-1b (shale): $\delta^{71}\text{Ga} = -1.40 \pm 0.02\text{‰}$ (2SD, $n = 2$); USGS GSD-12 (sediment): $\delta^{71}\text{Ga} = -1.37 \pm 0.05\text{‰}$ (2SD, $n = 4$) | 365 |
| Hg isotopes | Coal, Cu–Ag sulfide ore, Au–Te sulfide ore | MC-ICP-MS | A dual-stage tube furnace system containing a Mn catalyst tube was used to pretreat mineral ore samples NCRM RMs: GBW-111108v, coal: $\delta^{202}\text{Hg} = -1.02 \pm 0.05\text{‰}$ and $\Delta^{199}\text{Hg} = -0.31 \pm 0.03\text{‰}$ (1SD, $n = 6$); GSO-3, Cu–Ag sulfide ore: $\delta^{202}\text{Hg} = 0.25 \pm 0.04\text{‰}$ y $\Delta^{199}\text{Hg} = -0.12 \pm 0.02\text{‰}$ (1SD, $N = 6$); GBW 07859, Au–Te sulfide ore: $\delta^{202}\text{Hg} = -0.97 \pm 0.06\text{‰}$ and $\Delta^{199}\text{Hg} = 0.08 \pm 0.03\text{‰}$ (1SD, $n = 6$) | 183 |
| I/Ca ratios | Carbonate, coral | LA-ICP-MS | JCp-1 (coral) more homogeneous and reproducible than MACS-3. Suitable as calibration RM for I/Ca profiling. I distribution much more homogeneous for JCp-1 (1.03%) than for MACS-3 (30.0%). Better repeatability for Mg, Sr, Ba and U for the former RM. JCp-1 more suitable as calibration standard for high resolution ($<100 \mu\text{m}$) I/Ca profiling and multielemental analysis of corals using LA-ICP-MS | 366 |
| Ir levels | Mafic intrusive rocks, felsic rocks, sedimentary rocks, metamorphic rock | MC-ICP-MS | 11 USGS RMs. Ir contents: mafic intrusive rocks (DTS-2 and W-2), felsic rocks (GSP-2, QLO-1, GSR-1, JG-2 and JR-2), sedimentary rocks (SBC-1, Nod-A-1 and COQ-1) and metamorphic rock (SDC-1) (in pg g^{-1}): 2983 ± 455 ; 383 ± 26 ; 18 ± 3 ; 6 ± 2 ; $4 \pm 0.5 \pm 0$; 9 ± 3 ; 105 ± 30 ; 8661 ± 980 ; 22 ± 6 ; 22 ± 6 | 367 |
| K isotopes | Igneous, sedimentary, metamorphic rocks | MC-ICP-MS | $\delta^{41}\text{K}$ for 18 NRC RMs geological RMs with K_2O mass fractions ranging from 0.15 to 7.5% . $\delta^{41}\text{K}$ values ranging from -1.15‰ (GBW07122, GSR 15, amphibolite) to 0.28‰ (GBW07120, GSR 13, limestone), with an intermediate measurement precision of 0.05‰ (2SD). New data provided for six RMs | 368 |
| Li isotopes | Sediments, soils, rocks | MC-ICP-MS/MS | Data provided for NIST SRMs 1646a (estuarine sediment), 2706 (New Jersey soil), 2711a (Montana II soil), 2780a (hard rock mine waste), and 4350b (Columbia River sediment) $\delta^7\text{Li}$: $3.79 \pm 0.63\text{‰}$; $2.50 \pm 0.53\text{‰}$; $-0.28 \pm 0.23\text{‰}$; $5.10 \pm 0.15\text{‰}$; $0.94 \pm 0.06\text{‰}$ (2S, $N = 3$), respectively | 369 |
| Mg isotopes | Gabbro, diabase, basalt, andesite, granite, rhyolite, schist, mudstone, quartz sandstone, limestone, clayey limestone, dolomite, fluvial sediments, manganese nodules | MC-ICP-MS | USGS, GSJ and NRC CRM RMs. Felsic and mafic igneous rocks: gabbro (JGb-2); diabase (DNC-1a); basalt (JB-1b, JB-2); andesite (GSR-2, JA-2); syenite (STM-2); granite (GSR-1, JG-1); rhyolite (GSR-11, RGM-2, JR-1, JR-3). Metamorphic rocks: micaceous schist (SDC-1). Sedimentary rocks: mudstone (GSR-5); quartz sandstone (GSR-4); limestone (GSR-13); clayey limestone (GSR-6); dolomite (JDO-1, GBW07127a). Sediments: soil (GSS-4); fluvial sediments from different regions (GSD-1, GSD-3, GSD-9, GSD-21, | 370 |



Table 11 (Contd.)

| Analytes | Matrix | Technique | Comments | References |
|----------------------|--|--------------|--|------------|
| Mg isotopes | Carbonates | MC-ICP-MS | GSD-23). Manganese nodules (NOD-A-1, NOD-P-1). Minerals: soapstone (GBW03130); kaolinite (GBW03121a); wollastonite (GBW03123) NCRM RMs magnesite GBW07865, dolomites GBW07114, GBW(E)070159, GBW07136, limestone GBW07108, gypsum GBW03109a, limestones GBW07120 and GBW07214a, and RMs IAEA-B-7 and carbonatite IAEA-CO-8. Mg content: 295 $\mu\text{g g}^{-1}$; Ca to Mg mass ratios around 1300 g g^{-1} | 371 |
| Mo isotopes | Granite, andesite, olivine basalt, syenite, trachyte, granodiorite, rhyolite, amphibolite, soils | MC-ICP-MS | NCRM RMs analysed: granite GBW07103, andesite GBW07104, olivine basalt GBW07105, syenite GBW07109, trachyte GBW07110, granodiorite GBW07111, rhyolite GBW07113, amphibolite GBW07122, soils GBW07401a, GBW07405a and GBW07407 $\delta^{98/95}\text{Mo}$: igneous -0.54‰ to $+0.01\text{‰}$; amphibolite $-0.04 \pm 0.08\text{‰}$; soils -0.28‰ to $+0.22\text{‰}$. Mo from 0.07 to 3.92 $\mu\text{g g}^{-1}$, RSD 0.05–5.30% | 372 |
| Ni, Cu & Zn isotopes | Basalt, andesite, granodiorite, Mn nodule, sulfide ore, sediments, soil, mud | MC-ICP-MS | $\delta^{60}\text{Ni}_{\text{NIST986}}$, $\delta^{65}\text{Cu}_{\text{NIST976}}$ and $\delta^{66}\text{Zn}_{\text{JMC-Lyon}}$ provided for 36 NIST, IRMM, NRC, USGS and GSJ geological RMs | 99 |
| S isotopes | Marine sediments | CR-IR-MS | USGS and GSJ RMs: Marine sediments (JMS-1, JMS-2), marine shales (SBC-1, SCo-2), stream sediments (JSd-3, JSd-4) and lacustrine sediment (JLk-1). New data set including abundances of total S, HCl-insoluble S, and their isotopic ratios ($\delta^{34}\text{S}_{\text{Total S}}$, $\delta^{34}\text{S}_{\text{HCl-insoluble S}}$, and $\delta^{34}\text{S}_{\text{Cr reducible S}}$) for the RMs | 373 |
| Sb isotopes | Basalt, andesite, amphibolite, quartz sandstone | HG-MC-ICP-MS | $^{113/111}\text{Cd}$ element doping and SSB improved precision (2SD) from 0.08‰ – 0.12‰ to 0.02‰ – 0.08‰ . $\delta^{123}\text{Sb}$: USGS BCR-2 ($0.28 \pm 0.09\text{‰}$, 2SD, $n = 9$), USGS AGV-2 ($0.23 \pm 0.11\text{‰}$, 2SD, $N = 6$), NCRM GSR-15 ($0.36 \pm 0.09\text{‰}$, 2SD, $N = 6$), and NCRM GSR-4 ($0.49 \pm 0.06\text{‰}$, 2SD, $N = 9$) | 131 |
| Sn isotopes | Basalt, dunite, quartz latite, rhyolite, shale, syenite, dolomite, peridotite, komatiite, serpentine | MC-ICP-MS | $\delta^{122/118}\text{Sn}_{(\text{NIST SRM}) (3161a)}$ for USGS BIR-1a, Icelandic basalt; USGS DTS-2b, dunite; USGS QLO-1a, quartz latite; USGS RGM-2, rhyolite; USGS SGR-1b, shale; USGS STM-2, syenite; BAS ECRM 782-1, dolomite; CPRM BRP-1, basalt; GSJ JP-1, peridotite; IAG OKUM, komatiite; ANRT UB-N, serpentine | 374 |
| Ti isotopes | Ilmenite, titanite | LA-MC-ICP-MS | $\delta^{49}\text{Ti}_{\text{OL-Ti}}$ with solution nebulization MC-ICP-MS: ilmenite GER16: $-0.24 \pm 0.05\text{‰}$ (2SD, $n = 6$); titanite MAD12: $0.26 \pm 0.06\text{‰}$ (2SD, $n = 4$) LA-MC-ICP-MS data in good agreement Ilmenite GER16: ns-LA-MC-ICP-MS (wet plasma) $\delta^{49}\text{Ti} = -0.22 \pm 0.17\text{‰}$ (2SD, $n = 28$); ilmenite GER16: fs-LA-MC-ICP-MS (wet plasma) $\delta^{49}\text{Ti} = -0.24 \pm 0.13\text{‰}$ (2SD, $n = 42$) Titanite MAD12: ns-LA-MC-ICP-MS (wet plasma) $\delta^{49}\text{Ti} = 0.25 \pm 0.14\text{‰}$ (2SD, $n = 21$); titanite MAD12: fs-LA-MC-ICP-MS (wet plasma) $\delta^{49}\text{Ti} = 0.23 \pm 0.16\text{‰}$ (2SD, $n = 45$) | 375 |
| Tl isotopes | Stream sediment, soil, shale, granodiorite, granite, nepheline syenite, trachyte, rhyolite | MC-ICP-MS | $^{205}\text{Tl}/^{203}\text{Tl}$ ratios determined in ten geological RMs: SGR-1b (from the USGS), and GBW07302, GBW07303a, GBW07401a, GBW03104, GBW07103, GBW07109, GBW07110, GBW07111 and GBW07113 (from China). Dry ash digestion causes heavy isotope enrichment vs. acid digestion. $\epsilon^{205}\text{Tl}$ validated with USGS RMs | 376 |

5.3. Sample preparation, dissolution and chemical separation

Various *sample preparation methods* (166 references) were reviewed in the Handbook of Rock and Mineral Analysis,¹⁸¹

including open- and closed-vessel decomposition using HF, HNO₃, HClO₄, H₂SO₄, with or without microwave assistance, as well as alternatives such as NH₂HF₂ and NH₄F. Molten salt fusions (LiBO₂, Li₂B₄O₇, Na₂CO₃) and sequential extractions are also reviewed, while preconcentration and separation





Table 12 Methods developed for the determination of isotope ratios in geological material

| Element | Matrix | Sample preparation | Technique | Comment | References |
|--------------------------------------|---|---|---|---|------------|
| Ag | Ultramafic, mafic to felsic igneous rocks, sediments, soils | NH ₄ HF ₂ digestion + ammonia coprecipitation | ID-ICP-MS | Polyatomic interferences (Zr, Nb, Y) corrected, ID compensated Ag loss. LOQ 1.83 ng g ⁻¹ ; RSD 0.4–7% | 377 |
| Al isotopes | Carbonaceous chondrites | Thin polished sections | SIMS | Six ²⁶ Al/ ²⁷ Al ₀ values near canonical (5.2 × 10 ⁻⁵); inclusions formed during main thermal event | 378 |
| As, Tl | Sphalerite and associated phases | Comparison with RMs (realgar, orpiment, mimetite, lorandite, synthetic Tl silicate) | XANES | Derivative analysis distinguished As from As ³⁺ ; Tl spectra confirmed monovalent Tl. Demonstrated oxidation state discrimination in ore systems | 379 |
| B isotopes | Carbonates | Direct LA | LA-ICP-MC-MS | Ca-rich matrices and ionized Ar increased background at <i>m/z</i> ≈ 10, complicating ^δ ¹¹ B accuracy. Differences in ablation rates between samples and standards introduced isotopic bias | 380 |
| B isotopes | Silicate, peridotite, coral, calcite, aragonite, basalt glass | Mounting/pellets | LA-MC-ICP-MS/MS | Precision <1‰ (≥40 mV). ^δ ¹¹ B of 14 RMs within uncertainty; design minimized Ar, Ca interferences | 381 |
| B isotopes, major and minor elements | Silicates | Milling, pelleting, epoxy mount | LA-ICP-MS | 51 elements + ^δ ¹¹ B; new ^δ ¹¹ B for GSJ JP-1, BHVO-1, BCR-1, JG-1a. Precision ±0.3–0.4‰; elements within ±20% of GeoReM | 382 |
| C isotopes | Diamond | Mounted in Sn alloy | LA-MC-ICP-MS | <i>In situ</i> ^δ ¹³ C precision <0.2‰ (S/N ratio > 4). Accuracy validated vs. NanoSIMS/LA-IRMS. Mass fractionation 19.4‰ between natural/synthetic | 383 |
| C isotopes | Carbonates | <i>In situ</i> analysis at 90 μm spatial resolution | LA-ICP-MC-MS | Doubly charged Mg ²⁺ ions cause isobaric interference on ^δ ¹³ C measurements. Optimized He/Ar ratios and N ₂ addition (4–6 mL min ⁻¹) enhanced signal intensity and minimised Mg ²⁺ formation. Iterative mass bias correction yielded accurate ^δ ¹³ C values | 384 |
| Ca isotopes | Coral, dolomite, and limestone | Digestion with HNO ₃ /HCl = 3 : 1 v/v at 95 °C for 60 min | ICP-MS/MS | Ozone was proposed for Ca isotope analysis, overcoming the ⁴⁰ Ar interference <i>via</i> CaO ₃ ⁺ and ArO ⁺ generation | 385 |
| Ca isotopes | Calcite, dolomite | Direct ablation | LA-MC-ICP-MS | High-Sr carbonates; iterative correction improved accuracy. ^δ ⁴⁴ / ⁴² Ca: 0.10–0.19‰, ^δ ⁴³ / ⁴² Ca: 0.09–0.12‰ (2SD) | 386 |
| Ba, Ca, Ce, Nd, Sr | Manganese nodules, andesite, basalt, granodiorite, carbonate, simulated lunar soils | Digestion + multi-column separation | TIMS (Ca, Sr and Nd); MC-ICP-MS (Ba and Ce) | USGS analysed RMs: basalt (BHVO-2), manganese nodule powder (NOD-A-1), andesite (AGV-2), granite (GSP-2), and carbonate rock (COQ-1). Simulated lunar soil samples (CUG-1A and CUG-1B). Accurate simultaneous separation/measurement from 1–2 mg. High recovery (>99.5%), blanks <0.1%. Simultaneous separation and accurate measurement of Ca, Sr, Ba, Ce, and Nd isotopes from 1–2 mg. High recovery (>99.5%), low procedural blanks (<0.1%). First Sr, Ba isotope data for NOD-A-1, and those of Ca, Sr, Ba, Ce, and Nd from the simulated lunar soils CUG-1A and CUG-1B | 387 |



Table 12 (Contd.)

| Element | Matrix | Sample preparation | Technique | Comment | References |
|----------------------|--|---|-----------------|---|------------|
| Cd isotopes | Basalt, soil, shale, manganese nodules | Acid digestion + anion exchange | MC-ICP-MS | By measuring ^{106}Cd , ^{110}Cd , ^{111}Cd , and ^{113}Cd , the ^{114}Cd isotope was calculated, circumventing ^{114}Sn interference. Analysis of four geochemical RMs verified $\delta^{114/110}\text{Cd}$ values consistent with literature. Novel ^{106}Cd – ^{111}Cd double spike avoids Sn interference and simplifies separation | 388 |
| Eu isotopes | Basalt, sienite | HF/HNO ₃ digestion + two-step purification | MC-ICP-MS | Nd internal normalization improved stability and reproducibility of Eu isotope measurements long-term external precision of $\delta^{153/151}\text{Eu}$ at 0.04‰ (2SD) | 389 |
| Fe isotopes | Biotite, hornblende, pyroxene, olivine | Polished thin sections | fs-LA-MC-ICP-MS | Intermediate precision of 0.17‰ (2SD) for $\delta^{56}\text{Fe}$ over 3 years and consistency with previous data. Uncertainties for glass and olivine < 0.15‰. Spatial resolution was below 30 μm | 390 |
| Fe and Mg isotopes | Basalt, andesite, serpentine, granite, dolomite, coral | HF/HNO ₃ digestion + single-column separation | MC-ICP-MS | Geological RMs: USGS Basalt, USGS BHVO-2, BCR-2 and GSJ JB-1; andesite, USGS AGV-2; serpentine, ANRT UB-N; granite, USGS G-2 and GA; dolomite, NMJ JDo-1; and coral, GSJ JCP-1. Low sample sizes, <10 ng. Fe and Mg recoveries > 98% with removal of matrix elements Al, Ti, Na, K, Ca. The full purification procedure requires 1 day | 391 |
| Fe and Zn isotopes | Andesites, basalts, granodiorites | HF/HNO ₃ digestion + AG1-X8 purification | MC-ICP-MS | $\delta^{56}\text{Fe}$ and $\delta^{66}\text{Mg}$ values consistent with literature Use of a combined approach of element doping and standard-sample bracketing. RMs: USGS BCR-2, BHVO-2, AGV-2 and GSP-2, and GSJ JA-1, JA-2, JB-1b, JB-2, JG-1 and JG-2. Recoveries > 99.5%. Long-term analytical precision: $\pm 0.05\%$ for $\delta^{56}\text{Fe}$ and $\pm 0.03\%$ for $\delta^{66}\text{Zn}$. New Fe isotope data had been previously reported for JG-1. For JG-2, Fe isotope values higher than previously published data | 392 |
| Ge isotopes | Basalts, meteorites | Digestion, two-steps ionic exchange separation | MC-ICP-MS | Double-spike approach; HG introduction beneficial for low Ge | 393 |
| Ar, He, Ne, isotopes | Extraterrestrial materials (ilmenite and olivine) | Co-implantation of noble gases simulating solar wind irradiation | LIMAS | Enabled nanoscale noble gas profiling. Achieved low LODs, reproducible isotopic ratios, and 5–31% (1SD) RSF reproducibility | 394 |
| Hf and Nd isotopes | Basalt, andesite, serpentine | Hot plate digestion + three-steps ionic chromatography purification | MC-ICP-MS | High sensitivity (<10 ng). Apex omega desolvation gave low oxides (<0.05%) and interference removal (Ce, Sm) | 395 |
| K isotopes | Granite, basalt | HF/HNO ₃ digestion + AG50W-X12 resin | MC-ICP-MS/MS | Interferences ($^{40}\text{ArH}^+$) corrected with H ₂ . CRC. $\delta^{41}\text{K}$ for USGS BCR-1, basalt = $-0.37 \pm 0.12\%$ (2 SD) and for CRPG GA, granite = $-0.46 \pm 0.07\%$ (2 SD). Data in agreement with previously published work | 396 |
| Lu–Hf dating | Allanite | Epoxy mounts | LA-ICP-MS | Nine allanite samples from different rock types (e.g., granite, pegmatite). Ages 2650–100 Ma; calibration with NIST SRM 610 + LE2808. Precision <5% | 397 |



Table 12 (Contd.)

| Element | Matrix | Sample preparation | Technique | Comment | References |
|---------------|---|---|-----------|---|------------|
| Multi-element | Sedimentary rocks | Calibrated using stoichiometric materials; compared three scanners (medical CT, HECTOR μ CT, CoreTOM μ CT) | DECT | Determined Z_{eff} and ρ_{e} assessed X-ray energy, resolution, and calibration effects. Highlighted lack of universal protocol for geoscientific DECT | 398 |
| O isotopes | Quartz grains from river sediments and turbidites | Individual quartz grains (~ 200) isolated from Himalayan catchments and Bengal Fan sediments | LG-SIMS | Used $\delta^{18}\text{O}$ signatures to discriminate magmatic, metamorphic, and sedimentary sources. $\delta^{18}\text{O}$ values ranged 5–25‰; overlap ($\sim 11\%$) between Trans- and Lesser Himalaya but geological context enabled distinction. Complements detrital zircon provenance analysis | 399 |
| O isotopes | Quartz grains in river sediments | Drying and sieving. Subsequent quartz preconcentration with Na-polytungstate and dissolution with H_2SiF_6 and HCl. Pressing and polishing and cleaning with ethanol and Au coating | LG-SIMS | $\delta^{18}\text{O}$ signature ranged from 5‰ for Trans-Himalayan batholiths to 25‰ for the Tethys Himalayan zone | 399 |
| Os isotopes | Peridotite, chromitite, ultrabasic rocks | Sb fire assay + distillation | MC-ICP-MS | Large sample amounts (>20 g) enabled analysis of low-Os samples ($<1 \mu\text{g kg}^{-1}$). Validated vs. six IGGE RMs (WPR-1, GPT-5, GPT-6, GPT-3, GBW07102 and GPT-4) | 400 |
| Rb isotopes | Peridotite, komatiite, ultramafic rock | Digestion + ion exchange | MC-ICP-MS | Aridus III + Ni cones reduced requirements (~ 20 ng Rb). Precision $<0.05\%$ SSB with internal Zr normalization provided improved intermediate precision, though SSB was adequate for accuracy | 346 |
| Re isotopes | Basalt, diabase, andesite | Digestion + TEVA resin purification | MC-ICP-MS | Purification blank (<0.2 pg), Re yield $93.2 \pm 2.4\%$, 2SD , $N = 5$). $\delta^{187}\text{Re}_{\text{SRM3143}}$ precision 0.048% (1 ng g^{-1}). Consistent $\delta^{187}\text{Re}$ values for multiple RMs | 401 |
| Re isotopes | Basalts, marine mud, shales | Heating + digestion + AG1-X8 purification | MC-ICP-MS | Applied to USGS RMs: BCR-2, BIR-1, BHVO-2, basalts, SDO-1, SBC-1, SGR-1, shales with $\sim 0.5\text{--}75 \text{ ng g}^{-1}$ for Re. Re recovery = $99.6 \pm 6.7\%$, 2SD , $N = 10$; $\delta^{187}\text{Re} = -0.49 \pm 0.04\%$, 2SD , $N = 10$. Procedural blank for solid materials: $8 \pm 3 \text{ pg}$ (2SD , $N = 7$). Re isotope reported for the first time for SBC-1 (shale), $\delta^{187}\text{Re}$: $-0.45 \pm 0.06\%$ (2SD , $N = 4$) and SGR-1 (shale), $\delta^{187}\text{Re}$: $-0.27 \pm 0.10\%$ (2SD , $N = 5$). Variation in $\delta^{187}\text{Re}$ for schists: $\sim 0.35\%$ | 402 |
| Si isotopes | Basalt, peridotite, diatomite | NaOH fusion + AG50W-X12 purification | MC-ICP-MS | Double-spiked. $\delta^{30}\text{Si}/\text{Si}$ precision $\pm 0.03\%$; $\delta^{30}\text{Si}_{\text{NBS289}}$ for USGS RM BHVO-2 ($-0.276 \pm 0.011\%$, 2SD , $N = 94$), USGS RM BIR-1 ($-0.321 \pm 0.025\%$, 2SD , $N = 27$), GSJ RM JP-1 ($-0.273 \pm 0.030\%$, 2SD , $N = 19$) and diatomite ($1.244 \pm 0.025\%$, 2SD , $N = 20$) | 403 |
| Sn isotopes | Basalts, zinc ore, granite and soil | HNO_3 -HCl digestion + two-stage chromatography | MC-ICP-MS | Neoma less affected by isobaric interferences than the Neptune. Sn recoveries $85 \pm 5\%$, double spiking. RMs: Granodiorites (USGS GSP-2), basalts (USGS BCR-2, USGS BHVO-2, AISTJB-3), granite | 404 |



Table 12 (Contd.)

| Element | Matrix | Sample preparation | Technique | Comment | References |
|------------------|---|---------------------------------------|-------------------------------|---|------------|
| Sn isotopes | Basalt, andesite, granite, sediment, soil | Acid digestion + AG1-X8 + AG50W-X12 | MC-ICP-MS | (IAG OU-3), zinc ore (AIST JZn-1), soil (NIST SRM2711a), $\delta^{124/116}\text{Sn}_{\text{SRM3161a}}$ reported for the first time: $0.6 \pm 0.1\text{‰}$ (2SD, $N = 2$); $0.8 \pm 0.08\text{‰}$ (2SD, $N = 4$); $-0.87 \pm 0.07\text{‰}$ (2SD, $N = 2$); and $-0.12 \pm 0.08\text{‰}$ (2SD, $N = 3$), for the RMs: OU-3, JB-3, JZn-1 and NIST SRM 2711a, respectively | 405 |
| | | | | Interferents caused by Ag, Zn, Mo, Cd and Sb eliminated. Procedural blanks: $0.54 \pm 0.21\text{ ng}$ ($N = 3$), recovery: 95–102%, ($N = 32$); External precision ($\delta^{120}\text{Sn}$) = $0.02\text{--}0.04\text{‰}$ ($N = 55$). New $\delta^{117}\text{Sn}$, $\delta^{119}\text{Sn}$, $\delta^{120}\text{Sn}$ and $\delta^{122}\text{Sn}$ values for seven RMs: USGS BCR-2, USGS BHVO-2, USGS AGV-2, GSJ JG-2, GRPG AC-E, NRCC PACS-2 and ICGE GSS 7 | |
| Sr isotopes | Standard glasses | — | LA/solution MC-ICP-MS/MS | Precision (RSD) of <i>in situ</i> $^{87}\text{Sr}/^{86}\text{Sr}$ and $^{87}\text{Rb}/^{86}\text{Sr}$ isotope ratios (NIST SRM 610, BCR-2G, BHVO-2G, and OJY-1) = $0.016\text{‰}\text{--}0.036\text{‰}$ | 348 |
| Sr isotopes | Apatite | Four grains per sample, LA | LA- ICP-MS | <i>In situ</i> $^{87}\text{Sr}/^{86}\text{Sr}$ precision 0.45‰ (2SD) at $13\text{ }\mu\text{m}$ scale | 406 |
| Ti isotopes | Zircon RMs | | LA-ICP-MS/MS | NH_3 used to remove $^{48}\text{Ca}^+$ and $^{96}\text{Zr}^{2+}$ interferences on $^{48}\text{Ti}^+$. Analytical precisions <10%. Use of O_2 proved unsuitable due to $^{48}\text{Ca}^{16}\text{O}$ formation | 407 |
| U–Pb dating | Columbite | Epoxy mounts | LA-MC-ICP-MS | Resolution $10\text{ }\mu\text{m}$ (improved vs. $>20\text{ }\mu\text{m}$). $^{206}\text{Pb}/^{238}\text{U}$ ages correlated with $\text{Ta}/(\text{Nb} + \text{Ta})$ ratio | 408 |
| (U–Th)/He dating | Vesuvianite | Fragmentation, encapsulation | Laser He stripping-MS, ICP-MS | First vesuvianite (U–Th)/He dating. Ages consistent with U–Pb. Seven natural samples analysed: five alkaline rocks from China, a calcic grossular Al garnet (Russia) and metapelites (Mexico). Determined weighted mean ages: China M6635, $225.0 \pm 4.0\text{ Ma}$; M784, $223.0 \pm 4.8\text{ Ma}$; M1377 : $216.8 \pm 4.0\text{ Ma}$. $\pm 4.7\text{ Ma}$; M6608, $89.2 \pm 2.8\text{ Ma}$; M1439, $165.1 \pm 3.7\text{ Ma}$; Russia, Wilui, $266.7 \pm 6.6\text{ Ma}$; Mexico, Bufa, $32.3 \pm 0.6\text{ Ma}$ | 409 |
| Zn isotopes | Granodiorite, andesite, diabase, basalt, manganese nodules, granite | Precipitation + AG1-X8 chromatography | MC-ICP-MS | USGS GSP-2 (granodiorite), USGS AGV-2 (andesite), USGS W-2 (diabase), USGS BCR-2 (basalt), USGS BHVO-2 (basalt), USGS NOD-A-1 (manganese nodule), NCRM CRMs GBW07103 GSR-1 (granite), GBW07104 GSR-2 (andesite), and GBW07105 GSR3 (basalt). $\delta^{66}\text{Zn}$ for 9 RMs consistent with literature. $\delta^{66}\text{Zn}_{\text{MC-Lyon}} = 0.01\text{‰}\text{--}0.09\text{‰}$ (2SD). Zn recovery around 98% | 410 |
| Zn isotopes | Basalt, andesite, manganese nodules, granodiorite | AG1-X8 resin purification | MC-ICP-MS | Zn recoveries $\sim 98\%$. $\delta^{66/64}\text{Zn}_{\text{MC-Lyon}} = -1.43 \pm 0.04\text{‰}$ (2SD, $N = 362$) for NIST SRM 3168a, $0.29 \pm 0.04\text{‰}$ (2SD, $N = 61$) for IRMM 3702 and $0.29 \pm 0.04\text{‰}$ (2SD, $N = 61$) for AA-ETH-Zn. Long-term external reproducibility: $\pm 0.04\text{‰}$ (2SD) | 411 |
| Zr isotopes | Basalt | DGA resin single-pass chromatography | MC-ICP-MS | Results for eight RMs consistent with literature. Long-term reproducibility $< \pm 0.048\text{‰}$ for $\delta^{94}\text{Zr}$ | 412 |

Table 13 Sample preparation methods for the analysis of geological materials

| Analytes | Matrix | Technique | Sample preparation method | References |
|------------------------|---|-----------|---|------------|
| Ru, Os, Pd, Rh, Ir, Pt | Geological RMs | ID-ICP-MS | NaOH–Na ₂ O ₂ fusion; HNO ₃ acidification; K ₂ S ₂ O ₈ oxidation; HF/HCl dissolution; Te co-precipitation | 413 |
| Re, PGE | Meteorites | LA-ICP-MS | Comparison of carius tube and high-pressure ashing (HPA) dissolution; cation exchange column for on-line separation | 414 |
| Pd, Rh, Ir, Pt | Ore samples (PGE-bearing) | LA-ICP-MS | Sb fire assay preconcentration; compared to Pb-, NiS-, and Bi-based fire assays | 415 |
| Cd | Meteorites and soils | MC-ICP-MS | Digestion; AG MP-1M resin column in HCl; microcolumn purification | 129 |
| Nd, Sm | Chondrite | TIMS | Sequential ion-exchange (AG1-X8, TRU-Spec, DGA resins) | 416 |
| Sn | Siliceous rocks | MC-ICP-MS | Double-spike method; rock dissolution; organic matter removal; two-stage ion-exchange | 374 |
| REE (heavy REE focus) | Barite-bearing minerals | ICP-MS | Triethanolamine extraction; ammonia precipitation; anion exchange chromatography (717 resin) | 417 |
| Zr ^{IV} | Digested soils and rocks | ICP-AOES | Micelle extraction using eriochrome cyanine R and CTAB; cloud point extraction with Triton X-114; EtOH:HNO ₃ dissolution | 323 |
| Hg | Carbonates (corals, speleothems, carbonate rocks) | MC-ICP-MS | Digestion–reduction–purge–trapping protocol | 418 |

procedures are detailed in Part 2 of the Handbook. Additional preparation methods are summarised in Table 13.

An automated double-layer quartz pyrohydrolysis tube equipped with a liquid nitrogen cold trap was employed¹⁸² for the *quantitative recovery of volatile halogen compounds* from geological materials. The use of V₂O₅ promoted matrix decomposition and halogen volatilisation. After cold trapping, halogens were quantified by IC (Cl, F) and ICP-MS (Br, I) with MDLs of: 1.2 ng g^{−1} (Br), 0.40 µg g^{−1} (Cl), 0.25 µg g^{−1} (F), and 0.32 ng g^{−1} (I), for a 0.7 g sample. For the USGS RM BHVO-2 (Hawaiian volcano observatory basalt), Br Cl, and F results agreed with reported consensus values. However, iodine recoveries were significantly higher than the compiled reported values obtained with similar techniques, but agreed with those obtained using radiochemical NAA, demonstrating the efficacy of the extraction procedure.

Use of a novel dual-stage combustion-based system that incorporated an MnO₂ catalyst improved¹⁸³ *mercury isotope determination* in ores by effectively releasing Hg⁰ and eliminating tellurium by promoting the formation of non-volatile MnTeO₃. Unlike existing methods, which failed to remove tellurium, the new system improved Hg recovery (100.5 ± 3.8%, 1SD, N = 15) and reduced interferences during isotopic analysis of magmatic and hydrothermal sulfide ores by MC-ICP-MS.

Accurate *quantification of amorphous inorganic phases* in soils remains difficult with powder XRD. A comparative study¹⁸⁴ tested two sample preparation methods using synthetic mixtures that were also analysed by XRF. In the conventional method, quartz–calcite–feldspar–clay mixtures were spiked with

corundum (30% w/w) as IS and ground in ethanol, and the amorphicity was determined relative to the IS. In the alternative spray-drying method, aqueous suspensions with polyvinyl alcohol and 1-octanol produced fluid granules that could be analysed without sample rotation because samples were now more homogeneous. For mixtures with a >10% (w/w) amorphous content, both methods were accurate to <10%, the spray-drying method achieved better precision and eliminated orientation effects due to presence of clays.

5.4. Instrumental analysis

5.4.1. Laser-induced breakdown spectroscopy. LIBS has been extensively reviewed¹⁸⁵ (149 references) providing an overview of fundamentals, instrumentation, and geochemical applications, with a particular emphasis on the analysis of silicate rocks and the combination of LIBS with LA-ICP-MS. Sample preparation, matrix effects, signal processing, and chemometrics were discussed, along with elemental, quantitative, isotope, and 2D/3D compositional analyses. A tutorial review¹⁴⁴ (158 references) focused on LIBS imaging, addressing operational principles, resolution enhancement, and integration with complementary methods for biomedicine, minerals, industry, and materials. A review of tandem approaches¹⁴² (121 references) that combine LIBS with LA-ICP-MS, XRF, LIF, Raman, NIR, and hyperspectral imaging (HI), emphasised the importance of data fusion and the improvement in spatial and molecular characterisation that was now possible. Two separate reviews, one on the evolution of instrumentation¹⁸⁶ (246 references) from laboratory systems to portable analysers and the



other on recent developments in rock detection¹⁸⁷ (121 references) highlighted benchtop, compact, remote, and hybrid systems, used alongside machine learning (ML), for enhanced classification and quantification. The development of double-pulse LIBS (DP-LIBS) was reviewed¹⁴³ (247 references) with regards to configurations, signal enhancement, and plasma properties. Applications from metallurgical to environmental and archaeological studies were tabulated. A review¹⁸⁸ (255 references) of LIBS in extraterrestrial applications focused on calibration and transfer learning, TL, and the use of hyphenated methods such as LIBS-Raman, MS-LIBS, and FTIR-LIBS. Critical aspects and emerging trends were reviewed¹⁴¹ (200 references), including calibration, data fusion, and ML, leading to enhanced robustness and better analytical performance. These reviews showed that LIBS is versatile, integrates with complementary methods and is of growing importance in advanced geochemical analysis.

Matrix effects continue to challenge LIBS quantification. The influence of moisture was investigated¹⁸⁹ by evaluating spectral changes as rock samples were dried. It was determined that higher humidity attenuated spectral signals and their duration but without significantly affecting the plasma electron density or ionisation temperature. For U quantification in minerals, a modified spectral (internal) standardisation method utilised¹⁹⁰ correlations with a matrix element, typically silicon, in combination with a dominant-factor PLS regression model to improve the analytical signal RSD from 23% to 9% and improved r^2 from 0.91 to 0.99.

An innovative direction for overcoming matrix effects is the measurement¹⁹¹ of the acoustic emissions from laser-induced plasmas as a diagnostic signal using microphones. It was shown that, at laser fluences above the breakdown thresholds, acoustic responses were identical across various matrices, whereas at low fluences, the acoustic signal produced depended on the matrix and, hence, the normalisation of LIBS intensities to acoustic signals produced more consistent elemental determinations. Use of DP LIBS with acoustic signal normalisation for rock analysis significantly improved classification accuracy, from 91.8% when only using LIBS, to 97.3%. Use of a prototype portable LIBS system enabled¹⁹² the spatial distribution of Ti in quartz veinlets to be readily mapped in the field, although the results were semi-quantitative in nature because of the lack of matrix-matched RMs and optimised calibration algorithms. A drive for portability led to the development¹⁹³ of a miniaturised prototype LIBS system with data processing tools such as PCA. The use of a SVM model achieved a 99.6% classification accuracy for 16 rock types studied. Similarly, a handheld system was used¹⁹⁴ for the *in situ* mapping of iron meteorites that was superior to handheld XRF because low-atomic-number elements could be determined. Furthermore, improved compositional mapping using microspot analysis was available with which up to 40 elements could be measured.

Limitations in classifying rocks can be overcome by *synergistic instrumental use*. Here use of¹⁹⁵ LIBS now enabled petalite to be distinguished from spodumene using knowledge of the matrices gleaned from prior examination of Raman spectral information. In another study, a similar fusion¹⁹⁶ of LIBS and

Raman data improved classification accuracy to 99.7% for 11 distinct mineral types. Femtosecond LIBS minimises plasma thermal effects within the ablation zone compared to those created by ns laser pulses, thus leading to improvements in measurements. In an exploratory study, Mg/Ca and Sr/Ca ratios determined in a Himalayan stalagmite¹⁹⁷ tallied with $\delta^{13}\text{C}$ and $\delta^{18}\text{O}$ data thus validating the technique as a promising tool for high-resolution paleoclimatology. The performance of ns-LIBS and fs-LIBS for quantifying U and Th in twelve tantalum-niobium ores was compared¹⁹⁸ and benchmarked against reference measurements undertaken using HPGe- γ spectrometry. Based on parameters such as the goodness of calibration fit and measurement precision, use of fs-LIBS was deemed superior.

Novel sample manipulation techniques were applied to the interrogation of mineral particles by LIBS. Use¹⁹⁹ of an optical catapulting and trapping approach LIBS (OC-OT-LIBS) enabled individual meteorite particles to be suspended and analysed. The use of ternary plots enabled mineral phases to be differentiated and the application of calibration-free LIBS enabled semi-quantitative oxide compositions to be obtained. In the on-line analysis of powdered coal,²⁰⁰ a cylindrical sample confinement system improved particle flow stability, and the use of a relative S/N measurement approach enhanced the accuracy of proximate analysis models.

Planetary science remains a major LIBS application area. Under simulated lunar vacuum conditions of *ca.* 100 to 400 mTorr, it was demonstrated²⁰¹ that whilst LIBS was able to quantify 69 elements in pulverised and pelletised terrestrial rock standards, achievable LOQs for Br, C, K_2O , Rb and S were higher than typical concentrations present in Moon rock. Cross-calibration transfer approaches were proposed²⁰² for determining major element compositions across Earth, Mars, and Moon matrices that are impacted by different atmospheric conditions. On missions to Mars, harmonisation²⁰³ of LIBS data from the ChemCam and MarSCoDe rovers was achieved by cross-instrumental spectral harmonisation and peak position consistency correction protocols. This reduced average intensity differences and peak wavelength differences while lowering *rsmes* for oxide prediction.

5.4.2. Dating techniques. Recent advances in MC-ICP-MS/MS technology such as the NeomaTM MS/MS, allowed accurate determination of $^{87}\text{Sr}/^{86}\text{Sr}$ ratios in geological samples. Notably, this new instrument, now equipped with a CRC, exhibits advantages over conventional MC-ICP-MS for *in situ* Rb-Sr dating applications particularly to those samples with a high Rb/Sr ratio because the isobar $^{87}\text{Rb}^+$ interferant could now be mass shifted away using SF_6 allowing precise Sr IR measurements with RSDs <0.040% to be performed.

For U-Pb zircon dating by LA-MC-ICP-MS, the influence of ablation spot size (35–10 μm) and laser shot replicates (50–150) on downhole fractionation (DHF) precision and accuracy was assessed.²⁰⁴ Fewer repetitive shots improved $^{206}\text{Pb}/^{238}\text{U}$ accuracy by reducing standard-sample fractionation, especially for small spots. Method performance was benchmarked using the IAG 91500, GJ-1 and the Plesovice Princeton University zircon RMs. By using a 15 μm spot size with 150 laser shot replicates, the



variation in DHF($^{206}\text{Pb}/^{238}\text{U}$) between IAG 91500, taken as primary standard, and GJ-1 and Plesovice, taken as samples, was determined to be *ca.* 13%, and the ages were found to agree to <1.5% of the consensus values, but lowering the shot number to 50 reduced the DHF variation to *ca.* 2.4%, and improved age accuracy to <1%.

Simultaneous determination of U isotopic composition and particle age was demonstrated²⁰⁵ in U-containing microparticles using LA-MC-ICP-MS where the isotopic composition was derived from ^{234}U , ^{235}U , and ^{238}U abundances with dating derived from $^{230}\text{Th}/^{234}\text{U}$ measurements. Evaluation of the method using U particles of varying age and isotopic composition, produced results consistent with those obtained using LG-SIMS but highlighted a need for standards to correct for Th/U fractionation.

Improvements in dating applications were attributed to optimisation of sample preparation steps. Both thermal annealing and chemical abrasion procedures can impact²⁰⁶ zircon U–Pb dating by LA-ICP-MS, especially in ancient (~4.0–3.8 Ga) complex zircons. Post-annealing CA improved concordance and reduced scatter, while TA enhanced sample homogeneity. It was determined that HF leaching at 170 °C efficiently removed radiation-damaged zones and annealing partially repaired damage, but neither process altered Lu–Hf IRs or trace element compositions and enabled a better matching between samples and standards. In a related study,²⁰⁷ the CA impact on zircon U–Pb ages, O isotopes, and trace elements composition were examined using SHRIMP and LA-ICP-MS when it was determined that U–Pb ages from untreated RMs were systematically younger than those from CA-treated samples; whereas, isotopic compositions were unaffected, but some trace element variations were observed. A novel *in situ* triple-dating protocol²⁰⁸ combined the use of U–Pb, (U–Th)/He, and fission track methods on single apatite crystals thus enabling three independent age verifications. Apatites were mounted in a polymeric film, sectioned, and polished to ensure homogeneity. Improvements, included use of pit depth rather than volume in (U–Th)/He dating and optimal use of etching, demonstrated potential for resolving thermal histories and provenances with greater efficiency and higher spatial resolution.

A new low-cost sample preparation system for *radiocarbon dating* employed²⁰⁹ Zn as a reducing agent and Fe powder as a catalyst to convert CO_2 , generated from samples, to graphite. Capable of handling diverse sample matrices (organic matter, carbonates, water), the system achieved conversion efficiencies of 50–100% thus providing accurate AMS results even for very low-carbon containing samples of $\leq 0.01\%$ (m m^{-1}), such as arid or agricultural soils.

5.4.3. Inductively coupled plasma mass spectrometry. *Geochemical analysis by ICP-MS* was reviewed²¹⁰ (146 references) with a focus on drift correction, calibration strategies, and laser ablation microsampling. In a tutorial review on non-traditional isotopic analyses by MC-ICP-MS²¹¹ (115 references), the importance of sample preparation and chemical purification steps in the production of high-precision measurements to provide reliable isotopic data for geological RMs was emphasised.

The attributes of the *prototype CC-MC-ICP-MS/MS Proteus* were exemplified²¹² through the *in situ* LA determination of Ti in stardust. Benefits of one configuration included the exclusion of undesirable ions such as Ar^+ from the CC using a mass filter with improved resolution and a mass-shift protocol to avoid isobaric interferences.

*Micro-ultrasonic single-droplet nebulisation*²¹³ was used in the determination of $\delta^7\text{Li}$ in a basalt RM by MC-ICP-MS. Ultra low sample volumes of only 0.5–8 μL were deposited on a nebulizer foil and aerosolised, generating transient signals that lasted seconds but producing data comparable to that obtained with more conventional nebulisation. Benefits included reduced washout times, a 17-fold sensitivity enhancement, improved long-term precision with a sample mass requirement of only *ca.* 1 ng.

Use of LA-ICP-MS is advantageous for *spatially-resolved trace element mapping*. Using a numerical inversion method that involved²¹⁴ fitting, deconvolution, regularization, and boundary restoration, spatial resolution was improved *ca.* 18-fold compared to original data interrogation so improving the analysis of barite, pyrite, apatite, and zircon samples. High-resolution 2D geochemical imaging of biogenic carbonates was achieved²¹⁵ via LA-TOF-ICP-MS at a 1–2 μm pixel resolution and a mapping rate of 200 pixels per s enabled microscale variability in Ba, Mg, Sr and U to be determined in coral skeletons, coralline algae, and foraminifera. The technique provided both cost- and time-effective alternatives to synchrotron X-ray spectroscopy, SIMS, and EMPA.

The typically low I to Ca ratios found in carbonate rocks were more readily determined²¹⁶ with a SCGD sample introduction system coupled to ICP-MS. This enhanced the I signal 100-fold and decreased the Ca signal 70-fold compared with those of conventional nebulisation, thus improving accuracy and precision.

5.4.4. Secondary ion mass spectrometry. Studies to improve *accuracy in measurements using SIMS* were reported. Alleviation of matrix effects in the determination of oxygen isotopes in silicates was a focus of one publication.²¹⁷ Variations in the IMF due to sample chemical composition were characterised, and regression models proposed to correct for such effects. The researchers recommended the use of quartz as a universal “zero” point for IMF normalisation. Instrumental artefacts arising from near-simultaneous arrival of secondary ions at the EM can lead²¹⁸ to undercounting and thus inaccurate isotope ratios, particularly under high count rates or when there is a mismatch between sample and RM instrumental conditions. A procedure to determine the QSA coefficient (β) experimentally was developed with illustrative $\delta^{34}\text{S}/\delta^{32}\text{S}$ measurements performed to demonstrate its corrective powers.

The use of *nanoSIMS* has revealed significant isotopic heterogeneity at the micrometer scale in pyrites. Individual Ediacaran pyrite grains, previously assumed to be homogeneous, displayed²¹⁹ $\delta^{34}\text{S}$ variations of up to 69.3‰ over a 1–5 μm scale thus highlighting the need for analysis at high spatial resolution for a better understanding of ancient biogeochemical processes. The interrogation of Archean sedimentary pyrite grains with a 0.2 μm Cs^+ ion beam enabled²²⁰ a resolution of



only $1\ \mu\text{m}^2$ and a precision of *ca.* 1‰ (1SD) for $\delta^{34}\text{S}$ measurements. An integrated nanoSIMS method for the simultaneous measurements of O isotope ratios and volatile components (Cl, F, H_2O , SO_3) in apatite was reported²²¹ at a lateral resolution of $\sim 7\ \mu\text{m}$ following optimisation of detector configuration, raster area, and primary beam current. While oxygen isotope data was less precise relative to that obtainable by LG-SIMS, total spot measurement time was only *ca.* 6 min, and LODs were sufficiently low to quantify volatiles at ppm levels. Analyses of eight apatite RMs produced results consistent with published data. A high-spatial-resolution methodology for Mg isotope determinations in olivines at the micrometer scale incorporated²²² online correction of both matrix and fractionation effects using an empirical model based on the use of the so-called BiHill equation. When applied to the analysis of lunar olivine samples from the Chang'e-5 mission, $\delta^{26}\text{Mg}$ variations exceeding 4‰ over distances of $<100\ \mu\text{m}$ were revealed.

Stable carbon isotope measurements in basaltic glasses were determined²²³ after meticulous optimisation of LG-SIMS protocols. To minimise volatile carbon contamination, samples were typically degassed under vacuum overnight. Method blanks were quantified using carbon-free olivine, and corrections applied for any residual organic blank contributions. The $^{12}\text{C}^-$ and $^{13}\text{C}^-$ ions were measured simultaneously by EM detectors, whereas reference masses ($^{30}\text{Si}^-$ or $^{18}\text{O}^-$) were collected by a $10^{11}\ \Omega$ Faraday cup. Internal drift was corrected on a per-analysis basis, while external drift was addressed through frequent analysis of RMs. Achievable internal precision for $\delta^{13}\text{C}$ measurements was $\pm 0.35\text{‰}$ (1RSE) at sample concentrations of $1706\ \mu\text{g g}^{-1}$ (expressed as a CO_2 equivalent content) and $\leq \pm 1.00\text{‰}$ or better for concentrations between 163 and $267\ \mu\text{g g}^{-1}$.

In a *comparative study*²²⁴ for the determination of S isotopes in a natural marcasite sample, minor discrepancies of $<1.5\text{‰}$ between SIMS and LA-MC-ICP-MS and GS-IRMS measurements were observed but were not attributable to crystal orientation effects in SIMS measurements, which hitherto had not been unexplored.

5.4.5. X-ray fluorescence spectrometry and related techniques. The use of a radio isotope excitation source improved²²⁵ sensitivity for REE determinations compared to that obtainable with a silver anode X-ray tube. The Am-241 source enabled excitation across a broader elemental range, from Ca ($Z = 20$) to Gd ($Z = 64$), and optimisation of the source-sample-detector geometry maximised analytical sensitivity while reducing background. Instrumental performance was verified against soil RMs and comparison with INAA and ICP-MS results.

A *WD-XRF* protocol for gold quantification in geological matrices such as rocks and soils involved²²⁶ *aqua regia* digestion, evaporation to dryness, and subsequent WD-XRF measurement. So avoiding the environmental and safety hazards associated with the more common lead oxide fire assay or MIBK solvent extraction. The LODs were $20\text{--}70\ \mu\text{g kg}^{-1}$ using gold-enriched hematite standards as calibrants. Results were in good agreement with those obtained by fire assay coupled with ETAAS, and analyses of two USGS CRMs demonstrated acceptable accuracy according to the AOAC guidelines.

A new approach for *quantitative TXRF analysis*²²⁷ of complex matrices, such as oceanic polymetallic nodules, addressed the problem of spectral overlaps by using LS deconvolution of measured spectra into weighted sums of simulated elemental subspectra. This was advantageous because use of only one matrix-matched reference standard was now required. Comparative evaluation against an external calibration approach with IS correction for 11 elements demonstrated the accuracy of the new method, particularly when calibration materials are limited.

X-ray computed tomography quantitative mineral mapping at the nanoscale has been advanced²²⁸ by the development of a mathematical model exploiting the linear relationship between X-ray attenuation and elemental concentration and applying Bayesian decision theory to match voxel-wise attenuation to reference attenuation distributions from pure mineral standards. The algorithm assigns the most probable composition to each voxel thus enabling high-resolution 3D mineral maps to be constructed. Application of this approach to binary (Ca, Cd) CO_3 and ternary (Ca, Cd, Zn) CO_3 test carbonates demonstrated accurate mineral identification and mapping.

Fusion of NIR and XRF spectral information has emerged as a powerful approach for classifying²²⁹ coal quality. An initial SVM model was used to identify coal type prior to use of PLS regression for predicting ash, volatile matter, and sulfur content, resulting in a classification accuracy of up to 96%. A similar fusion approach was deployed²³⁰ on an integrated coal analyser system enabling rapid and automated coal classification, improved repeatability, reduced analysis time, enhanced safety, and better detection of sub-standard coal compared with the performance of conventional approaches.

The first application of a *neural network* (NN) for the quantification²³¹ of homogeneous bulk samples by confocal $\mu\text{-XRF}$ significantly simplified data evaluation and effectively eliminated the need for human intervention, requiring no equipment characterization, elemental selection, deconvolution, or initial parameters. The NN training relied on simulated data derived from the elemental compositions of CRMs stored in the GeoReM database. The model predicted sample densities within $\pm 30\%$, with spatial accuracies within $\pm 10\ \mu\text{m}$. While accuracy was marginally lower than that of conventional FP approaches, processing speed increased by *ca.* 10^5 , and eliminated the need for instrument-specific calibrations or deconvolution protocols.

The *hierarchical convolutional network* with attention excitation (HCNAE) architecture was designed²³² for elemental analysis of minerals by XRF. This approach improved resilience to matrix effects, line interference, and instrumental noise. Comparative tests demonstrated superior predictive accuracy and robustness relative to those of conventional machine and deep learning models.

In the classification²³³ of vanadiferous titanomagnetite ore rock by XRF, the performances of six *supervised models*, namely SVM, RF, extreme gradient boosting (XGBoost), light gradient boosting machine, DNN and 1D-CNN were evaluated. Use of the 1D-CNN model delivered the best predictive accuracy,



underscoring its potential to enhance operational efficiency in underground mining.

5.4.6. Other techniques. Use of μ -Raman in combination with LA-ICP-MS and multivariate statistical tools aided²³⁴ *provenancing of emeralds*. Characteristics such as Raman shifts, peak intensities, z and crystal orientation were studied for gem and crystal emeralds from 11 different global deposits. It was found that, for example, Colombian emeralds exhibited a distinct clustering pattern with characteristic Raman signatures, notably in the N_2 and CO_2 bands. Dimensionality reduction of Raman information and LA-ICP-MS elemental datasets was facilitated using PCA, while LDA on the resultant combined PCA scores enabled advanced origin discrimination, successfully differentiating deposits from various regions.

The use of N_2 as an ablation and transport gas in LA-microwave-sustained inductively coupled atmospheric-pressure plasma mass spectrometry (MICAP-MS) was compared²³⁵ with He and Ar in the analyses of geological RMs. Parameters such as sensitivity, quantification capability, and particle size and morphology under different laser conditions and cell geometries were evaluated. Nitrogen was found to be a cost-effective alternative despite the differences seen in aerosol morphology and transient signal profiles. The use of Al cones instead of Pt further reduced operational costs.

An improved TIMS instrument employed²³⁶ a dual-focusing Nier-Johnson geometry with improved ion energy control, transmission efficiency, and mass resolution. Furthermore, an advanced symmetrical five-electrode retarding filter provided both energy and directional filtering, thereby reducing peak tailing and improving abundance sensitivity from <2 ppm to <5 ppb. A detector array consisting of 16 FCs and 4 discrete dynode secondary EMs with double quadrupole zoom lenses enabled simultaneous collection of multiple isotopes with precisions <4 ppm. Use²³⁷ of a $MoSi_2$ emitter enhanced Cd ionization efficiency enabling a reduction in the required sample mass from 100 ng to only 6.5–9 ng whilst maintaining a precision of $\pm 0.051\%$ (3 ng Cd, 2SD) in $\delta^{114/110}Cd$ measurements of NIST SRM 3108 (cadmium standard solution).

In a matrix-assisted ionisation TOF-MS method for rapid U isotope ratio determination²³⁸ the addition of 3-nitrobenzonitrile to samples in 2% HNO_3 generated volatile uranyl trinitrates $^{235}UO_2(NO_3)_3^-$ or $^{238}UO_2(NO_3)_3^-$ under vacuum, allowing analyses to be performed within minutes eliminating the need for sample purification. Enrichment differences as small as 0.2–0.3% were resolved in solutions that contained only 200–500 pg U.

Determination²³⁹ of Pb and trace element isotope ratios in glass and zircon RMs using an improved LA-VUV-TOF system enabled $^{207}Pb/^{206}Pb$ and $^{208}Pb/^{206}Pb$ precisions of <1.6% (2SD), matching ID-TIMS values. Other advantages included ablation spots of $\leq 2 \mu m$ compared to $>20 \mu m$ for LA-ICP-MS and 5–10 μm for SIMS, high sensitivity, stability, calibration-free operation, and no requirement for metallic sample coatings.

Sample preparation guidelines for high-precision CF-IRMS analysis of $\delta^{13}C$ and $\delta^{18}O$ in calcite, dolomite, and magnesite were issued²⁴⁰ following optimisation of the acidification step to release CO_2 . The influence of mineral grain size, reaction

temperature, and time on CO_2 production were studied to reduce non-equilibrium isotope effects and ^{18}O exchange with water. Time-resolved evolution of phosphoric acid-released CO_2 confirmed $\delta^{18}O_{CO_2}$ drift was unavoidable.

A V-shaped cavity optical feedback/cavity ring-down spectroscopy (CRDS) instrument deployed²⁴¹ for O isotope ratio measurements in water and carbonate RMs used a stabilised near-IR laser diode in a low-pressure V-shaped cavity, with acousto-optical wavelength modulation, thus providing 0.004‰ precision in $\Delta^{17}O$ measurements within 10 min. Measurements with this technique then allowed robust linking of VSMOW-SLAP and VPDB scales by providing updated O isotope values for NBS and IAEA carbonate standards.

The matrix effects in SHRIMP-stable isotope analysis²⁴² were corrected by using LA-ICP-MS elemental data. In the triple O isotope analysis of stony micrometeorites, removal of IMF using San Carlos olivine ($\delta^{18}O = 5.27\%$) improved $\delta^{18}O$ and $\delta^{17}O$ values. This combined with LS modelling of idealised olivine-basaltic glass-iron oxide mixtures improved $\delta^{18}O$ accuracy, so results for East Antarctic cosmic spherules agreed with those of prior bulk method.

The determination²⁴³ of Li isotope ratios in geological samples by HR-CS-AAS utilised the 15 pm wavelength difference between the $2^2P \leftarrow 2^2S$ transition at 670.8 nm to resolve 6Li from 7Li . Data analysis using extreme gradient boosting ML algorithms available in the open source XGBoost software, yielded δ^7Li precisions of 1.0–2.5‰ at an instrumental resolution of $\lambda/\Delta\lambda \approx 780\,000$, for samples with δ^7Li values ranging from ± 0.5 to 4.5‰, these results were not significantly different compared to MC-ICP-MS data.

The quantification of REEs, Th and U by k_0 -NAA in Egyptian monazite sands was hampered²⁴⁴ by neutron self-shielding. This was alleviated by sequential sample dilution using SiO_2 to derive an empirical correction factor from exponential fitting of mass-specific count rates versus diluted values. This protocol was validated using a synthetic monazite and comparative analysis with ICP-MS. The authors noted that the advantages were that their procedure avoided *a priori* compositional knowledge and yielded negligible spectral/nuclear interferences or γ self-attenuation effects.

Use of both TOF-SIMS and resonant laser secondary neutral mass spectrometry (rL-SNMS) facilitated²⁴⁵ the mapping of Pu diffusion in Opalinus clay where the latter technique, despite its lower intensities, confirmed the $^{242}Pu^+$ distributions obtained by TOF-SIMS. The Pu in the pore water occurred mainly as PuO_2^+ , as verified by CE-ICP-MS and displayed a lower mobility than those of other actinides under similar conditions.

An EPMA protocol for accurate N quantification in silicate and oxide minerals and glasses was proposed²⁴⁶ whose use of multi-point background corrections and a peak area factor improved accuracy. Improvements included optimisation of beam parameters to limit N mobility and use of Python scripts for community adoption. The use of nitrides such as BN or GaN as RMs was recommended.

Calibration²⁴⁷ of a spatially resolved scanning transmission electron microscopy-mapping electron energy loss spectroscopic (STEM-EELS) procedure enabled Fe^{3+} determination at



Table 14 Summary of analytical software and algorithms described in recent literature

| Analytes and/or sample | Algorithm or software | Technique | Comments | References |
|---|---|---|--|------------|
| Apatite | Integrated open-source fission track software (Trax®) | LA-ICP-MS with fission track analysis | New LA-ICP-MS protocol for apatite dating using Trax® software integrates fission track length measurements with mineral geochemistry. Ages derived from modified xi calibration approach, ξ ICP (U/Ca-based), and absolute U calibration match EDM results on RMs | 419 |
| 40 elements in Regolith and parent rock materials | DataMosaic™ + user-supervised algorithm (uTSA) + multi-feature extraction methods (MFEMs) | pXRF, VNIR-SWIR hyperspectral, wireline logging, including natural gamma, inductive conductivity, and magnetic susceptibility | Multivariate ML and wavelet-based framework combining hyperspectral, geochemical and petrophysical data for boundary detection Enabled more precise delineation of regolith boundaries and internal zoning than manual or geochemical-only methods | 252 |
| Signals were measured for 47 <i>m/z</i> ratios in tungstates and silicates (scheelite and garnet) | G.O.Joe platform independent web application | LA-ICP-MS | Dart-based browser application for LA-ICP-MS data processing including multi-step correction workflow Improved correction accuracy, data quality, and consistency in multi-elemental analysis of geological materials | 250 |
| General LA-ICP-MS datasets | ICPMSDataCal-Py | LA-ICP-MS | Python open-source package with scalable calibration and isotopic formula editor Enhanced computational efficiency and flexible calibration across isotopic systems | 251 |
| Gold grains (trace element analysis) | OreGenes (MATLAB) | Geochemical analysis of gold grains | Neural network-based classification using PCA-selected elements for deposit-type prediction Accurately classified gold deposit types and linked trace elements to structural defects | 420 |
| General applications | Hklhop, open-source software package | Hard X-ray samples using spherically curved crystal analysers (SBCAs) | Python tool for asymmetric Rowland circle configuration optimisation of SBCAs Reduced Johann broadening and increased operational flexibility while lowering costs | 421 |
| Meteorite and geological samples | TOFHunter | ICP-TOF-MS | Python package using PCA and interesting feature finder (IFF) for unbiased data exploration Revealed key elemental correlations and interferences without prior compositional knowledge | 422 |
| Homogeneous solid samples | CNN-MLP model | CMXRf | AI-based approach combining CNN feature extraction with MLP prediction trained on simulated data Achieved 3D quantification of 53 elements with <30% deviation and 1 000 00× faster than traditional models | 231 |





Table 14 (Contd.)

| Analytes and/or sample | Algorithm or software | Technique | Comments | References |
|--|--|--------------------|---|------------|
| Minerals containing Cu, Zn, Pb | Hierarchical convolutional network with attention excitation | XRF | DL model integrating convolutional layers with Squeeze-and-Excitation attention mechanism Outperformed existing ML/DL models in heavy-metal quantification accuracy and robustness | 232 |
| Zircon (O isotopes), RMs (S isotopes) | CSIDRS open-source software | SIMS | Software using Monte Carlo uncertainty propagation for isotope data reduction Provided higher precision and reproducibility than spreadsheet-based reduction methods | 423 |
| Source rock samples (76) | Multi-block chemometric model (PCA, PLS, HPLS) | NIR, FT-Raman, XRF | Hierarchical data integration and variable selection via VIP scores for spectral data fusion | 424 |
| Lithium-bearing minerals, e.g. quartz-amblygonite, albite-lepidolite-zinnwaldite | LIBS clustering algorithm | LIBS | Produced improved unsupervised clustering and interpretability of rock source classification Baseline removal, Gaussian filtering and k-means clustering for mineral discrimination Successfully identified complex mineral assemblages validated against petrographic analysis | 425 |
| Iron ores (by grade/origin) | DP-LIBS classification (PCA + k-means) | DP-LIBS | Multivariate approach combining PCA and k-means for unsupervised clustering of spectral data Achieved >94% classification accuracy by grade and origin using atomic and molecular emissions | 426 |
| Multielemental LIBS spectra | Semi-automated elemental identification algorithm | LIBS | Comb-shaped spectral filter-based algorithm for semi-supervised qualitative analysis Enabled autonomous interference detection and improved reliability of elemental assignment | 427 |
| Li-bearing minerals (e.g. petalite, spodumene) | Multimodal spectral knowledge distillation (LIBS + Raman) | LIBS + Raman | Knowledge transfer framework aligning Raman (teacher) and LIBS (student) models Improved classification accuracy for spectrally similar lithium minerals | 195 |
| Polymetallic nodules | GANN with physics-based loss | LIBS | Augmenting limited LIBS datasets Improved predictive accuracy for Ni, Co and Li quantification compared to baseline ML models | 428 |
| LIBS and Raman spectra for mineral classification | Adaptive nonlinear mapping (CNN-based image classification) | LIBS + Raman | Feature extraction via intensity, width, and area conversion into 2D image representation Achieved 99.7% accuracy and superior performance compared with PCA and RF approaches | 196 |

submicron scales in materials such as hornblende, magnetite, and hematite for the first time. A correlation between Fe-L₃/L₂ peak area ratios and Fe³⁺/ΣFe was established using pyroxene RMs. Recommended optimal sample thickness and instrumental parameters (residence and integration time) were presented.

The first application²⁴⁸ of *photon counting computed tomography (PC-CT)* to mineralogical investigations as an alternative to conventional attenuation-contrast X-ray CT was reported. The authors built a prototype PC-CT with multi-pixel photon counters that demonstrated improved low-energy contrast *versus* that of traditional CT when quartz and calcite were interrogated as model mineral phases. Outcomes suggested that the production of high-contrast images of minerals was feasible, thus enabling mineral phases with different attenuation curves to be distinguished, even when their CT values are similar.

5.5. Software and databases

A recent tutorial article (163 references) provided²⁴⁹ a detailed guide for the application of *Random Forest (RF) tool* to interrogate data obtained by TOF-SIMS emphasised its advantage in the classification of complex chemical compositions. Critical aspects such as data preprocessing, hyperparameter optimisation, and the management of multicollinearity were also addressed, highlighting the potential of RF for advanced mass image analysis.

Recent *analytical advancements that focus on integrating diverse techniques with sophisticated chemometrics and ML* for enhanced geological analysis are summarised in Table 14. Notably LA-ICP-MS data processing has seen improvements through platform-independent web applications²⁵⁰ and open-source Python packages²⁵¹ to increase calibration flexibility and computational efficiency. As reported within, techniques like LIBS and XRF now utilise^{231,232} DL models for rapid, accurate 3D elemental quantification and robust heavy-metal analysis. Furthermore, combining multimodal data (e.g., LIBS + Raman, pXRF/hyperspectral/wireline)²⁵² with chemometric models (e.g., PCA, PLS) or knowledge distillation frameworks improves mineral classification, boundary detection, and source rock characterization. This integration yields superior precision and interpretability across various geological samples, including regolith, gold grains, and apatite.

6. Glossary of abbreviations

| | |
|-----|----------------------------------|
| 3D | three dimensional |
| AAS | atomic absorption spectrometry |
| ABS | acrylonitrile butadiene styrene |
| AEC | anion-exchange chromatography |
| AES | atomic emission spectrometry |
| AFM | atomic force microscopy |
| AFS | atomic fluorescence spectroscopy |
| AI | artificial intelligence |
| AMS | accelerator mass spectrometry |
| AMU | atomic mass unit |

| | |
|---------|--|
| APA | automated particle analysis |
| APGD | atmospheric pressure glow discharge |
| APM | atmospheric particulate matter |
| BAM | Federal Institute for Materials Research and Testing (Germany) |
| BP-ANN | back propagation-artificial neural network |
| BPNN | backpropagation neural networks |
| C18 | octadecyl bonded silica |
| CA | chemical abrasion |
| CC | collision cell |
| CCD | charge coupled device |
| CCT | collision cell technology |
| CE | capillary electrophoresis |
| CF | continuous flow |
| CFD | computational fluid dynamics |
| CF-IRMS | continuous-flow isotope ratio mass spectrometry |
| CI | confidence interval |
| CIMS | chemical ionisation mass spectrometry |
| CISH | cross-instrument spectral harmonisation |
| CMOS | complementary metal oxide semiconductor |
| CMPO | octyl(phenyl)-N,N-diisobutylcarbamoylmethylphosphine oxide |
| CMXRF | confocal micro-XRF |
| CNN | convolutional neural network |
| CNPGAA | cold neutron prompt gamma activation analysis |
| CPE | cloud point extraction |
| CRC | collision/reaction cell |
| CRCCRM | Chinese Research Centre for Certified Reference Materials |
| CRDS | cavity ring-down spectroscopy |
| CRM | certified reference material |
| CS | continuum source |
| CT | computed tomography |
| CTAB | cetyltrimethylammonium bromide |
| CV | cold vapour |
| CVG | chemical vapour generation |
| CyTOF | cytometry by time of flight |
| D50 | particle size at which there is a 50% collection efficiency |
| DBSCAN | density-based clustering of applications with noise |
| DECT | dual-energy computed tomography |
| DES | deep eutectic solvent |
| DF-PLSR | dominant factor-based partial least squares regression model |
| DHF | downhole fractionation |
| DL | deep learning |
| DLLME | dispersive liquid-liquid microextraction |
| DMA | dimethylarsenic |
| DNN | deep neural network |
| DP-LIBS | double-pulse laser-induced breakdown spectroscopy |
| DPTA | diethylenetriaminepentaacetic acid |
| EA | elemental analyser |
| EC | environment Canada |
| ECCC | environment and climate change Canada |
| ED | energy dispersive |
| EDM | external detector method |
| EDS | energy dispersive spectrometry |
| EDTA | ethylenediaminetetraacetic acid |



| | | | |
|----------------|--|----------|--|
| EDXRF | energy dispersive X-ray fluorescence | JNA | Johann normal alignment |
| EF | enrichment factor | KNN | <i>k</i> -nearest neighbour |
| ELPI | electrical low pressure impactor | LA | laser ablation |
| EM | electron multiplier | LABQ3 | linear attenuation Bayesian quantitative 3D-mapper |
| EMS | exospheric mass spectrometer | LAMIS | laser ablation molecular isotopic spectrometry |
| EPA | environmental protection agency (USA) | LASMA-LR | laser-ionisation mass spectrometer – low resolution |
| EPMA | electron probe microanalysis | LDA | linear discriminant analysis |
| ERDA | elastic recoil detection analysis | LF-IRMS | laser fluorination isotope ratio mass spectrometry |
| ERM | European Reference Material | LGBM | light gradient boosting machine |
| ESI | electrospray ionisation | LG-SIMS | large-geometry secondary ion mass spectrometry |
| ETAAS | electrothermal atomic absorption spectrometry | LIBS | laser-induced breakdown spectroscopy |
| ETMAS | electrothermal molecular absorption spectrometry | LIF | laser-induced fluorescence |
| EtOH | ethanol | LIMAS | laser ionisation mass analyser |
| FAAS | flame atomic absorption spectrometry | LIPAc | laser induced plasmas acoustic signals |
| FC | faraday cup | LLE | liquid–liquid extraction |
| FFF | field flow fractionation | LLME | liquid–liquid microextraction |
| FHP | fast hot-pressing | LOD | limit of detection |
| FWHM | full width at half maximum height | LOQ | limit of quantification |
| GANN | generative adversarial neural network | LPME | liquid phase microextraction |
| GC | gas chromatography | LS | least squares |
| GeoPT | International Program for Professional Testing of Geoanalytical Laboratories | MAD | microwave-assisted digestion |
| GOM | gaseous oxidised mercury | MAE | microwave-assisted extraction |
| Grad-CAM | gradient-weighted class activation mapping | MC | multicollector |
| GS-IRMS | gas-source isotope ratio mass spectrometry | MCE | mixed cellulose ester |
| GSJ | Geological Survey of Japan | MDL | method detection limit |
| GSR | gunshot residues | MEMS | micro-electro-mechanical system |
| HCNAE | hierarchical convolutional network with attention excitation | MeOH | methanol |
| HG | hydride generation | MFEM | multi-feature extraction method |
| HI | hyperspectral imaging | MICAP | microwave inductively coupled atmospheric-pressure plasma |
| HPA | high-pressure ashing | MIP | microwave induced plasma |
| HPGe- γ | high-purity germanium γ -ray | ML | machine learning |
| HPLC | high performance liquid chromatography | MLP | multilayer perceptron |
| HPLS | hierarchical partial least squares | MMA | monomethylarsenic |
| HR | high resolution | MMAD | mass median aerodynamic diameter |
| HTC | high-temperature conversion | MMWCNT | magnetic multiwalled carbon nanotube |
| IAEA | International Atomic Energy Agency | MNP | magnetic nanoparticles |
| IC | ion chromatography | MOF | metal–organic framework |
| ICP | inductively coupled plasma | MOUDI | micro orifice uniform deposit impactor |
| ICP-AES | inductively coupled plasma atomic emission spectrometry | MP | microplastic |
| ICP-MS | inductively coupled plasma mass spectrometry | MPT | microwave plasma torch |
| ICP-TOF-MS | inductively coupled plasma time of flight mass spectrometry | MS | mass spectrometry |
| ID | isotope dilution | MS/MS | tandem mass spectrometry |
| ID-TIMS | isotopic dilution thermal ionization mass spectrometry | MSWD | mean squared weighted deviation |
| IEC | ion exclusion chromatography | MU | measurement uncertainty |
| IFF | interesting feature finder | μ CT | microscale X-ray computed tomography |
| IGGE | Institute of Geophysical and Geochemical Exploration | MWCNT | multi-walled carbon nanotubes |
| ILC | interlaboratory comparison | NAA | neutron activation analysis |
| IMF | instrumental mass fractionation | NBS | National Bureau of Standards |
| INAA | instrumental neutron activation analysis | Nd:YAG | neodymium doped yttrium aluminium garnet |
| IR | isotope ratio | NIES | National Institute for Environmental Studies (Japan) |
| IRMS | isotope ratio mass spectrometry | NIMC | National Institute of Metrology of China |
| IS | internal standard | NIOSH | National Institute of Occupational Safety and Health (USA) |
| ISO | International Organization for Standardisation | NIR | near infra-red |
| | | NIST | National Institute of Standards and Technology (USA) |



| | | | |
|------------|---|-----------|---|
| NMIJ | National Metrology Institute of Japan | S/N | signal-to-noise ratio |
| NN | neural network | SBCA | spherically bent crystal analyser |
| NP | nanoparticle | SBET | simplified bioaccessibility extraction test |
| NRA | nuclear reaction analysis | SCGD | solution cathode glow discharge |
| NRCC | National Research Council of Canada | SE | standard error |
| NRCM | National Research Center for Certified Reference Materials (China) | SEM | scanning electron microscopy |
| NRMSE | normalised root mean square error | SES | spark emission spectroscopy |
| NTIMS | negative thermal ionization mass spectrometry | SF | sector field |
| OC-OT-LIBS | Optical catapulting-optical trapping LIBS | SF-ICP-MS | sector-field inductively coupled plasma mass spectrometry |
| OES | optical emission spectrometry | SFODME | solidified floating organic drop microextraction |
| PCA | principal component analysis | SHM-IRMS | step-heating extraction and manometry combined with isotope ratio mass spectrometry |
| PC-CT | photon counting computed tomography | SHRIMP | sensitive high-resolution ion microprobe |
| PCM | phase contrast microscopy | SHRIMP-SI | SHRIMP stable isotope |
| PENS | personal nanoparticle sampler | SIMS | secondary ion mass spectrometry |
| PERI | potential ecological risk index | SIMS-SAMS | secondary ion mass spectrometry-single stage accelerator mass spectrometry |
| PET | polyethylene terephthalate | SLAP | standard light Antarctic precipitation |
| PGE | platinum group element | SN | solution nebulisation |
| PIGE | particle induced γ -ray emission | sp | single particle |
| PIXE | proton induced X-ray emission | SPE | solid-phase extraction |
| PLI | pollution load index | SR | synchrotron radiation |
| PLS | partial least squares | SRM | standard reference material |
| PLSR | partial least squares regression | SSB | standard sample bracketing |
| PM1.0 | particulate matter (with an aerodynamic diameter of up to 1.0 μm) | SSML | semi supervised machine learning |
| PM10 | particulate matter (with an aerodynamic diameter of up to 10 μm) | SVM | support vector machine |
| PM2.5 | particulate matter (with an aerodynamic diameter of up to 2.5 μm) | TA | thermal annealing |
| PMMA | poly(methyl methacrylate) | TCE | technology-critical element |
| ppmv | part per million volume | TCEA-IRMS | thermal conversion elemental analyser combined with IRMS |
| PS | polystyrene | TD | thermal desorption |
| PSL | polystyrene latex | TEM | transmission electron microscopy |
| PS-MP | polystyrene microplastic | TIMS | thermal ionisation mass spectrometry |
| PT | proficiency testing | TL | transfer learning |
| PTE | potentially toxic element | TOC | total organic carbon |
| PTFE | polytetrafluoroethylene | TOF | time of flight |
| PTR | proton transfer reaction | TXRF | total reflection X-ray fluorescence |
| PVC | polyvinylchloride | UAE | ultrasound-assisted extraction |
| PVG | photochemical vapour generation | URE | ultra fine particle |
| pXRD | portable X-ray diffraction | UNDBD | ultrasound nebulization-dielectric barrier discharge |
| pXRF | portable X-ray fluorescence | UPLC | ultra performance liquid chromatography |
| Py | pyrolysis | USGS | United States geological survey |
| Q/SF | quadrupole or sector field | USN | ultrasonic nebulizer |
| QA | quality assurance | UTEVA | uranium and tetravalent actinides |
| QC | quality control | uTSA | user-supervised algorithm |
| QCL | quantum cascade laser | UV | ultra-violet |
| QMS | quadrupole mass spectrometry | VALLME | vortex assisted liquid liquid microextraction |
| QT | quartz tube | VCOF-CRDS | V-shaped cavity optical feedback/cavity ring-down spectroscopy |
| RCS | respirable crystalline silica | VG | vapour generation |
| REE | rare earth element | VIP | variable influence on projection |
| rf | radio frequency | VNIR-SWIR | visible, near-infrared, and short-wave infrared |
| RF | random forest | VOC | volatile organic compound |
| RL-SNMS | resonant laser secondary neutral mass spectrometry | VPDB | Vienna Pee Dee Belemnite |
| RM | reference material | VSMOW | Vienna Standard Mean Ocean Water |
| rmse | root mean square error | | |
| RSD | relative standard deviation | | |



| | |
|---------|---|
| VUV-TOF | vacuum ultraviolet laser ablation/ionization time-of-flight mass spectrometry |
| WD-XRF | wavelength dispersive X-ray fluorescence |
| WEPAL | Wageningen Evaluating Programs for Analytical Laboratories |
| XAFS | X-ray absorption fine structure |
| XANES | X-ray absorption near-edge structure |
| XGBoost | extreme gradient boosting |
| XRD | X-ray diffraction |
| XRF | X-ray fluorescence |
| XRFS | X-ray fluorescence spectroscopy |
| μ-APD | atmospheric microplasma discharge |
| μ-XANES | micro-X-ray absorption near edge structure spectroscopy |
| μ-XRF | micro X-ray fluorescence |

Conflicts of interest

The authors declare no conflict of interest. The contents of this paper, including any opinions and/or conclusions expressed, are those of the authors alone and do not necessarily reflect HSE policy.

Data availability

There is no additional data associated with this article.

References

- W. R. L. Cairns, O. T. Butler, O. Cavoura, C. M. Davidson, J.-L. Todolí-Torró and M. V. D. Au, *J. Anal. At. Spectrom.*, 2025, **40**(1), 11–69.
- M. Patriarca, N. Barlow, A. Cross, S. Hill, D. Milde and J. Tyson, *J. Anal. At. Spectrom.*, 2025, **40**(3), 541–664.
- E. H. Evans, J. Pisonero, C. M. M. Smith and R. N. Taylor, *J. Anal. At. Spectrom.*, 2025, **40**(5), 1136–1157.
- R. Clough, C. F. Harrington, S. J. Hill, Y. Madrid and J. F. Tyson, *J. Anal. At. Spectrom.*, 2025, **40**(7), 1615–1644.
- C. Vanhoof, A. Cross, U. E. A. Fittschen and L. Vincze, *J. Anal. At. Spectrom.*, 2025, **40**(9), 2275–2289.
- A. Agarwal, E. Bolea-Fernandez, R. Clough, A. Fisher, B. Gibson and S. Hill, *J. Anal. At. Spectrom.*, 2025, **40**(11), 2982–3022.
- I. Han, C. Lee, C. Belchez, A. G. Shipper and K. E. Wiens, *Environments*, 2024, **11**(11), 256.
- J. H. Seo, Y. Shin, I.-g. Song, J. Lim, Y. S. Ok and S. Weon, *TrAC, Trends Anal. Chem.*, 2024, **178**, 117859.
- T. Lei, W. Xiang, B. Zhao, C. Hou, M. Ge and W. Wang, *Sci. Total Environ.*, 2024, **949**, 175045.
- K. Lehtipalo, T. Nieminen, S. Schobesberger, M. Ehn, M. Kulmala and V.-M. Kerminen, *J. Aerosol Sci.*, 2025, **184**, 106494.
- L. N. Zheng, W. T. Feng, Z. L. Huo, J. L. Li, W. F. Xuan and Z. Han, *Anal. Methods*, 2025, **17**(20), 4103–4123.
- S.-H. Bae, E. Chae, Y.-S. Park, S.-W. Lee, J.-H. Yun and S.-S. Choi, *Sci. Total Environ.*, 2024, **944**, 173948.
- M. Haugen, P. Bühler, S. Schläfle, D. O'Loughlin, S. Saladin, C. Giorio and A. Boies, *Environ. Sci.: Atmos.*, 2024, **4**(9), 1079–1090.
- C. Levesque, K. Casey and S. Beauchemin, *Aerosol Sci. Technol.*, 2025, **59**(11), 1371–1384.
- K. Vasilatou, K. Iida, M. Kazemimanesh, J. Olfert, H. Sakurai, T. A. Sipkens and G. J. Smallwood, *J. Aerosol Sci.*, 2025, **183**, 106483.
- S. L. Abram, I. Tavernaro, L. J. Johnston, S. Zou and U. Resch-Genger, *Anal. Bioanal. Chem.*, 2025, **417**(12), 2405–2425.
- T. D. Andron, W. T. Corns, M. A. Dexter, I. Zivkovic, J. Kotnik and M. Horvat, *Atmosphere*, 2025, **16**(4), 421.
- S. Page, P. J. H. Dunn, P. Petrov, S. V. Nair, I. Zivkovic, M. Horvat, W. T. Corns and H. Goenaga-Infante, *J. Anal. At. Spectrom.*, 2025, **40**(3), 785–794.
- M. Davis and J. Lu, *Crit. Rev. Anal. Chem.*, 2024, **54**(6), 1748–1757.
- Y. B. Zhao, T. L. Chen and J. Wang, *Atmos. Environ.*, 2025, **358**, 121343.
- A. M. Craze, C. Bartle and C. Roper, *J. Air Waste Manage. Assoc.*, 2025, **75**(1), 52–71.
- F. Bergman, A. C. Eriksson, M. Spanne, L. Ohlsson, I. Mahmutovic Persson, L. Uller, J. Rissler and C. Isaxon, *J. Aerosol Sci.*, 2024, **181**, 106416.
- J. R. Bacon, O. T. Butler, W. R. L. Cairns, O. Cavoura, J. M. Cook, C. M. Davidson and R. Mertz-Kraus, *J. Anal. At. Spectrom.*, 2023, **38**(1), 10–56.
- H. Y. Li, L. Mazzei, C. D. Wallis and A. S. Wexler, *Aerosol Air Qual. Res.*, 2024, **24**(10), 240117.
- Z. Sun, C. Yu, J. Feng, J. Zhu and Y. Liu, *J. Anal. At. Spectrom.*, 2024, **39**(5), 1212–1224.
- M. Nakazato and T. Hirata, *Anal. Sci.*, 2025, **41**(8), 1185–1201.
- A. J. Goodman, B. F. Benner and M. D. Montañó, *Environ. Sci.: Nano*, 2025, **12**(3), 1789–1800.
- M. I. Chronakis, B. Meermann and M. von der Au, *Anal. Bioanal. Chem.*, 2025, **417**(1), 7–13.
- T. E. Lockwood, L. Schlatt and D. Clases, *J. Anal. At. Spectrom.*, 2025, **40**(1), 130–136.
- R. L. B. Johnson, H. Karkee and A. Gundlach-Graham, *J. Anal. At. Spectrom.*, 2025, **40**(7), 1658–1665.
- C. Gómez-Pertusa, M. C. García-Poyo, G. Grindlay, R. Pedraza, A. Yañez and L. Gras, *Microchim. Acta*, 2025, **192**(5), 288.
- T. Zerdoner, J. Vidmar, B. Arah and T. Zuliani, *Analyst*, 2025, **150**(20), 4572–4585.
- C. Stephan, A. Hineman and R. Merrifield, *Spectroscopy*, 2024, **39**(7), 8–13.
- L. T. Chou, Y. P. Lin, C. H. Yu, J. F. Ye, W. C. Hou and T. C. Hsiao, *J. Hazard. Mater.*, 2025, **494**, 138711.
- T. Hirata, K. Kobayashi, H. H. Khoo, O. Shikino and H. Asanuma, *Analyst*, 2024, **149**(21), 5174–5183.
- A. Ganeev, V. Chuchina, A. Gubal, D. Kravtsov, E. Iakovleva, M. Yavor, A. Berdnikov, A. Frolov, M. Sillanpää, Q. Ye, J. Han, M. Myradimov and A. Stroganov, *Eur. J. Mass Spectrom.*, 2025, **31**(1–2), 3–20.



- 37 B. A. Nault, M. Canagaratna, P. Croteau, E. Fortner, A. T. Lambe, H. Stark, D. Sueper, B. S. Werden, A. Williams, L. R. Williams, D. Worsnop, J. Jayne, P. F. Decarlo, M. Cubison, G. Papadopoulos and R. Urs, *Aerosol Sci. Technol.*, 2025, **59**(6), 719–742.
- 38 M. A. R. Tawadrous, A. K. Y. Lee and A. W. H. Chan, *Aerosol Sci. Technol.*, 2025, **59**(6), 691–704.
- 39 L. Mărmureanu, C. A. Marin, J. Vasilescu, J.-E. Petit, T. Amodeo, F. Truong, B. Antonescu, M. C. Minguillon, D. C. Green, B. Zainab, J. Ovadnevaite, T. Elste, E. Coz, J. Allan, P. L. Croteau, J. Jayne, M. R. Canagaratna, L. Williams, V. Gros, A. S. H. Prevot, O. Favez and E. Freney, *Aerosol Sci. Technol.*, 2025, **59**(1), 16–33.
- 40 J. Ø. Halvorsen, P. Stacey, P. Graff, E. L. Folven Gjengedal and T. K. Ervik, *J. Occup. Environ. Hyg.*, 2025, **22**(4), 248–258.
- 41 I. Trebs, C. Lett, A. Krein, E. M. Kawaguchi and J. Junk, *Atmos. Meas. Tech.*, 2024, **17**(23), 6791–6805.
- 42 B. Wu, Z. Wu, J. Dou, Z. Yao, X. Shen, A. Wang, L. Li and X. Hao, *Sci. Total Environ.*, 2025, **958**, 177872.
- 43 A. K. Alang and S. G. Aggarwal, *Aerosol Air Qual. Res.*, 2024, **24**(9), 240035.
- 44 T. A. Sipkens, J. C. Corbin, B. Smith, S. Gagné, P. Lobo, B. T. Brem, M. P. Johnson and G. J. Smallwood, *Atmos. Meas. Tech.*, 2024, **17**(14), 4291–4302.
- 45 O. Butler and J. Forster, *Accredit. Qual. Assur.*, 2024, **29**(5), 391–395.
- 46 M. J. Haryanto, J. Zhang, S. Kagaya, K. Horikawa and M. S. Nahar, *Microchem. J.*, 2024, **206**, 111526.
- 47 R. Fernandes, R. Martins and C. Marques, *Anal. Methods*, 2025, **17**(7), 1415–1427.
- 48 A. Moteallehi, M. H. Dehghani, F. Momeniha and S. Azizi, *Microchem. J.*, 2024, **207**, 111884.
- 49 M. Vasudeva, A. K. Warriar, V. B. Kartha and V. K. Unnikrishnan, *TrAC, Trends Anal. Chem.*, 2025, **183**, 118111.
- 50 L. S. Kato, V. H. C. da Silva, D. C. de Andrade, G. Cruz, J. H. Pedrobom, A. Raab, J. Feldmann and M. A. Z. Arruda, *Anal. Chim. Acta*, 2024, **1331**, 343084.
- 51 H. Lu, J. Wang, C. Wei, J. B. Chao, T. Zhou and M. T. Zhao, *At. Spectrosc.*, 2024, **45**(5), 415–421.
- 52 D. Bartzak, S. C. Nunez, A. Kubicka, D. Ojeda, A. S. Cachero, S. Cowen, S. Ellison, G. Holcombe and H. Goenaga-Infante, *Anal. Bioanal. Chem.*, 2025, **417**(12), 2655–2667.
- 53 P. C. Gillemot, A. Kretschmer, R. Grimmig, U. E. A. Fittschen and S. Witzleben, *Anal. Chim. Acta*, 2025, **1362**, 344185.
- 54 S. Frassati, E. Barbaro, C. Rossetti, G. Cozzi, C. Turetta, F. Scoto, M. Roman, M. Feltracco, K. Kim, C. Barbante, A. Gambaro and A. Spolaor, *J. Anal. Sci. Technol.*, 2024, **15**(1), 49.
- 55 M. Athmer, A. M. Röhnelt, T. J. Maas, S. B. Haderlein and U. Karst, *J. Chromatogr.*, 2025, **1748**, 465843.
- 56 L. J. Chen, Y. Y. Du, S. Y. Li, X. Liu, J. Shen and Z. L. Zhu, *Anal. Chem.*, 2025, **97**(4), 2264–2272.
- 57 T. Narukawa, A. Wada, C. Cheong and K. Chiba, *Anal. Sci.*, 2024, **40**(12), 2279–2286.
- 58 R. Pechancová, R. da Silva, D. Milde and T. Pluháček, *Microchem. J.*, 2025, **212**, 113190.
- 59 F. Sandro, H. Bodo and G. Detlef, *J. Anal. At. Spectrom.*, 2025, **40**(1), 276–285.
- 60 L. Brunnbauer, L. Kronlachner, E. Foisner and A. Limbeck, *J. Anal. At. Spectrom.*, 2025, **40**(3), 753–761.
- 61 J. L. Tian, L. N. Zheng, Z. W. Meng, W. J. Wang, S. S. Liang, H. Fang, T. F. Zhang, B. Wang, M. Wang and W. Y. Feng, *J. Anal. At. Spectrom.*, 2025, **40**(7), 1718–1725.
- 62 B. T. Manard, V. C. Bradley, L. Hendriks, D. R. Dunlap, N. A. Zirakparvar, B. W. Ticknor, M. Toro-Gonzalez and H. B. Andrews, *Talanta*, 2025, **286**, 127516.
- 63 S. E. Szakas, J. S. Stanberry, N. A. Zirakparvar, H. B. Andrews, D. R. Dunlap, M. Darnell, B. W. Ticknor, L. R. Shultz-Johnson, S. K. Tazik and B. T. Manard, *J. Anal. At. Spectrom.*, 2025, **40**(6), 1483–1493.
- 64 A. Bazo, E. Bolea-Fernandez, A. Rua-Ibarz, M. Aramendia and M. Resano, *Anal. Chim. Acta*, 2024, **1331**, 343305.
- 65 M. Lomax-Vogt, L. M. Carter, J. Wielinski, S. Kutuzov, G. V. Lowry, R. Sullivan, P. Gabrielli and J. W. Olesik, *J. Anal. At. Spectrom.*, 2025, **40**(3), 848–859.
- 66 A. S. Priede, M. Corte-Rodríguez, H. Gödde, M. M. Bayón and J. Bettmer, *Talanta*, 2025, **295**, 128372.
- 67 J. H. Dong, Z. L. Zhu, L. J. Li, P. J. Xing, S. Y. Li, L. Ouyang, X. Liu, W. Guo, H. T. Zheng and R. Qian, *J. Anal. At. Spectrom.*, 2024, **39**(11), 2791–2798.
- 68 K. Li, W. Zeng, C. H. Li, X. M. Jiang and X. D. Hou, *Anal. Chem.*, 2025, **97**(10), 5439–5444.
- 69 F. Xu, Y. Liu, X. Liu, J. Tan, H. Xia and M. Li, *Microchem. J.*, 2023, **193**, 109109.
- 70 Z. X. Liu, Y. B. Su, Y. Y. Liu, J. Y. Zhang and C. B. Zheng, *At. Spectrosc.*, 2025, **46**(1), 1–9.
- 71 C. H. Kuo and C. K. Su, *Anal. Chim. Acta*, 2025, **1336**, 343536.
- 72 R. Tong, H. T. Li, W. Guo, C. X. Zhang, Q. H. Xu, L. L. Jin and S. H. Hu, *At. Spectrosc.*, 2024, **45**(2), 144–149.
- 73 M. Harhash, J. G. Wiederhold, I. Nett, J. Arndt, A. Zavarsky, T. A. Ternes and L. Duester, *Environ. Sci. Eur.*, 2025, **37**(1), 89.
- 74 B. Hattendorf, T. Renevey and D. Gunther, *Anal. Chem.*, 2025, **97**(11), 5926–5931.
- 75 W. R. L. Cairns, O. T. Butler, O. Cavoura, C. M. Davidson, J. L. Todolí-Torró and M. von der Au, *J. Anal. At. Spectrom.*, 2025, **40**(1), 11–69.
- 76 K. P. Hobbs, A. D. French, S. R. Scott, M. A. Risenhuber, M. M. Haney, I. J. Arnquist, S. M. Herman and C. L. Beck, *Talanta*, 2025, **287**, 127666.
- 77 A. D. French, K. P. Hobbs, R. M. Cox and I. J. Arnquist, *Analyst*, 2024, **149**(24), 5812–5820.
- 78 T. D. Schlieder, N. D. Rocco, M. L. di Vacri, I. J. Arnquist, D. Bottenus, Z. Huber and B. McNamara, *J. Anal. At. Spectrom.*, 2024, **39**(10), 2502–2507.
- 79 D. Y. Li, G. H. Cui, S. S. Chen, Y. F. Qiao, Q. Liu, J. Zhang and Q. He, *J. Anal. At. Spectrom.*, 2024, **39**(10), 2395–2401.
- 80 B. Wiggershaus, E. Franke and C. Vogt, *X-Ray Spectrom.*, 2025, **54**(2), 193–202.



- 81 Q. Y. Wang, X. Gao, Z. Y. Wang, Y. Cui, A. M. Chen and X. Y. Han, *J. Anal. At. Spectrom.*, 2025, **40**(5), 1411–1418.
- 82 G. Kajner and G. Galbács, *Anal. Chem.*, 2025, **97**(23), 12000–12004.
- 83 H. J. Zhang, Y. Chen, Z. J. Bi, X. H. Che and Z. S. Tian, *Photonics*, 2025, **12**(6), 616.
- 84 Y. T. Chen, S. J. Guo, Y. F. Jiang, A. M. Chen and M. X. Jin, *Talanta*, 2025, **286**, 127512.
- 85 Y. W. Xiong, W. H. Huang, J. H. Yang, J. F. Nie and L. B. Guo, *J. Anal. At. Spectrom.*, 2025, **40**(2), 503–512.
- 86 Y. K. Tanaka, K. Matsushashi and Y. Ogra, *Anal. Sci.*, 2025, **41**(4), 317–321.
- 87 S. W. C. Chung, *Food Addit. Contam., Part A*, 2025, **42**(3), 342–358.
- 88 P. Sharma, J. Govindaraj, C. Poulin-Ponnelle and D. Lariviere, *Microchem. J.*, 2025, **212**, 113099.
- 89 P. Wang, Y. J. Zou, H. Ren, A. Zhang, Y. Y. Cao and L. Xu, *Environ. Technol. Innovation*, 2025, **38**, 104152.
- 90 A. H. Chaudhry, S. A. A. Zaidi, S. Ali, M. Imran, N. Sial, N. Iqbal, S. K. Wahla, F. Qurban, M. Aslam and M. Ajmal, *Rev. Anal. Chem.*, 2025, **44**(1), 20230082.
- 91 T. M. Mogashane, O. Mapazi, M. A. Motlatle, L. Mokoena and J. Tshilongo, *Molecules*, 2025, **30**(5), 1001.
- 92 X. Yu, X. B. Su, Z. Wang, Z. Y. Hou and B. P. Li, *Anal. Methods*, 2025, **17**(8), 1683–1697.
- 93 H. Ren, Y. H. Li, L. Xu, P. Wang and Y. Y. Cao, *Environ. Technol. Innovation*, 2025, **38**, 104146.
- 94 S. L. C. Ferreira, L. S. G. Teixeira, W. Q. Ferreira, S. V. A. Dantas, A. S. Lima, M. G. A. Korn, F. A. S. Cunha, V. Cerda, W. N. L. dos Santos, J. B. da Silva Jr. and O. M. C. Oliveira, *TrAC, Trends Anal. Chem.*, 2024, **181**, 118055.
- 95 W. H. Li, Y. Tan, G. J. Shang, L. Q. Chen, Z. B. Wu, Y. Q. Lin, L. Luo and Y. Yang, *J. Environ. Chem. Eng.*, 2024, **12**(6), 114748.
- 96 S. A. Wise, S. H. Coskun, H. V. Hayes, W. B. Wilson, J. A. Murray, J. A. Lippert, C. Q. Burdette, M. M. Schantz, K. E. Murphy, S. J. Christopher, L. L. Yu, C. A. Rimmer, S. M. Pasiakos and A. J. Kuszak, *Anal. Bioanal. Chem.*, 2025, **417**(12), 2439–2471.
- 97 J. F. Sam, A. J. Kuszak, P. J. Gray and S. A. Wise, *J. AOAC Int.*, 2024, **107**(6), 1027–1037.
- 98 J. Wu, Y. An, X. Li, F. Liu, J. Xu, M. Ling and Z. Zhang, *Geostand. Geoanal. Res.*, 2024, **49**(1), 233–244.
- 99 C. Park, K. Ra and H. Jeong, *J. Anal. At. Spectrom.*, 2025, **40**(4), 1058–1068.
- 100 M. A. Gürbüz, *J. Soil Sci. Plant Nutr.*, 2025, **25**(2), 4669–4686.
- 101 A. R. López, E. Ortega-Caneda, E. Espada-Bellido, O. R. Taracena-Zepeda, M. Palma and G. Fernández-Barbero, *Foods*, 2024, **13**(24), 4051.
- 102 K. Giacobe, D. P. de Almeida, S. R. Waechter, F. A. Duarte and C. A. Duarte, *Braz. J. Anal. Chem.*, 2024, **11**(44), 118–130.
- 103 S. S. Zhang, B. Y. Chen, Y. Liu, H. Y. Sun, H. X. Zhang, N. Li, Y. Qing, J. Elango, D. Y. Zhao and W. H. Wu, *Foods*, 2025, **14**(3), 384.
- 104 S. S. Ferreira, R. S. Lamarca, L. S. Silva, T. A. L. Burgo, P. Gomes, C. D. B. Amaral, J. O. Fernandes, S. C. Cunha and M. H. Gonzalez, *ACS Omega*, 2025, **10**(24), 26118–26128.
- 105 G. A. Biltekin, A. Akdogan and Ü. Divrikli, *J. Food Meas. Charact.*, 2025, **19**(1), 401–411.
- 106 N. Vaezi and N. Dalali, *J. Dispersion Sci. Technol.*, 2024, 1–15.
- 107 X. J. Chen, Q. C. Xu, L. Yan, X. D. Hao, X. C. Guan, X. P. Han, A. D. Sun, Z. Q. Chen, L. H. Liu and Z. H. Zhu, *J. Anal. At. Spectrom.*, 2024, **39**(12), 3162–3170.
- 108 A. Sun, D. Gou, Y. Dong, Q. Xu and G. Cao, *J. Agric. Food Chem.*, 2019, **67**(25), 7183–7189.
- 109 Y. R. Wu, G. L. Liu, X. Q. Liu, Y. X. Mao, Y. Y. Guo, Y. W. Liu, L. C. Zhu, Y. G. Yin, Y. Cai and G. B. Jiang, *Water Res.*, 2024, **263**, 122167.
- 110 D. J. Butcher, *Appl. Spectrosc. Rev.*, 2024, **60**(5), 431–449.
- 111 O. Zverina, L. Bruhova, P. Coufalik, C. D. Stringer, J. Rieger and W. Goessler, *Spectrochim. Acta, Part B*, 2024, **218**, 106979.
- 112 B. D. Szeredai, T. Frentiu, N. Muntean, A. I. Dudu and E. Covaci, *J. Anal. At. Spectrom.*, 2025, **40**(4), 942–953.
- 113 O. V. Shuvaeva, I. A. Bekesha and D. Y. Troitskii, *Microchem. J.*, 2024, **207**, 111755.
- 114 G. Y. Lan, L. Chen, J. W. Guo, Y. Xu, X. Li, Y. B. Li, L. C. Liu, L. Feng, X. J. Xi and X. Mao, *At. Spectrosc.*, 2024, **45**(6), 516–524.
- 115 C. Tobias, L. Gehrenkemper, T. Bernstein, S. Schlau, F. Simon, M. Röllig, B. Meermann and M. von der Au, *Anal. Chim. Acta*, 2025, **1335**, 343460.
- 116 X. N. Liu, X. A. Yang, X. F. Chu and W. B. Zhang, *Talanta*, 2025, **285**, 127324.
- 117 M. I. Chronakis, B. Meermann and M. von der Au, *Anal. Bioanal. Chem.*, 2025, **417**(1), 7–13.
- 118 O. N. Grebneva-Balyuk, M. S. Kiseleva and I. V. Kubrakova, *J. Anal. Chem.*, 2025, **80**(4), 608–622.
- 119 T. Xu, X. W. Tian, Y. W. Liu, Y. Y. Guo, L. G. Hu, Y. G. Yin, Q. H. Zhang, Y. Cai and G. B. Jiang, *Chin. J. Anal. Chem.*, 2024, **52**(10), 1403–1412.
- 120 M. Vats, B. Cillero-Pastor, E. Cuypers and R. M. A. Heeren, *Analyst*, 2024, **149**(18), 4553–4582.
- 121 Y. R. Duan, Z. R. Wang, W. X. Gou, Z. Wang, Q. G. Li and W. Li, *Earth-Sci. Rev.*, 2025, **269**, 105185.
- 122 Y. B. Zhu, G. S. Yang, A. Sakaguchi, T. Miura, Y. Shikamori and J. Zheng, *J. Anal. At. Spectrom.*, 2025, **40**(6), 1428–1446.
- 123 G. R. Bitencourt, P. A. Mello, P. Grinberg and R. E. Sturgeon, *J. Anal. At. Spectrom.*, 2025, **40**, 1754–1766.
- 124 N. Q. Thang, H. K. Trung, L. V. Tan, N. T. K. Phuong, N. T. K. Ngan and T. Q. Hieu, *J. Anal. Chem.*, 2025, **80**(5), 877–886.
- 125 H. C. Xu, Y. W. Zhu, Y. Peng, C. C. Sun, F. F. Fu and Y. Lin, *J. Anal. At. Spectrom.*, 2025, **40**(5), 1364–1372.
- 126 A. Izdebska, S. Budzynska and K. Bierla, *Molecules*, 2024, **29**(13), 3055.
- 127 X. X. Zhou, Q. Z. Xiao, K. N. Zhang, Y. Gao, J. Zhang, L. P. Fang, B. Yan and F. B. Li, *Anal. Chem.*, 2024, **96**(42), 16937–16945.



- 128 A. C. V. Rubin, V. M. Neves, A. B. Viana, T. B. Riquieri, D. Pozebon and V. L. Dressler, *Quim. Nova*, 2025, **48**(2), e20250078.
- 129 Y. H. Huang, Z. J. Jia, H. Xu, K. Kreissig, B. J. Coles, M. Rehkämper and R. E. T. Moore, *Talanta*, 2025, **285**, 127296.
- 130 X. Wu, Z. Y. Wang, G. Y. Sun, Y. Lin, X. W. Fu, Y. Tang and X. B. Feng, *J. Anal. At. Spectrom.*, 2024, **39**(9), 2298–2308.
- 131 H. G. Zhu, J. M. Zhu, D. C. Tan, Z. Lu, H. F. Liao and Y. W. Ma, *J. Anal. At. Spectrom.*, 2024, **39**(12), 3082–3093.
- 132 S. Singh, M. R. Mucalo and M. N. C. Grainger, *Talanta*, 2025, **281**, 126797.
- 133 B. Jiang, X. R. Zhou, W. Xie and B. Y. Ni, *Anal. Bioanal. Chem.*, 2025, **417**(20), 4617–4626.
- 134 T. D. Schlieder, K. P. Hobbs, A. D. French, L. H. Hughes, I. J. Arnquist and C. Beck, *Anal. Chem.*, 2025, **97**(23), 12313–12320.
- 135 X. Zhou, Q. Xiao, Y. Deng, X. Hou, L. Fang, Y. Zhou and F. Li, *Sci. Total Environ.*, 2024, **947**, 174621.
- 136 B. M. Freire, A. Rua-Ibarz, F. V. Nakadi, E. Bolea-Fernandez, J. J. Barriuso-Vargas, C. N. Lange, M. Aramendia, B. L. Batista and M. Resano, *Talanta*, 2024, **277**, 126417.
- 137 J. Feldmann, H. R. Hansen, T. M. Karlsson and J. H. Christensen, *Environ. Sci. Technol.*, 2024, **58**(29), 12755–12762.
- 138 G. S. Zhao, L. Huang, L. F. Liu, B. Jia, L. Xu, H. Zhu and P. Cheng, *Talanta*, 2025, **282**, 127075.
- 139 T. Shi, Z. B. Zhou, Z. Y. Tang, Y. Guo, D. B. Wu, L. Wang and C. B. Leng, *Talanta*, 2024, **279**, 126539.
- 140 Y. Guo, T. Shi, D. B. Wu, L. Wang, H. Y. Guo, W. Liu and C. B. Leng, *J. Anal. At. Spectrom.*, 2025, **40**(8), 1946–1953.
- 141 D. S. Ferreira, D. V. Babos, M. H. Lima, H. F. Castello, A. C. Olivieri, F. M. V. Pereira and E. R. Pereira, *J. Anal. At. Spectrom.*, 2024, **39**(12), 2949–2973.
- 142 S. C. Yao, Z. Y. Yu, Z. Y. Hou, L. B. Guo, L. Zhang, H. B. Ding, Y. Lu, Q. Q. Wang and Z. Wang, *TrAC, Trends Anal. Chem.*, 2024, **177**, 117795.
- 143 M. Rizwan, M. S. Afgan, S. Saleem, K. K. Kou, Z. Y. Hou and Z. Wang, *Spectrochim. Acta, Part B*, 2025, **227**, 107168.
- 144 S. Y. Zhao, Y. C. Zhao, Y. J. Dai, Z. Y. Liu, Z. Y. Hou, X. Gao and Z. Wang, *J. Anal. At. Spectrom.*, 2025, **40**(3), 665–678.
- 145 X. L. Li, R. Q. Chen, F. Liu, Z. K. You, J. Huang, J. Y. Peng and G. Li, *Comput. Electron. Agric.*, 2025, **229**, 109831.
- 146 S. F. Li, Q. Zheng, X. D. Liu, P. Liu and L. Yu, *Molecules*, 2024, **29**(15), 3699.
- 147 Z. H. Yang, M. Y. Pang, J. C. Ma, Y. R. Zhao, K. Q. Yu and Y. He, *J. Anal. At. Spectrom.*, 2024, **39**(12), 3094–3105.
- 148 H. W. Duan, S. J. Zhao, M. Guo, Q. J. Niu, J. Huang and F. Liu, *Spectrosc. Spectr. Anal.*, 2025, **45**(4), 980–985.
- 149 Y. J. Gou, X. L. Fu, J. Zhang, J. Y. Jiang, Y. H. Huang, S. X. Ma, C. J. Zhao and G. L. Li, *J. Hazard. Mater.*, 2025, **487**, 137291.
- 150 A. Z. Li, X. Chuai, Y. X. Liu, L. R. Qiu, H. Cui and W. Q. Zhao, *Spectrochim. Acta, Part B*, 2024, **216**, 106931.
- 151 K. Keerthi, M. M. Antony and M. V. Matham, *Chem. Biol. Technol. Agric.*, 2024, **11**(1), 138.
- 152 W. N. Guedes, D. V. Babos, V. S. Freitas, D. K. Neiva, D. de Souza, L. Martin-Neto, D. M. B. P. Milori and P. R. Villas-Boas, *At. Spectrosc.*, 2025, **46**(2), 141–149.
- 153 P. Lin, C. B. Song, C. S. Yang, M. J. Zhang, S. X. Ma, J. T. Wen, D. M. Dong and Y. X. Han, *Comput. Electron. Agric.*, 2024, **226**, 109396.
- 154 F. H. Qu, H. C. Li, Q. F. Sun, W. X. Li, Y. C. Fu, M. Z. Huang and T. Y. Liu, *J. Anal. At. Spectrom.*, 2024, **39**(10), 2514–2521.
- 155 V. S. Kumar and M. Thangaraja, *Appl. Phys. A: Mater. Sci. Process.*, 2025, **131**(7), 553.
- 156 B. Lu, X. Wang, C. Hu and X. Li, *Agriculture*, 2024, **14**(6), 946.
- 157 W. P. Xie, J. Xu, L. Huang, Y. Xu, Q. Wan, Y. F. Chen and M. Y. Yao, *Agriculture*, 2024, **14**(11), 2053.
- 158 J. Y. Peng, L. F. Ye, Y. F. Liu, F. Zhou, L. J. Xu, F. L. Zhu, J. Huang and F. Liu, *Spectrochim. Acta, Part B*, 2024, **222**, 107072.
- 159 A. Wangeci, M. Knadel, O. De Pascale, M. H. Greve and G. S. Senesi, *J. Anal. At. Spectrom.*, 2024, **39**(11), 2903–2916.
- 160 L. Wang, T. Galina, L. K. Jing, L. Xu, Y. X. Fu, H. Gao and L. Li, *J. Anal. At. Spectrom.*, 2025, **40**(6), 1526–1535.
- 161 J. Z. Cai, T. Z. Wu, Y. Chen, S. Y. Yang, Z. R. Zhang and Y. Z. Liu, *J. Laser Appl.*, 2024, **36**(3), 032027.
- 162 C. Vanhoof, J. R. Bacon, U. E. A. Fittschen and L. Vincze, *J. Anal. At. Spectrom.*, 2024, **39**(9), 2152–2164.
- 163 P. Ashe, K. Y. Tu, J. A. Stobbs, J. J. Dynes, M. Vu, H. Shaterian, S. Kagale, K. K. Tanino, J. P. D. Wanasundara, S. Vail, C. Karunakaran and T. D. Quilichini, *Front. Plant Sci.*, 2025, **15**, 1395952.
- 164 X. Chen, S. X. Wang, M. H. Zhou, J. J. Wang, W. Song, J. Q. Zhang, Y. Wang, W. Tian and Y. X. Wu, *Talanta*, 2025, **288**, 127719.
- 165 Y. Wang, T. Gan, N. Zhao, G. Yin, T. Li, X. Li and X. Tan, *Anal. Methods*, 2025, **17**(25), 5186–5202.
- 166 Z. Q. Ye, T. T. Gan, N. J. Zhao, G. F. Yin, R. Y. Sheng, Y. Wang and T. H. Li, *X-Ray Spectrom.*, 2025, **54**(5), 506–516.
- 167 I. Purwadi, P. D. Erskine, L. W. Casey and A. van Der Ent, *Ecol. Res.*, 2024, DOI: [10.1111/1440-1703.12501](https://doi.org/10.1111/1440-1703.12501).
- 168 E. Chatzitheodoridis, C. D. Georgiou, M. Ferus, E. Kalaitzopoulou, H. A. Stavrakakis, I. Markopoulos and M. Holynska, *Adv. Space Res.*, 2024, **74**(7), 3407–3436.
- 169 M. Schindler, M. A. Alavijeh, M. L. S. Oliveira and L. F. O. Silva, *Geostand. Geoanal. Res.*, 2025, **49**(1), 133–159.
- 170 A. R. Cardoso, J. S. Schmidt, A. J. Maraschin, D. C. de Andrade, F. M. de Albano, E. M. Bernardes, G. Ruebensam, G. B. Barp, N. P. Rodrigues, Y. F. de Oliveira, J. C. Vazquez and F. D. Vecchia, *Geostand. Geoanal. Res.*, 2025, **49**(1), 161–177.
- 171 D. Y. Peng, Z. Bao, L. Kang, P. Liu, C. L. Zong, K. Y. Chen and H. L. Yuan, *At. Spectrosc.*, 2024, **45**(6), 498–507.
- 172 X. L. Zeng, M. Li, H. Y. Jin, Z. W. Cao, D. T. He, Z. C. Hu, Y. S. Liu and X. N. Chai, *At. Spectrosc.*, 2024, **45**(6), 532–540.
- 173 D. Peng, Z. Bao, K. Chen, N. Lv, X. Nie, J. Tian and H. Yuan, *J. Anal. At. Spectrom.*, 2024, **39**(9), 2235–2244.
- 174 Z.-H. Dai, P. Liao, D.-J. Wang, S. Lin, H.-P. Li, Z.-A. Bao, K.-J. Hou, L.-M. Chen, T.-G. Lan and C. Cui, *J. Anal. At. Spectrom.*, 2024, **39**(9), 2309–2318.



- 175 D. Y. Peng, Z. Bao, L. Kang, X. J. Nie, K. Y. Chen, Y. Zhang and H. L. Yuan, *Microchem. J.*, 2025, **212**, 113238.
- 176 S. W. Raja, R. Acharya, A. D. Sonawane, T. S. R. C. Murthy and S. Majumdar, *J. Anal. At. Spectrom.*, 2024, **39**(9), 2278–2289.
- 177 S. Balachandar, W. Zhang, Y. S. Liu, Z. C. Hu, H. H. Chen, T. Luo, T. He and X. L. Zeng, *J. Anal. At. Spectrom.*, 2025, **40**(1), 259–275.
- 178 Y. Moussallam, W. H. Towbin, T. Plank, H. Bureau, H. Khodja, Y. Guan, C. Ma, M. B. Baker, E. M. Stolper, F. U. Naab, B. D. Monteleone, G. A. Gaetani, K. Shimizu, T. Ushikubo, H. J. Lee, S. Ding, S. Shi and E. F. Rose-Koga, *Geostand. Geoanal. Res.*, 2024, **48**(3), 637–660.
- 179 T. Luo, M. F. Li, X. D. Deng, J. R. Tu, H. T. Shen, T. Kapitany, B. N. Hu, W. Zhang and Z. C. Hu, *Chem. Geol.*, 2025, **674**, 122562.
- 180 N. Sharp, M. V. Martinez, R. Corzo, B. Toman, R. Paul, S. Rabb, J. Prothero and J. L. Weaver, *Geostand. Geoanal. Res.*, 2025, **49**(4), 781–798.
- 181 P. Robinson, *Geostand. Geoanal. Res.*, 2025, **49**(1), 9–50.
- 182 D. S. Xue, S. Guo, Y. H. Liu, D. P. Zhang, D. Zhang, X. G. Li and S. K. Liu, *Anal. Chim. Acta*, 2025, **1345**, 343732.
- 183 L. J. Gao, D. Y. Sun, X. Y. Wang, D. Chen, Z. D. Tian, A. B. Luo and R. S. Yin, *Anal. Chem.*, 2024, **96**(44), 17560–17566.
- 184 S. J. Akinbodunse, K. Ufer, R. Dohrmann and C. Mikutta, *Am. Mineral.*, 2024, **109**(12), 2037–2051.
- 185 R. S. Harmon and G. S. Senesi, *Geostand. Geoanal. Res.*, 2024, **48**(4), 763–792.
- 186 R. S. Harmon, *Minerals*, 2024, **14**(7), 731.
- 187 J. J. Yan, J. X. Ma, K. Liu, Y. Li and K. L. Li, *J. Anal. At. Spectrom.*, 2025, **40**(6), 1447–1468.
- 188 H. Saeidfirozeh, P. Kubelik, V. Laitl, A. Krivková, J. Vrabec, K. Rammelkamp, S. Schröder, I. B. Gornushkin, E. Kepes, J. Zabka, M. Ferus, P. Porizka and J. Kaiser, *TrAC, Trends Anal. Chem.*, 2024, **181**, 117991.
- 189 S. Selmani, I. Elhamdaoui, P. Bouchard, M. Constantin, M. Sabsabi and F. Vidal, *At. Spectrosc.*, 2025, **46**(2), 109–118.
- 190 J. X. Ji, Z. Y. Hou, W. L. Gu, X. Yu and Z. Wang, *Anal. Chim. Acta*, 2025, **1359**, 344125.
- 191 M. Bosáková, K. Novotny, J. Moros and J. Laserna, *Spectrochim. Acta, Part B*, 2025, **226**, 107140.
- 192 D. Díaz Pace, A. Caggianelli, O. De Pascale and G. S. Senesi, *Minerals*, 2024, **14**(12), 1257.
- 193 Y. T. Fu, J. Chen, B. Y. Liu, B. B. Hu, X. Y. Jin, G. Yang and H. H. Sun, *J. Anal. At. Spectrom.*, 2025, **40**(3), 715–726.
- 194 G. S. Senesi, O. De Pascale, S. Mattiello, V. Moggi Cecchi, A. Ibhi, L. Ouknine and H. Nachit, *Geostand. Geoanal. Res.*, 2024, **48**(4), 837–862.
- 195 T. Lopes, R. Cavaco, D. Capela, F. Dias, J. Teixeira, C. S. Monteiro, A. Lima, D. Guimaraes, P. A. S. Jorge and N. A. Silva, *Talanta*, 2025, **283**, 127110.
- 196 Y. Li, M. J. Shan, Y. H. Wang, J. J. Cong, L. Y. Ding, J. J. Lin, M. C. Cui and N. Ma, *J. Anal. At. Spectrom.*, 2025, **40**(8), 1995–2005.
- 197 S. Saha, J. Sanwal, P. Mahadik, P. Sengupta and P. Mathi, *Microchem. J.*, 2024, **207**, 112215.
- 198 X. L. Liu, S. C. Ren, M. Zhang, L. L. Peng, Y. Zhang, X. T. Meng, S. J. Wu, Y. H. Li, L. Liu and S. H. Sun, *J. Anal. At. Spectrom.*, 2025, **40**(2), 437–446.
- 199 C. Burgos-Palop, F. J. Fortes, P. Purohit, T. Delgado and J. Laserna, *Anal. Chim. Acta*, 2024, **1332**, 343361.
- 200 J. B. Cai, M. R. Dong, H. J. Chen, Z. H. Shang, S. C. Yao and J. D. Lu, *At. Spectrosc.*, 2024, **45**(3), 200–208.
- 201 M. D. Dyar, C. R. Ytsma and K. Lepore, *Earth Space Sci.*, 2024, **11**(10), e2024EA003635.
- 202 K. H. Lepore, I. Belkhdja, M. D. Dyar and C. R. Ytsma, *Spectrochim. Acta, Part B*, 2024, **217**, 106970.
- 203 H. F. Zeng, S. C. Liu, Z. X. Zhang, X. F. Liu, X. H. Tong, H. Xie, K. C. Du and J. Zhang, *IEEE Trans. Geosci. Remote Sens.*, 2024, **62**, 4601311.
- 204 S. Singhal, S. Singh and D. Singh, *J. Mass Spectrom.*, 2025, **60**(3), e5115.
- 205 A. C. Humbert, F. Pointurier and A. Hubert, *J. Anal. At. Spectrom.*, 2024, **39**(12), 3180–3189.
- 206 X. Yang, S. X. Gao, D. Wang, X. F. Qiu, X. R. Tong, D. Y. Ju and Z. F. Zhang, *At. Spectrosc.*, 2024, **45**(5), 422–437.
- 207 C. Kooymans, C. W. Magee Jr, K. Waltenberg, N. J. Evans, S. Bodorkos, Y. Amelin, S. L. Kamo and T. Ireland, *Geochronology*, 2024, **6**(3), 337–363.
- 208 J. Hu, Z. W. Li, J. X. Li, S. G. Liu, G. Q. Xu, C. Q. Yang, K. Tong and Y. Li, *J. Anal. At. Spectrom.*, 2024, **39**(11), 2856–2869.
- 209 A. H. Laskar, P. Nayak, A. Singh, R. K. Agrawal, R. K. Mohanty, M. S. Shah and M. G. Yadava, *Nucl. Instrum. Methods Phys. Res., Sect. B*, 2025, **563**, 165698.
- 210 K. L. Linge, *Geostand. Geoanal. Res.*, 2024, **48**(3), 543–575.
- 211 J. T. Kang, X. Q. Chen, X. Deng, Y. Fang, H. C. Jiang, C. Y. H. Liu, C. H. Luo, X. Li, Y. C. Lin, Z. Q. Ren, J. R. Sheng, X. Tang, L. Y. Xu, J. Y. Yan, Y. Q. Zhang, Z. Y. Hou, F. Wu, H. M. Yu and F. Huang, *J. Earth Sci.*, 2025, **36**(4), 1408–1424.
- 212 K. M. M. Shaw, M. Pfeifer, B. L. L. Coath, J. Lewis, D. Bevan, C. D. Coath and T. Elliott, *J. Anal. At. Spectrom.*, 2025, **40**(6), 1566–1579.
- 213 J. H. Dong, Y. Yu, Z. J. Dai, S. Y. Li, L. J. Chen, P. J. Xing, G. Wang, X. Liu, H. T. Zheng and Z. L. Zhu, *Anal. Chem.*, 2024, **96**(50), 19955–19964.
- 214 Y. Hu, Z. C. Hu and W. Zhang, *Anal. Chem.*, 2025, **97**(4), 2486–2493.
- 215 C. D. Standish, J. A. Milton, T. M. Page, R. M. Brown, D. Douglas, B. Paul, L. Schlatt and G. L. Foster, *Chem. Geol.*, 2024, **670**, 122438.
- 216 X. Wang, X. Liu, L. L. Jin, Z. L. Zhu, J. H. Dong, P. J. Xing, L. J. Chen, Y. H. Geng, J. W. Zhang, H. Tong, H. T. Zheng, M. Zhang and S. H. Hu, *J. Anal. At. Spectrom.*, 2024, **39**(12), 3198–3206.
- 217 E. Dubinina, A. Borisov, A. Gurenko, S. A. Kossova and A. S. Avdeenko, *Geostand. Geoanal. Res.*, 2025, **49**(3), 629–644.
- 218 C. Jones and D. A. Fike, *Geostand. Geoanal. Res.*, 2024, **48**(3), 613–618.



- 219 Y. L. Hu, W. Wang, X. Y. Zhao, C. G. Guan, C. M. Zhou, C. R. Song, H. Y. Shi, Y. P. Sun, Z. Chen and X. L. Yuan, *Mar. Pet. Geol.*, 2025, **171**, 107201.
- 220 K. Sasaki, A. Ishida, K. Sugitani and N. Takahata, *Chem. Geol.*, 2025, **683**, 122770.
- 221 Y. W. Chen, J. F. Gao, X. W. Bi, S. H. Dong, Q. L. Lei and R. Z. Hu, *J. Anal. At. Spectrom.*, 2024, **39**, 3000–3009.
- 222 J. L. Hao, H. C. Tian, C. Qi, R. Y. Li, S. Hu, Y. T. Lin, Y. S. He and W. Yang, *Talanta*, 2025, **289**, 127733.
- 223 J. Shea, E. Hughes, R. Balzer, I. Bindeman, J. Blundy, R. Brooker, R. Botcharnikov, P. Cartigny, G. Gaetani, G. Kilgour, J. Maclennan, B. Monteleone, D. A. Neave, O. Shorttle and EIMF, *Geostand. Geoanal. Res.*, 2025, **49**(3), 607–627.
- 224 R. C. Li, J. Y. Yan, J. W. Yu, X. L. Wang, T. Yang, S. P. Qian, C. M. Wang and H. Y. Xian, *J. Anal. At. Spectrom.*, 2025, **40**(3), 775–784.
- 225 P. J. Adeti, J. B. Tandoh, G. Owiredu, H. Ahiamadjie, R. A. T. Annan, E. J. Aniabo, G. E. Fianoo, S. Akoto Bamford and G. Amoako, *Cogent Eng.*, 2024, **11**(1), 2356168.
- 226 A. K. Maurya, P. D. Barman, A. Kumar, U. Yadav and A. K. Pandey, *X-Ray Spectrom.*, 2025, **54**(4), 352–358.
- 227 A. N. Zhilicheva, G. V. Pashkova, V. M. Chubarov, A. S. Maltsev, D. Kirsanov and V. Panchuk, *Spectrochim. Acta, Part B*, 2024, **222**, 107070.
- 228 C. H. Yi, C. A. Peters, V. Nikitin, S. S. Lee and P. Fenter, *Comput. Geosci.*, 2025, **196**, 105858.
- 229 Z. D. Zhang, J. X. Li, R. Gao, Y. Zhao, Y. Zhang, L. Zhang, Z. F. Ye, Z. J. Zhu, P. H. Zhang, W. B. Yin and S. T. Jia, *J. Anal. At. Spectrom.*, 2024, **39**(10), 2433–2442.
- 230 R. Gao, J. X. Li, H. Z. Han, J. C. Song, J. Y. Huo, L. Dong, W. G. Ma, S. Q. Wang, Y. Zhang, L. Zhang, P. H. Zhang, Z. F. Ye, Z. J. Zhu, Y. Zhao, W. B. Yin and S. T. Jia, *J. Anal. At. Spectrom.*, 2025, **40**(4), 1069–1085.
- 231 F. Förste, L. Bauer, Y. Wagener, F. Hilgerdenaar, F. Möller, B. Kanngiesser and I. Mantouvalou, *Anal. Chem.*, 2025, **97**(13), 7177–7185.
- 232 A. A. Al-Tameemi, F. S. Li, Q. L. Zhang, Z. N. Xiao, W. Q. Yang and S. Lyu, *J. Anal. At. Spectrom.*, 2025, **40**(6), 1580–1590.
- 233 J. Baek, S. Cho and S. Shin, *Environ. Earth Sci.*, 2025, **84**(13), 368.
- 234 R. Alonso-Perez, A. H. Rios, D. Gray, M. A. Palacios and A. McClelland, *J. Raman Spectrosc.*, 2025, **84**, 368.
- 235 D. Käser, R. Kägi, B. Hattendorf and D. Günther, *J. Anal. At. Spectrom.*, 2024, **39**(12), 3069–3081.
- 236 X. L. Yuan, X. P. Shen, L. B. Y. Liu, F. T. Li, L. L. Jiang, L. H. Zhai, H. Deng, L. X. Yan and Z. M. Li, *Int. J. Mass Spectrom.*, 2025, **510**, 117408.
- 237 C. F. Li, Z. Y. Chu and P. Peng, *Anal. Chem.*, 2024, **96**(38), 15436–15445.
- 238 S. Bowden, K. M. Samperton, E. D. LaBone, H. B. Lawton, A. M. Waldron, J. M. Mannion, M. S. Wellons and D. R. Mannion, *J. Anal. At. Spectrom.*, 2025, **40**(1), 195–201.
- 239 Y. X. Li, H. Y. Shi, P. Wang and Y. X. Mo, *J. Anal. At. Spectrom.*, 2025, **40**(7), 1833–1844.
- 240 S. Kim, S. T. Kim and M. Knyf, *Rapid Commun. Mass Spectrom.*, 2025, **39**(5), e9958.
- 241 J. Chaillot, S. Kassi, T. Clauzel, M. Pesnin, M. Casado, A. Landais and M. Daëron, *Chem. Geol.*, 2025, **673**, 122450.
- 242 S. J. McKibbin, J. N. Avila, T. R. Ireland, M. Van Ginneken, B. Soens, F. Van Maldeghem, M. Huber, L. Baeza, A. Patkar, F. Vanhaecke, V. Debaille, P. Claeys and S. Goderis, *Rapid Commun. Mass Spectrom.*, 2025, **39**(1), e9921.
- 243 D. Morcillo, A. Winckelmann, D. A. Frick, L. Jacobsen, T. Seger, S. Florek, S. Richter, J. Vogl, S. Recknagel, U. Panne and C. Adab, *Spectrochim. Acta, Part B*, 2024, **220**, 107013.
- 244 H. M. Hamed, M. Soliman, F. S. Abdou, S. Landsberger, A. H. Ali, Y. M. Khawassek, A. Eldidamony and A. M. Othman, *J. Radioanal. Nucl. Chem.*, 2024, **334**(2), 1225–1246.
- 245 F. Berg, C. Sirleaf, J. Lohmann, M. Breckheimer and T. Reich, *Appl. Geochem.*, 2025, **183**, 106332.
- 246 E. R. Mare, J. F. Chen, I. Buisman, C. Hayward, A. D. Burnham, C. Melai, E. E. Stüeken, G. Bromiley and S. Mikhail, *Geostand. Geoanal. Res.*, 2025, **49**(3), 590–596.
- 247 S. Li, K. Wen, Y. Yang, X. Lin, Y. Cao, Y. Xiao, H. Xian, J. Zhu and H. He, *J. Anal. At. Spectrom.*, 2025, **40**(8), 1954–1963.
- 248 A. Ishiguro, M. Arimoto, D. Sato, T. Tomoda, K. Itano, A. Tamura, H. Sugiyama, T. Kawae, M. Fukuyama, J. Kataoka, S. Terazawa, S. Shiota and T. Morishita, *Am. Mineral.*, 2024, **109**(9), 1591–1597.
- 249 M. A. Shamraeva, T. Visvikis, S. Zoidis, I. G. M. Anthony and S. Van Nuffel, *J. Am. Soc. Mass Spectrom.*, 2024, **35**(12), 2801–2814.
- 250 F. Altenberger, J. Krause, T. Auer, A. Auer and J. Berndt, *Geostand. Geoanal. Res.*, 2025, **49**(2), 281–294.
- 251 J. Mao, Y. S. Liu, W. Zhang, K. Q. Zong, A. Yang and X. T. Lü, *J. Anal. At. Spectrom.*, 2025, **40**(8), 1929–1939.
- 252 H. Zekri, D. Cohen, N. Rutherford, C. Folkes and M. Thomas, *J. Geochem. Explor.*, 2025, **269**, 107634.
- 253 S. Nava, R. Vecchi, P. Prati, V. Bernardoni, L. Cadeo, G. Calzolari, L. Carraresi, C. Cialdai, M. Chiari, F. Crova, A. Forello, C. Fratticcoli, F. Giardi, M. Manetti, D. Massabo, F. Mazzei, L. Repetto, G. Valli, V. Vernocchi and F. Lucarelli, *Atmos. Meas. Tech.*, 2025, **18**(9), 2137–2147.
- 254 G. Mainelis and T. T. Han, *J. Occup. Environ. Hyg.*, 2025, 1–18.
- 255 O. Zervaki, D. D. Dionysiou and P. Kulkarni, *Aerosol Sci. Technol.*, 2024, **58**(8), 889–901.
- 256 G. Zazzeri, L. Wacker, N. Haghipour, P. Gautschi, T. Laemmel, S. Szidat and H. Graven, *Atmos. Meas. Tech.*, 2025, **18**(2), 319–325.
- 257 T.-C. Le, Y.-Y. Tsai, C. C. Wang and C.-J. Tsai, *J. Aerosol Sci.*, 2025, **183**, 106479.
- 258 M.-S. Kwon, M. Yoo, J. Park and M.-H. Lee, *Sep. Purif. Technol.*, 2025, **359**, 130510.
- 259 D. Goderis, Y. Xiao, A. Alotbi, A. Ahtsham, J. T. Dvonch, A. J. Mason and A. P. Ault, *Aerosol Sci. Technol.*, 2025, **59**(2), 238–251.



- 260 E. Eckenberger, A. Mittereder, N. Gawlitta, J. Schnelle-Kreis, M. Sklorz, D. Brüggemann, R. Zimmermann and A. C. Nölscher, *Aerosol Res.*, 2025, **3**(1), 45–64.
- 261 M. Vaitilingom, C. Bernard, M. Ribeiro, C. Verhaege, C. Goubeyre, C. Berthod, A. Bianco and L. Deguillaume, *Atmos. Meas. Tech.*, 2025, **18**(5), 1073–1090.
- 262 B. J. Foley, S. M. Scott, M. G. Bronikowski, W. W. Kuhne, K. M. Samperton, A. R. Swindle, G. S. King, T. C. Shehee, J. H. Christian, B. E. Naes, T. J. Tenner and M. S. Wellons, *J. Anal. At. Spectrom.*, 2025, DOI: [10.1039/d5ja00114e](https://doi.org/10.1039/d5ja00114e).
- 263 A. Yamakawa, K. Nagano, K. Onishi, M. Ukachi and K. Inamasu, *Anal. Sci.*, 2025, **41**(8), 1373–1382.
- 264 R. Bergin, K. Samperton, M. Bronikowski, E. Hoar, J. Rolison, Q. Shollenberger, N. Marks, M. Wellons and S. Scott, *Talanta*, 2025, **285**, 127425.
- 265 B. Yang, J. Zheng, G. S. Yang, N. Qin, K. Tagami and S. Uchida, *J. Environ. Radioact.*, 2024, **278**, 107506.
- 266 C. Gómez-Pertusa, M. C. García-Poyo, G. Grindlay, R. Pedraza, M. A. Yañez and L. Gras, *J. Anal. At. Spectrom.*, 2024, **39**(7), 1736–1740.
- 267 A. I. Ivaneev, M. S. Ermolin, R. A. Zinovkin, A. A. Dashkevich, L. A. Zinovkina, B. V. Chernyak and P. S. Fedotov, *Anal. Methods*, 2025, **17**(3), 440–449.
- 268 X. Zhou, L. Y. Gui, Z. Y. Lu, B. B. Chen, Z. K. Wu, Z. Zhou, Y. Liang, M. He and B. Hu, *Anal. Chim. Acta*, 2024, **1324**, 343003.
- 269 K. Chen, Z. M. Wang, J. Wagner and K. Kumagai, *Atmosphere*, 2025, **16**(4), 361.
- 270 M. Pouyiousrou, T. Bochtler, C. Coith, H. Wikman, B. Kraft, T. Hielscher, A. Stenzinger, S. Riethdorf, K. Pantel and A. Kramer, *Clin. Chem.*, 2024, **70**(1), 297–306.
- 271 S. Das, K. Teinilä, H. Timonen, E. Ikonen and T. Laurila, *Environ. Monit. Assess.*, 2024, **196**(11), 1128.
- 272 G. Cioccia, R. Wenceslau, M. Ribeiro, G. S. Senesi, J. Cabral, G. Nicolodelli, C. Cena and B. Marangoni, *Microchem. J.*, 2024, **207**, 112142.
- 273 J. L. Li, J. Huang, L. N. Zheng, W. T. Feng, Y. H. Zhan and S. Naz, *Aerosol Sci. Technol.*, 2024, **58**(11), 1267–1280.
- 274 D. Diaz, A. Carreon and D. W. Hahn, *Photonics*, 2024, **11**(12), 1112.
- 275 M. Gao, R. Rong, Z. Q. Cai and Z. Wang, *J. Anal. At. Spectrom.*, 2024, **39**(9), 2230–2234.
- 276 Y. He and R. P. Mason, *Atmos. Environ.*, 2024, **337**, 120785.
- 277 P. Heikkilä, A. Rostedt, J. Toivonen and J. Keskinen, *Aerosol Sci. Technol.*, 2024, **58**(9), 1063–1078.
- 278 C. Piel, D. Romanini, M. Farradèche, J. Chaillot, C. Paul, N. Bienville, T. Lauwers, J. Sauze, K. Jaulin, F. Prié and A. Landais, *Atmos. Meas. Tech.*, 2024, **17**(22), 6647–6658.
- 279 M. Zabielska-Konopka, E. Zambrzycka-Szelewa, Z. Kowalewska and B. Godlewska-Zylkiewicz, *Talanta*, 2025, **281**, 126894.
- 280 L. Kronlachner, Z. Gajarska, P. Becker, D. Günther and A. Limbeck, *J. Anal. At. Spectrom.*, 2025, **40**(2), 467–477.
- 281 J. S. Stanberry, H. B. Andrews, C. V. Thompson, B. W. Ticknor and B. T. Manard, *Anal. Chem.*, 2025, **97**(3), 1688–1694.
- 282 T. L. Taylor, M. Strait and A. Gundlach-Graham, *Anal. Chem.*, 2024, **96**(52), 20535–20542.
- 283 M. Dia, P. E. Peyneau, D. Courtier-Murias and B. Bechet, *Environ. Sci.: Nano*, 2025, **12**(3), 1993–2007.
- 284 S. G. Morales, A. S. G. Garcia, V. V. Martínez, M. C. Rodriguez, V. M. D. Pidal and M. Montes-Bayón, *Talanta*, 2025, **287**, 127600.
- 285 B. Peng, Q. Y. Cai, X. Shi, Z. Y. Wang, J. Yan, M. Xu, M. Y. Wang, Z. Q. Shi, Z. S. Niu, X. P. Guo and Y. Yang, *J. Hazard. Mater.*, 2024, **476**, 134970.
- 286 E. C. Braysher, J. H. L. Cheong, D. M. Butterfield, A. S. Brown and R. J. C. Brown, *Atmosphere*, 2025, **16**(3), 283.
- 287 B. T. Manard, S. E. Szakas, J. S. Stanberry, B. W. Ticknor, L. O'Brien, M. Boris, J. T. Hewitt, P. Cable-Dunlap and H. B. Andrews, *J. Anal. At. Spectrom.*, 2025, **40**(5), 1241–1248.
- 288 S. M. Safavi, R. Abbasi, H. Ebrahimzadeh and A. A. Asgharinezhad, *Microchem. J.*, 2025, **213**, 113637.
- 289 M. Z. Wang, M. He, B. B. Chen and B. Hu, *Microchem. J.*, 2025, **212**, 113268.
- 290 E. Boyaci, A. Çagır, T. Shahwan and A. E. Eroglu, *Talanta*, 2025, **295**, 128373.
- 291 F. Aslan, H. Bingol and A. Tor, *Microchem. J.*, 2024, **206**, 111577.
- 292 A. Bozseki, M. Imamoglu, D. Avci and Y. Atalay, *J. Chromatogr.*, 2025, **1757**, 466118.
- 293 B. Yildiz, I. Durukan, M. Saylan, B. T. Zaman and S. Bakirdere, *Environ. Monit. Assess.*, 2024, **197**(1), 112.
- 294 M. R. Jamali, M. Katouk and R. Rahnama, *J. Food Compos. Anal.*, 2025, **145**, 107799.
- 295 M. Soylak, T. Zorlu and F. Uzcan, *J. Food Compos. Anal.*, 2025, **143**, 107545.
- 296 M. Soylak, A. M. A. Mohammed and H. E. H. Ahmed, *J. Food Compos. Anal.*, 2024, **130**, 106167.
- 297 T. Mumcu, S. Öncüoglu, C. G. Hizliates and S. S. Bozkurt, *J. Food Compos. Anal.*, 2025, **143**, 107638.
- 298 S. Korkmaz, E. H. Özkan, D. Uzun, N. K. Yetim and C. Özcan, *J. Sep. Sci.*, 2025, **48**(3), e70115.
- 299 Y. Z. Gao, H. P. Jiao, Z. H. Wang, J. B. Chao, J. Li, L. G. Hu, S. X. Zhang and J. Sun, *Spectrochim. Acta, Part B*, 2025, **224**, 107115.
- 300 M. Gao, J. H. Shi, Q. Li and Z. Wang, *Microchem. J.*, 2025, **213**, 113695.
- 301 M. Ahmad, A. Badshah, H. J. Li, M. Asad, M. A. Ibrahim, E. A. Ali, A. A. Shahat, U. Nishan, M. Khan and W. Sun, *J. Sep. Sci.*, 2024, **47**(20), e70004.
- 302 A. Amanzhol, O. Yalcinkaya, B. Cinar Acar and Z. Yuksekdog, *Microsc. Res. Tech.*, 2025, **88**(6), 1765–1783.
- 303 E. A. Bahaidarah, *Int. J. Anal. Chem.*, 2024, **2024**, 3152894.
- 304 D. Baskin, *ACS Omega*, 2025, **10**(9), 9537–9546.
- 305 M. Soylak, A. M. A. Mohammed and F. Uzcan, *J. Food Compos. Anal.*, 2025, **144**, 107733.
- 306 L. B. Hussien, E. M. Al-Kinani, H. Moradi, M. Gheibi and M. Eftekhari, *Microchem. J.*, 2025, **212**, 113374.
- 307 P. Poormoghadam and S. Bahar, *Int. J. Environ. Anal. Chem.*, 2024, **1–18**.
- 308 H. Q. Cai, H. M. Guo, H. L. Jing, P. P. Wen, Q. Y. Wu, Y. Li, Z. R. Suo and J. Zhang, *Separations*, 2025, **12**(3), 62.



- 309 W. T. Liu, L. Deng, H. Li, W. C. Lin, Y. Z. Yang, L. L. Zhang, R. R. Zhu, J. Zou, H. Y. Niu, Y. Y. Wang, C. Y. Tong and R. L. Zhu, *Talanta*, 2025, **284**, 127295.
- 310 R. Carvalho, T. A. Anunciação, A. F. Dantas, F. D. Dias and L. S. G. Teixeira, *J. Iran. Chem. Soc.*, 2024, **21**(10), 2635–2642.
- 311 K. Jankowski, M. Truskolaska, M. Borowska, J. Giersz and E. Reszke, *Molecules*, 2025, **30**(5), 1111.
- 312 D. Topaloglu, F. Uzcan, N. Kizil, B. B. Beydagi, D. E. Erbilgin, E. Basaran, M. L. Yola and M. Soylak, *J. Food Compos. Anal.*, 2025, **141**, 107348.
- 313 G. Roth, J. Silva, R. Faccio and M. Pistón, *RSC Adv.*, 2025, **15**(12), 9569–9575.
- 314 R. Mariychuk, S. Sukharev, O. Sukhareva, L. Roman and T. Babilia, *Environ. Geochem. Health*, 2024, **46**(11), 444.
- 315 W. A. Soomro, M. Y. Khuhawar, T. M. Jahangir, M. F. Lanjwani, Z. A. Bhatti, R. U. Z. Brohi and I. K. Rind, *Environ. Monit. Assess.*, 2025, **197**(3), 235.
- 316 M. Soylak, Q. Salamat and S. Sajjad, *Microchem. J.*, 2025, **211**, 113050.
- 317 Y. Q. Liu, Q. Han, Y. Y. Huo and X. H. Yang, *J. Water Chem. Technol.*, 2024, **46**(5), 480–490.
- 318 K. Karakebap, H. Serbest, F. Turak and S. Bakirdere, *J. Food Compos. Anal.*, 2025, **140**, 107281.
- 319 H. Alwael, K. A. Alzahrani, T. N. Abduljabbar, A. S. Alharthi, F. M. Alshareef, E. A. Bahaidarah, A. A. Alkhraije and M. S. El-Shahawi, *J. Fluoresc.*, 2025, 6539–6551.
- 320 I. Durukan and B. Yildiz, *Molecules*, 2024, **29**(17), 4189.
- 321 A. Saha, K. Sanyal, K. Kumari, S. B. Deb and M. K. Saxena, *J. Anal. At. Spectrom.*, 2025, **40**(2), 447–456.
- 322 A. Skok, N. Manousi, Y. Bazel, A. Vishnikin and A. Anthemidis, *Separations*, 2024, **11**(7), 193.
- 323 H. S. Alsalem, Y. G. Abou El-Reash, F. K. Algethami, M. A. Hashem, M. G. Wahba and M. A. Ismail, *Microchem. J.*, 2024, **206**, 111553.
- 324 T. Klis, P. Pohl, A. Dzimitrowicz and P. Jamroz, *J. Anal. At. Spectrom.*, 2024, **39**(12), 2982–2991.
- 325 K. Haslová and S. Musil, *Anal. Chem.*, 2025, **97**(6), 3545–3553.
- 326 M. R. Jamali, M. Tavakoli, A. Nezhadali and R. Rahnema, *Anal. Lett.*, 2025, 1–15.
- 327 M. S. Yalçın, S. Özdemir, E. Kilinç and M. Soylak, *J. Food Compos. Anal.*, 2024, **134**, 106561.
- 328 S. Ozdemir, N. Dizge, O. H. Abd-Elkader, G. Plavan and E. Kilinç, *J. Food Compos. Anal.*, 2025, **142**, 107382.
- 329 A. O. Klimov, A. Bakhadur, V. D. Abramova and K. A. Kokh, *Microchem. J.*, 2025, **210**, 112901.
- 330 P. L. He, X. L. Huang, L. Zhang, F. Yang, L. L. Chen and S. L. Sun, *J. Anal. At. Spectrom.*, 2025, **40**, 2062–2072.
- 331 W.-F. Zhang, D.-W. Zheng, F. Jourdan, A. Frew, C. Mayers, Y.-G. Xu, H.-Y. He, Y.-Q. Zhang, J.-J. Wang, Y.-D. Jiang, M. Xiao, J.-J. Li and J. Zhang, *J. Anal. At. Spectrom.*, 2024, **39**(9), 2173–2182.
- 332 E. Cannà, G. Sessa, S. Agostini and M. Tiepolo, *Geostand. Geoanal. Res.*, 2025, **49**(2), 343–356.
- 333 X. J. Nie, Y. Zhang, Z. Bao, K. Y. Chen, W. Q. Yang and H. L. Yuan, *J. Anal. At. Spectrom.*, 2025, **40**(8), 2049–2061.
- 334 X. Liao, T. Chen, T. Luo, Y. Cai, W. Zhang, Z. Yin and Z. Hu, *Geostand. Geoanal. Res.*, 2024, **49**(2), 385–401.
- 335 J. C. Xie, D. C. Zhu, Q. Wang, L. L. Zhang, W. T. Xu and T. R. Zhang, *At. Spectrosc.*, 2024, **45**(6), 490–497.
- 336 H. Lee, Y. Moussallam, E. F. R. Koga, L. Piani, J. Villeneuve, N. Bouden, A. A. Gurenko, B. Monteleone and G. A. Gaetani, *Chem. Geol.*, 2024, **670**, 122428.
- 337 L.-W. Xie, H.-R. Fan, H.-M. Yu, C. Huang, L. Xu, Y.-H. Yang, S.-T. Wu and H. Wang, *J. Anal. At. Spectrom.*, 2024, **39**(9), 2207–2219.
- 338 Y. Feng, W. Zhang, Y. Bao, X. Zeng, H. Liu, T. Luo, Z. Hu, M. Zhang, Y. Wang, Y. Yang and S. Liu, *Geostand. Geoanal. Res.*, 2024, **49**(1), 217–232.
- 339 Y. H. Cao, C. M. Xing, C. Y. Wang, X. Q. Ping and X. J. Lin, *J. Anal. At. Spectrom.*, 2025, **40**(1), 202–215.
- 340 X. L. Zeng, M. Li, W. Zhang, H. Y. Jin, Y. S. Liu, Z. C. Hu, T. Luo, S. J. Yang, Z. Y. Liu and J. Y. Wang, *J. Anal. At. Spectrom.*, 2025, **40**(3), 888–900.
- 341 Y. X. Zhang, N. Lv, Y. Zhang, X. J. Nie and H. L. Yuan, *At. Spectrosc.*, 2025, **46**(2), 150–160.
- 342 B. V. Ribeiro, C. L. Kirkland, M. Smit, K. Musiyachenko, F. J. Korhonen, N. J. Evans, K. Rankenburg, B. J. McDonald, S. Glorie, S. E. Gilbert, K. Goemann, I. Belousov, J. Oalman, C. Clark and S. Makin, *Geostand. Geoanal. Res.*, 2024, **48**(4), 887–908.
- 343 X. N. Yin, M. H. He, L. Zhang, W. F. Deng, Y. R. Guo, Z. X. Cui, Q. Yang, Y. Q. Zhang and G. J. Wei, *J. Anal. At. Spectrom.*, 2025, **40**(1), 104–109.
- 344 L. G. Wu, X. X. Ling, G. Q. Tang, Y. Liu, Z. Y. Chen, Q. L. Li, X. H. Li and B. Putlitz, *J. Anal. At. Spectrom.*, 2025, **40**(7), 1788–1795.
- 345 A. T. Hertwig, J. Chischi, A. K. Schmitt, H. C. Oskierski, K. Rankenburg, M. Wells, B. Putlitz and Z. Quadir, *Geostand. Geoanal. Res.*, 2025, **49**(4), 857–869.
- 346 Y. Q. Zhang, W. Wei, Z. Y. Zhang, X. Hu, H. M. Yu and F. Huang, *Geostand. Geoanal. Res.*, 2025, **49**(1), 259–270.
- 347 Z. Y. Chu, T. Q. Cui, T. C. Meisel, Y. L. Li, C. F. Li, L. Xu, Y. H. Yang and P. Peng, *Geostand. Geoanal. Res.*, 2025, **49**(2), 425–437.
- 348 C. Huang, H. Wang, L. W. Xie, L. Xu, S. T. Wu, Y. H. Yang and J. H. Yang, *Spectrochim. Acta, Part B*, 2025, **224**, 107117.
- 349 I. V. Nikolaeva, S. V. Palesskiy and A. S. Shaibalova, *Geochem. Int.*, 2024, **62**(11), 1219–1226.
- 350 J. L. Fu, X. Q. He, Z. C. Hu, S. Yin, J. Ma, K. Y. Chen and W. Zhang, *J. Earth Sci.*, 2025, **36**(1), 1–10.
- 351 L. L. Tian, X. L. Wang, Y. Guan, W. L. Xie, K. X. Xu, F. T. Tong, T. Yang and Y. B. Peng, *J. Anal. At. Spectrom.*, 2025, **40**(7), 1845–1851.
- 352 J. L. Hao, R. L. Chi, Z. J. Qiu, G. Q. Tang, Z. X. Cui, L. J. Feng, H. Yan, Q. Q. Zhu, P. Gao and W. Yang, *J. Anal. At. Spectrom.*, 2025, **40**(7), 1645–1651.
- 353 J. Wang, B.-X. Su, S.-Y. Wang, W.-J. Li, B.-Y. Gao and W.-G. Liu, *At. Spectrosc.*, 2024, **45**(3), 209–215.
- 354 H. J. Li, Z. Z. Hu, L. L. Zhang, D. C. Zhu, J. C. Xie, Q. Wang, W. T. Xu, L. J. Xu, W. Guo and J. Wu, *J. Anal. At. Spectrom.*, 2025, **40**(9), 2296–2305.



- 355 R. R. Chen, S. T. Wu, H. Wang, M. Senger, A. N. Paul, P. J. Sylvester, Y. H. Yang, J. H. Yang and F. Y. Wu, *Geostand. Geoanal. Res.*, 2025, **49**(1), 179–195.
- 356 Y. H. Yang, S. T. Wu, H. Wang, S. L. Kamo, Q. Ma, T. Liang, L. Xu, L. W. Xie, C. Huang, B. Wan, J. H. Yang and F. Y. Wu, *J. Anal. At. Spectrom.*, 2025, **40**(2), 326–337.
- 357 L. Qing, T. Luo, Z. Hu, Y. Li, J. Tu, L. Zhang, W. Zhang and K. Zong, *J. Anal. At. Spectrom.*, 2024, **39**(8), 2066–2077.
- 358 Y. Tang, N. Liu, J. Gao, J. Han, Z. Bai and T. Lan, *J. Anal. At. Spectrom.*, 2024, **39**(12), 3017–3024.
- 359 C. J. Beno, J. S. Lackey, M. D. Schmitz, J. R. Bowman, M. A. Stearns, J. M. Bartley and D. P. Fernandez, *Geostand. Geoanal. Res.*, 2024, **48**(4), 909–925.
- 360 S. Y. Zhang, Y. H. Yang, S. T. Wu, J. R. Tu, L. Xu, H. Wang, L. W. Xie, C. Huang, J. H. Yang and F. Y. Wu, *J. Anal. At. Spectrom.*, 2025, **40**(4), 931–941.
- 361 T. Luo, L. Y. Qing, C. X. Zhang, J. Crowley, Q. L. Li, X. X. Ling, X. P. Xia, D. F. He, X. D. Deng, W. Zhang and Z. C. Hu, *Geostand. Geoanal. Res.*, 2025, **49**(2), 403–423.
- 362 Z. Chen, L. G. Wu, X. X. Ling, J. F. Wotzlaw, C. Chelle-Michou, Y. Li, Z. H. Hou, W. L. Song, Q. Mao, W. Q. Yang, Y. Liu, G. Q. Tang, J. Li, Q. L. Li and X. H. Li, *J. Anal. At. Spectrom.*, 2024, **39**(10), 2580–2590.
- 363 S. R. Ma, G. L. Han, Q. Zhang, J. K. Liu, Z. Y. Ding and Y. Zhao, *Spectrochim. Acta, Part B*, 2025, **228**, 107185.
- 364 V. Chubarov, *Talanta*, 2025, **282**, 126981.
- 365 D. D. Li, Z. D. Zhang, X. S. Fan, T. H. Wu, Z. X. Huang, Q. Q. Shen, X. F. Liu and S. A. Liu, *J. Anal. At. Spectrom.*, 2025, **40**(5), 1383–1393.
- 366 A. N. Prow-Fleischer and Z. L. Lu, *Rapid Commun. Mass Spectrom.*, 2025, **39**(9), e10002.
- 367 C. Xu, W. Q. Li and S. C. An, *J. Anal. At. Spectrom.*, 2025, **40**(2), 411–420.
- 368 W. Li, B. Gao, Q. Pan, B. Yang, J. Wang and B. Su, *Geostand. Geoanal. Res.*, 2025, **49**(3), 665–674.
- 369 S. R. Scott, G. L. Turner, B. N. Gartman, S. A. Anguiano, K. M. Melby, B. E. Allen, T. D. Minton, M. A. Risenhuber and K. P. Hobbs, *J. Anal. At. Spectrom.*, 2025, **40**(4), 1098–1105.
- 370 Y. Zhang, W. Yang, Y. Wang, Y. He, S. Ke, K. Qu and S. Zhang, *Geostand. Geoanal. Res.*, 2025, **49**(2), 315–327.
- 371 Y. J. An, X. Li, W. N. Lu, J. B. Xu, Y. L. Xue, Q. Gong, Y. Peng, F. Liu, M. Ling and Z. Zhang, *Geostand. Geoanal. Res.*, 2024, **48**(4), 941–959.
- 372 B. Y. Peng, Q. H. Zhong, F. Y. Dong, G. B. Chu, L. Yin, J. Zhang and J. Li, *At. Spectrosc.*, 2025, **46**(2), 209–220.
- 373 W. Fujisaki, T. Maruoka, Y. Endo, Y. Sawaki and Y. Matsui, Early View Article, *Geostand. Geoanal. Res.*, 2025, **49**(4), 715–726.
- 374 D. Pathak and K. Mezger, *Geostand. Geoanal. Res.*, 2024, **48**(4), 863–885.
- 375 H. Liu, Z. C. Hu, L. Y. Qing, J. L. Guo, W. Zhang, X. H. Liao, T. Luo, M. Li and Z. C. Wang, *J. Anal. At. Spectrom.*, 2025, **40**(4), 1113–1121.
- 376 F. Y. Dong, Z. Y. Wang, L. Yin and J. Li, *Geostand. Geoanal. Res.*, 2025, **49**(2), 329–341.
- 377 T. He, H. Cao, W. Lang, Z. C. Hu, Z. C. Wang, Z. Q. Zou, W. Zhang, H. H. Chen and Y. S. Liu, *Geostand. Geoanal. Res.*, 2025, **49**(3), 555–567.
- 378 G. J. Macpherson, A. N. Krot, K. Nagashima and M. Ivanova, *Geochim. Cosmochim. Acta*, 2025, **391**, 291–311.
- 379 C. H. Ingles, J. A. Mavrogenes, N. D. Tailby and J. L. Wykes, *Chem. Geol.*, 2024, **670**, 122441.
- 380 D. Coenen, D. Evans, H. Jurikova, M. Dumont, J. Rae and W. Müller, *J. Anal. At. Spectrom.*, 2024, **39**(10), 2409–2420.
- 381 C. D. Standish, J. A. Milton, R. M. Brown and G. L. Foster, *J. Anal. At. Spectrom.*, 2025, **40**(5), 1309–1322.
- 382 J. D. Xu, A. Gerdes, A. Schmidt, D. C. Hezel and H. R. Marschall, *Geostand. Geoanal. Res.*, 2024, **48**(4), 807–822.
- 383 Y.-M. Huo, Z.-Y. Zhu, C.-F. Fan, Y.-W. She, J.-L. Hao and X.-K. Zhu, *J. Anal. At. Spectrom.*, 2025, **40**(3), 700–714.
- 384 J. Lu, W. Chen, F. Yang, Q. L. Li, K. D. Zhao and S. Y. Jiang, *Talanta*, 2025, **285**, 127371.
- 385 D. Asakawa and Y. B. Zhu, *Anal. Chem.*, 2024, **96**(41), 16315–16321.
- 386 J. Jiang, W. Chen, J. Lu, Y. H. Liu, M. Li, J. Sun, K. D. Zhao, S. Y. Jiang and Y. S. Liu, *J. Anal. At. Spectrom.*, 2025, **40**(4), 975–988.
- 387 L. Li, F. Liu, Q. Y. Peng, Z. F. Zhang, X. Li and Y. J. An, *J. Anal. At. Spectrom.*, 2025, **40**(7), 1767–1775.
- 388 J. Li, S. H. Tang, X. K. Zhu, J. X. Ma, Z. Y. Zhu and B. Yan, *J. Anal. At. Spectrom.*, 2024, **39**(12), 3106–3115.
- 389 H. Wu, J. H. Bai, X. R. Liang, X. B. Lu, Y. Y. Li, Y. N. Deng, Y. Zhao and G. J. Wei, *J. Anal. At. Spectrom.*, 2025, **40**(3), 860–867.
- 390 S. Rabin, F. X. d'Abzac, J. Chmieleff, F. Poitrasson and M. Grégoire, *Geostand. Geoanal. Res.*, 2024, **48**(3), 619–635.
- 391 G. H. Zhu, Z. M. Ge, L. Zhang, G. J. Wei and J. L. Ma, *J. Anal. At. Spectrom.*, 2024, **39**(11), 2783–2790.
- 392 D. Y. Li, L. Chen, H. O. Gu, G. C. Sun, J. H. Deng, S. Y. Yu, Y. Y. Zhao, Y. Zhang, N. Wang, X. Q. Guo, Z. S. Zhang, K. X. Feng, R. B. Zhang and S. Z. Li, *Rapid Commun. Mass Spectrom.*, 2025, **39**(13), e10041.
- 393 E. Wolfer, C. Burkhardt and T. Kleine, *J. Anal. At. Spectrom.*, 2025, **40**(4), 1023–1036.
- 394 Y. Otsuki, K. I. Bajo, T. Obase and H. Yurimoto, *J. Anal. At. Spectrom.*, 2025, **40**(6), 1505–1517.
- 395 T. Zhou, L. Qi, S. H. Liu and B. Zhou, *J. Anal. At. Spectrom.*, 2024, **39**(11), 2694–2702.
- 396 E. Albalat, P. Télouk and V. Balter, *J. Anal. At. Spectrom.*, 2024, **39**(9), 2183–2191.
- 397 S. T. Wu, Y. H. Yang, H. Wang, N. M. W. Roberts, J. L. Niu, Y. J. Wang, J. H. Yang and F. Y. Wu, *Chem. Geol.*, 2024, **670**, 122383.
- 398 M. Martini, P. Francus, L. Schröer, F. Buyse, P. Kibleur, V. Cnudde, L. D. Trotta and P. Després, *Geostand. Geoanal. Res.*, 2025, **49**(3), 645–664.
- 399 M. Limonta, C. France-Lanord, A. Galy, A. Gurenko, N. Bouden and E. Garzanti, *Chem. Geol.*, 2025, **673**, 122525.
- 400 H. Y. Bao, J. Li, W. S. Ni, T. T. Wang, N. P. Shen, G. B. Chu, J. G. Liu, J. J. Liu and J. F. Xu, *Anal. Chem.*, 2025, **97**(14), 8048–8055.



- 401 J. H. Liu, L. Zhou, X. Wang, J. W. Li, T. J. Algeo and X. D. Deng, *J. Anal. At. Spectrom.*, 2025, **40**(3), 868–878.
- 402 Y. M. Liu, T. Y. Chen, T. Li, W. Q. Li, Q. Q. Hong and J. B. Chen, *J. Anal. At. Spectrom.*, 2024, **39**(11), 2748–2755.
- 403 X. N. Liu, M. Klaver, R. C. Hin, C. D. Coath, H. C. Ng and T. Elliott, *J. Anal. At. Spectrom.*, 2024, **39**(11), 2799–2808.
- 404 W. R. Song, C. W. Zhu, H. J. Wen, Y. X. Zhang, Z. R. Liu and M. F. Zhou, *Geostand. Geoanal. Res.*, 2025, **49**(1), 245–258.
- 405 Q. Qu, W. Liu, W. Zheng, B. Chetelat, Q. Liu and J. Chen, *J. Anal. At. Spectrom.*, 2024, **39**(9), 2258–2269.
- 406 A. Buzenchi, H. Moreira, E. Bruand, O. Bruguier and B. Dhuime, *Chem. Geol.*, 2024, **666**, 122306.
- 407 J. L. Niu, S. T. Wu, Y. H. Yang, H. Wang, C. Huang, L. Xu and L. W. Xie, *J. Anal. At. Spectrom.*, 2024, **39**(12), 3060–3068.
- 408 S. Yang, L. L. Zhang, R. Wang, D. C. Zhu, J. C. Xie, Q. Wang and W. T. Xu, *J. Anal. At. Spectrom.*, 2024, **39**(10), 2421–2432.
- 409 J. An, L. Wu, F. Wang, Q. D. Wei, J. B. Sun, Z. Y. Zhang, R. Ren and N. Wang, *J. Anal. At. Spectrom.*, 2024, **39**(12), 3127–3141.
- 410 X. J. Nie, Z. Bao, C. L. Zong, D. Y. Peng, N. Lv and H. L. Yuan, *At. Spectrosc.*, 2024, **45**(4), 298–308.
- 411 Q. H. Zhong, L. Yin, G. B. Chu, C. F. He and J. Li, *J. Anal. At. Spectrom.*, 2025, **40**(5), 1353–1363.
- 412 L. P. Feng, C. Wang, Y. Han, W. Zhang, J. L. Guo, L. Zhou and Z. C. Hu, *J. Anal. At. Spectrom.*, 2024, **39**(12), 3035–3047.
- 413 Q. S. Huang, Y. L. Sun and S. Q. Zhao, *J. Anal. At. Spectrom.*, 2025, **40**(3), 795–807.
- 414 Y. L. Zeng, G. Q. Wang and T. C. Meisel, *Geostand. Geoanal. Res.*, 2025, **49**(4), 737–750.
- 415 W. S. Ni, T. T. Wang, X. J. Mao, L. P. Zhang, X. R. Guo, L. Fan, H. L. Zhang and F. Xiao, *Talanta*, 2025, **281**, 126932.
- 416 P. Frossard, J. M. J. Ball and M. Schönbächler, *J. Anal. At. Spectrom.*, 2025, **40**(1), 146–161.
- 417 X. L. Dong, J. H. Liu, Z. X. Jia, S. Z. Tang, S. Y. Tong, Y. X. Xiong and L. Ouyang, *Anal. Chim. Acta*, 2025, **1363**, 344195.
- 418 F. Cao, R. Y. Sun, L. Schneider, Y. Q. Zhang, S. J. Li, R. J. Yan, S. C. Tao, X. Y. Jiang, P. F. Li, W. Zheng, J. B. Chen and Y. Liu, *J. Anal. At. Spectrom.*, 2025, **40**(5), 1373–1382.
- 419 A. Piraquive, J. P. Machado, P. Machado, M. H. Huyskens, T. F. Redfield, R. van der Lelij and J. Knies, *Chem. Geol.*, 2025, **677**, 122626.
- 420 A. A. Verbel, M. E. Schutesky, D. D. Gregory and A. Verbel, *J. Geochem. Explor.*, 2025, **271**, 107701.
- 421 J. E. Abramson, Y. Chen and G. T. Seidler, *J. Anal. At. Spectrom.*, 2025, **40**(3), 817–824.
- 422 H. B. Andrews, L. Hendriks, S. B. Irvine, D. R. Dunlap and B. T. Manard, *J. Anal. At. Spectrom.*, 2025, **40**(3), 910–920.
- 423 R. C. Marsden, L. Martin, M. Aleshin and P. Guagliardo, *Comput. Geosci.*, 2024, **192**, 105683.
- 424 B. Galindo-Prieto, I. S. Mudway, J. Linderholm and P. Geladi, *J. Chemom.*, 2025, **39**(3), e70010.
- 425 D. Capela, T. Lopes, F. Dias, M. F. S. Ferreira, J. Teixeira, A. Lima, P. A. S. Jorge, N. A. Silva and D. Guimaraes, *Spectrochim. Acta, Part B*, 2025, **223**, 107085.
- 426 S. U. Choi, S. C. Han and J. I. Yun, *Anal. Chim. Acta*, 2025, **1364**, 344191.
- 427 Z. Gajarska, A. Faruzelová, E. Képes, D. Prochazka, P. Porízká, J. Kaiser, H. Lohninger and A. Limbeck, *J. Anal. At. Spectrom.*, 2024, **39**(12), 3151–3161.
- 428 J. Ren, S. M. Jiang, C. Sun, Z. G. Li, Y. H. Dong, L. Chen, X. B. Han, J. Yu and W. D. Wu, *J. Anal. At. Spectrom.*, 2025, **40**(3), 825–835.

